



HAL
open science

Spontaneous decoherence in large Rydberg systems

Eric Magnan

► **To cite this version:**

Eric Magnan. Spontaneous decoherence in large Rydberg systems. Optics [physics.optics]. Université Paris Saclay (COMUE), 2018. English. NNT : 2018SACLO008 . tel-02084130

HAL Id: tel-02084130

<https://pastel.hal.science/tel-02084130>

Submitted on 29 Mar 2019

HAL is a multi-disciplinary open access archive for the deposit and dissemination of scientific research documents, whether they are published or not. The documents may come from teaching and research institutions in France or abroad, or from public or private research centers.

L'archive ouverte pluridisciplinaire **HAL**, est destinée au dépôt et à la diffusion de documents scientifiques de niveau recherche, publiés ou non, émanant des établissements d'enseignement et de recherche français ou étrangers, des laboratoires publics ou privés.

Spontaneous decoherence in large Rydberg ensembles

Thèse de doctorat de l'Université Paris-Saclay
préparée à Institut d'Optique Théorique et Appliquée

Ecole doctorale n°572 École Doctorale Onde et Matière (EDOM)
Spécialité de doctorat : Physique

Thèse présentée et soutenue à Palaiseau (France), le 17 décembre 2018, par

ÉRIC MAGNAN

Composition du Jury :

Daniel COMPARAT Directeur de Recherches, Laboratoire Aimé Cotton	Président
Shannon WHITLOCK Professeur, IPCMS & ISIS	Rapporteur
Olivier GORCEIX Professeur, Laboratoire de Physique des Lasers	Rapporteur
Isabelle BOUCHOULE Chargée de Recherches, Laboratoire Charles Fabry	Examinatrice
Trey PORTO Fellow, Joint Quantum Institute	Co-directeur
Antoine BROWAEYS Directeur de Recherches, Laboratoire Charles Fabry	Directeur

RÉSUMÉ

De nombreux phénomènes de la vie quotidienne sont bien plus subtils qu'ils n'y paraissent. C'est le cas par exemple du magnétisme, qui, bien que très simple en apparence, se révèle très complexe à l'échelle atomique. En pratique, même les modèles les plus simples demandent rapidement une puissance de calcul bien supérieure à celle des supercalculateurs actuels.

Pour contourner cet obstacle, une alternative consiste à remplacer le calcul par la mesure d'un système expérimental se comportant comme le modèle : c'est la simulation quantique. Cette technique a été proposée pour étudier un vaste panel de problèmes, allant du rayonnement de Hawking à la thermodynamique quantique, avec différentes plateformes expérimentales telles que les ions, photons ou gaz d'atomes froids.

La simulation quantique permet notamment d'étudier des phases exotiques de la matière, comme par exemple les rotons, solitons, supersolides ou encore les phases topologiques. Ces phases n'apparaissent pas spontanément dans les gaz d'atomes alcalins, mais plusieurs travaux théoriques ont montré qu'elles peuvent émerger en présence d'interactions à longue portée.

Pour augmenter la portée des interactions dans un échantillon atomique, une solution consiste à exciter les atomes dans des états électroniques n de haute énergie appelés états de Rydberg. Ces états ont une interaction de type van der Waals, laquelle évolue rapidement avec le niveau d'énergie ($U_{\text{vdW}} \propto n^{11}$). Cependant, ces états ont une durée de vie trop courte pour permettre d'observer les nouvelles phases (voir Fig.1 a).

Ce problème peut être résolu en mélangeant de manière cohérente une petite fraction $\varepsilon \ll 1$ d'états de Rydberg $|r\rangle$ avec une fraction plus large d'atomes dans l'état fondamental $|g\rangle$. Le mélange qui en résulte $|\psi\rangle = (1 - \varepsilon) |g\rangle + \varepsilon |r\rangle$ combine long temps de vie et large portée d'interactions (voir Fig.1 b). Cette proposition d'habillage Rydberg offre ainsi une solution expérimentale pour observer de nouvelles phases de la matière dans des échantillons d'atomes alcalins.

Cette idée a suscité un vaste intérêt dans la communauté scientifique et a conduit à de nombreuses études théoriques. L'habillage Rydberg a été appliqué avec succès sur un système de deux atomes (voir Fig.1 c), mais la même technique appliquée à des systèmes plus larges n'a pas produit les résultats escomptés.

b

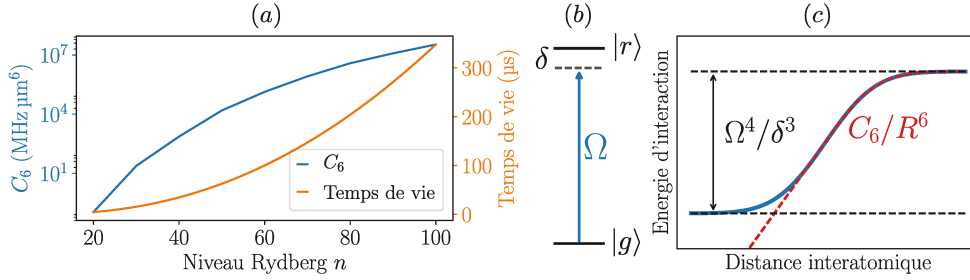


FIGURE 1 – (a) Les interactions de type van der Waals ($\Delta E = C_6/R^6$, en bleu) augmentent dramatiquement avec le niveau d’excitation n . Notez l’échelle logarithmique pour cette courbe. Le temps de vie (en orange) augmente également avec le niveau d’excitation (échelle linéaire), mais il reste très inférieur au temps nécessaire pour observer les nouvelles phases de la matière (1 – 100 ms). (b) Pour l’habillage Rydberg, la transition est excitée avec une fréquence de Rabi Ω et un désaccord δ . Ces deux paramètres permettent de contrôler la fraction d’états de Rydberg $\varepsilon = \Omega/2\delta$. (c) Une des conséquences de l’habillage Rydberg est l’apparition d’une saturation à courte distance dans le potentiel de van der Waals. C’est ce qui a été mesuré dans l’expérience à deux atomes de G.W. Biedermann.

En 2015, des expériences menées au JQI ont permis de comprendre les raisons de cet échec. Le groupe a identifié un comportement anormal de la transition Rydberg, et notamment un élargissement de la largeur de raie de plusieurs ordres de grandeur. Cet effet est attribué à l’apparition spontanée de plusieurs états de Rydberg différents dans le système (voir Fig.2 a). Les interactions de type dipole-dipole résonant entre ces états conduisent à un déphasage en chaîne et à un dérèglement du paramètre ε (voir Fig.2 b). La physique du problème étant très corrélée, seules des analyses en loi d’échelle ont pu être proposées (voir Fig.2 c). D’autres modèles plus complexes ont plus tard été développés sur la base des observations de l’équipe.

Lors de mon arrivée au Joint Quantum Institute (JQI) en janvier 2016, ces mesures avaient déjà été réalisées et laissaient peu d’espoir quant à l’utilisation de l’habillage Rydberg pour l’observation de nouvelles phases de la matière. Cependant, nous avons proposé trois axes de progression : valider le mécanisme par d’autres méthodes, étudier la dynamique des populations Rydberg et explorer de possibles solutions pour éviter la décohérence.

Pour prédire la dynamique des populations, nous proposons un système d’équations de taux non-linéaires fondé sur un argument de champ moyen. Notre hypothèse suppose que l’élargissement de la raie Rydberg est uniquement dû à la densité de nouveaux états Rydberg (états “polluants”) dans le système. Ce schéma permet d’extraire l’évolution temporelle des populations Rydberg ainsi que celle du taux de pompage et de la largeur de raie.

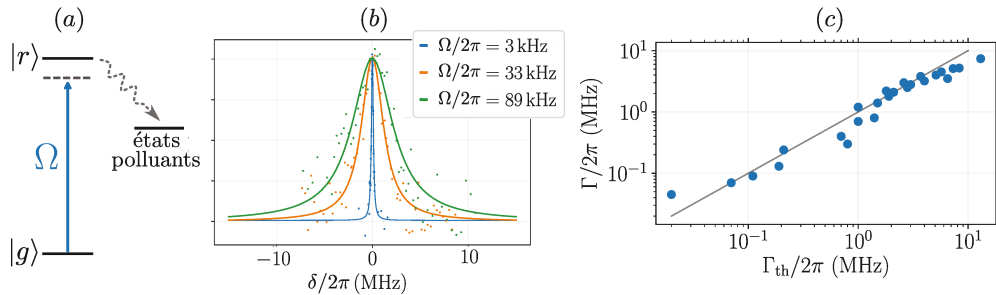


FIGURE 2 – (a) Le rayonnement du corps noir stimule des transferts radiatifs depuis l'état de Rydberg initial vers d'autres états de Rydberg voisins : les états polluants. Ce transfert est la première étape d'une avalanche de déphasage. (b) En augmentant Ω , on observe des largeurs de raie plus de 200 fois supérieures à la largeur naturelle. (c) Partant de l'hypothèse d'un déphasage induit par interaction dipole-dipole résonnant entre les différentes populations d'atomes de Rydberg, l'équipe a estimé une largeur de raie théorique par loi d'échelle. Ce graphe compare les largeurs mesurées à la loi d'échelle : les données (bleu) s'alignent raisonnablement sur la droite unitaire (gris), validant ainsi l'hypothèse d'interaction dipolaire (échelle logarithmique).

Certains états peuvent être mesurés directement par fluorescence (voir Fig.3 a) : nous observons un accord raisonnable entre les mesures et le modèle de champ moyen (voir Fig.3 b). Le dispositif expérimental du JQI ne permet pas de mesurer directement la dynamique des états polluants. Pour identifier leur impact sur le système, nous aggravons volontairement leur effet en augmentant leur population. Nous utilisons une seconde transition Rydberg pour introduire artificiellement de nombreux états polluants dans le système. La transition habituelle $|g\rangle \rightarrow |r\rangle$ permet de sonder leur évolution temporelle (voir Fig.3 c) et de quantifier leur impact sur la largeur de raie et le taux de pompage (voir Fig.3 d).

Par ailleurs, nous examinons plusieurs méthodes en vue d'éliminer l'élargissement de la transition Rydberg. Une première approche consiste à travailler à temps courts ($t \lesssim 10$ ps) afin d'éviter l'accumulation d'états polluants dans le système (voir Fig.4 a). Cette technique, notamment utilisée dans l'expérience de Munich, permet théoriquement d'augmenter le temps de cohérence en contrepartie d'une diminution de l'effet d'habillage Rydberg. Dans une expérience d'excitation stroboscopique, nous montrons que cette méthode est limitée par l'élargissement Fourier à temps courts. La plus petite largeur de raie mesurée se situe autour de 1 MHz, correspondant à plus de 20 fois sa largeur naturelle.

Une autre approche consiste à réduire la température du système. En effet, l'apparition des états polluants se fait au moyen de transferts radiatifs depuis l'état de Rydberg initial. Réduire la température de l'enceinte permet de diminuer la probabilité d'une désexcitation stimulée par le rayonnement du corps noir. Nos simulations montrent que des conditions cryogéniques permettent effectivement de limiter la décohérence. Cependant,

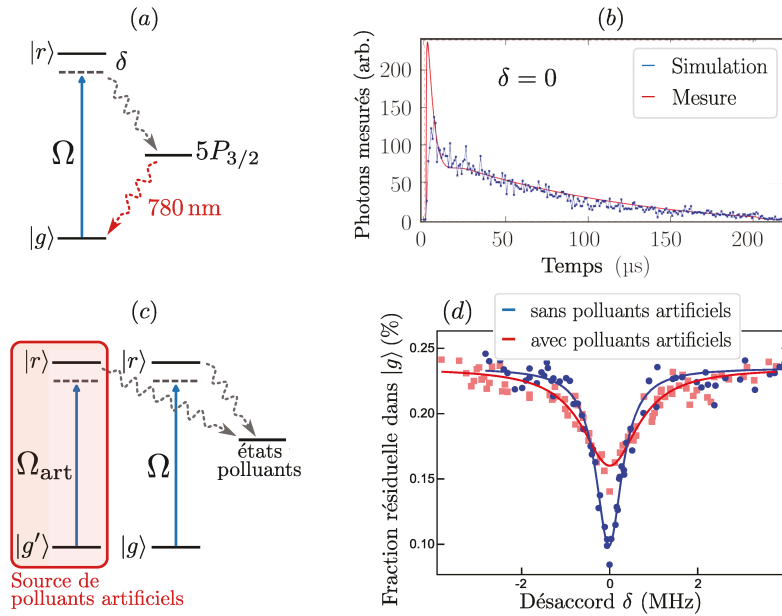


FIGURE 3 – (a) Lors de la désexcitation des états $|r\rangle$, nous collectons les photons à 780 nm émis par fluorescence depuis l'état intermédiaire $5P_{3/2}$. (b) Les mesures de fluorescence résolues en temps permettent de quantifier la dynamique de la population d'états $|r\rangle$. Dans cet exemple à résonance ($\delta = 0$), les équations de taux (en rouge) sont en bon accord avec les données expérimentales (en bleu). (c) Nous utilisons une seconde transition Rydberg pour générer des états polluants supplémentaires. Cette technique permet d'étudier l'influence des états polluants sur la largeur de transition. (d) Comparaison de spectres avec (rouge) et sans (bleu) états polluants artificiels. La présence de polluants supplémentaires conduit à un net élargissement de la raie.

cette technique n'a pas été envisagée au JQI en raison des modifications majeures du dispositif qu'elle aurait nécessité.

A la même période, une équipe de l'Institut d'Optique travaillant sur des recherches similaires a également constaté la nécessité d'un environnement cryogénique pour améliorer les performances de leur plateforme expérimentale. J'ai rejoint l'équipe début 2018 et réalisé quelques études préliminaires en vue du développement d'une expérience de simulation quantique avec des atomes de Rydberg dans une enceinte cryogénique.

Plus généralement, nos simulations montrent que l'avalanche de décohérence est fonction du nombre d'atomes dans le système N , du niveau Rydberg n et de la température de l'enceinte. Les conditions idéales réunissent température cryogénique, bas niveau Rydberg et faible nombre d'atomes. L'expérience de Munich parvient à limiter la décohérence en utilisant un très faible nombre d'atomes ($N \approx 150$) et un niveau Rydberg relativement bas ($n = 43$).

Dans l'immédiat, l'utilisation de l'habillage Rydberg pour la simulation de phases exotiques est peu engageante. A long terme, certains progrès

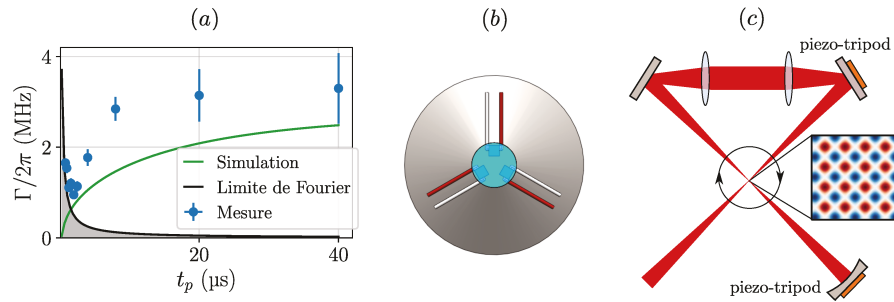


FIGURE 4 – (a) L’expérience stroboscopique montre que les largeurs de raie mesurées (en bleu) atteignent un minimum 20 fois supérieur à la largeur de raie naturelle. Cet élargissement est dû à l’élargissement Fourier (en gris). Cette méthode ne permet donc pas de compenser pleinement l’avalanche de décohérence. (b) Nous avons conçu un miroir vibrant pour des expériences de Floquet. Combiner trois piézo-actuateurs indépendants permet une haute stabilité de pointé sur de large amplitudes de déplacement. (c) Le super-réseau optique du JQI combiné avec deux miroirs vibrants permet désormais de déplacer le réseau dans un espace bidimensionnel. Cet outil est une étape majeure vers l’étude de structures de bande topologiques.

techniques pourraient permettre de reconsidérer cette idée. Par exemple, la disponibilité de sources intenses dans l’ultraviolet pourrait amoindrir l’influence du déphasage sur l’habillage Rydberg. D’autre part, les remarquables progrès dans le refroidissement de molécules polaires ouvrent également la voie vers l’observation de phases exotiques dans des échantillons comportant naturellement des interactions de longue portée.

A la suite de nos observations, les recherches du groupe ont pris une direction différente. L’équipe s’intéresse désormais des problématiques d’ingénierie quantique, et en particulier à la création de structures de bandes topologiques. Conformément au formalisme de Floquet, la méthode utilise des réseaux optiques secoués périodiquement. Les méthodes habituelles ne pouvant être adaptées à l’architecture en nœud papillon du réseau, nous avons développé un système de miroir vibrant piloté par trois piézo-actuateurs indépendants (voir Fig.4 b, c). L’expérience, désormais équipée de deux exemplaires de ces miroirs, permet notamment de mouvoir le réseau en cercle et d’ainsi explorer des effets de chiralité. Les derniers mois de l’année 2017 ont été dédiés à l’étude des instabilités paramétriques présentes dans ces systèmes.

ACKNOWLEDGMENTS

I acknowledge the support of the National Science Foundation via the Physics Frontier Center at Joint Quantum Institute. This PhD was also supported by the Fulbright Program via the Commission Franco-Américaine and the Institut d'Optique.

I warmly thank my jury : Isabelle Bouchoule, Olivier Gorceix, Shannon Whitlock and Daniel Comparat.

I am obliged to my two advisors, Trey Porto and Antoine Browaeys, for giving me the opportunity to work in their teams. I also thank Luis Orozco who made this PhD possible, and Thierry Lahaye who kindly mentored me during this past year.

I wish to express my gratitude to the other teams, namely Rb1, RbRy, Chadoq and Cyclopix. It's been a pleasure working with you, guys.

I warmly thank Timothée Cognard, H el ene Arvis, Lara Ehrenhofer and Nudrat Piracha, who have been my partners in crime in many adventures. Thanks for your encouragements!

And finally, a very special gratitude to my family: I owe it all to you.

A NOTE TO THE JURY

In 2015, I had the opportunity to do a joint Ph.D. between Trey Porto’s and Antoine Browaeys’ laboratories. Both experiments focus on quantum simulation using atoms in the Rydberg state: while the American experiment studies dissipation in large ensembles, the French experiment investigates the dynamics of smaller ensembles.

I started my Ph.D. in January 2016 at the Joint Quantum Institute (JQI) and stayed there for two years. We identified an avalanche decoherence mechanism affecting large Rydberg ensembles: this work had a large resonance in the cold atom community as it calls into question dozens of proposals. In January 2018, I joined the team at Laboratoire Charles Fabry at Institut d’Optique (LCFIO) to work on an evolution of their “atom-by-atom assembler”. This new setup aims to eliminate the black-body radiation at the origin of the broadening mechanism. Our goal is to make sure that large structures assembled on the tweezer-based experiment will not be affected by the decoherence.

As cold atoms experiments always correspond to a collective effort, it may be difficult to identify my contributions. Below is a list of some of my achievements as a graduate student.

- In early 2015, the experiment had just been move from the N.I.S.T building and was still to be reassembled. After Bose-Einstein condensation was achieved, I was in charge of the Rydberg excitation. In particular, we took the opportunity to modernize the setup.
- Later that year, I dedicated some significant amount of time to the double-wells optical lattice. We did not get to use this tool to its full capacity that year, but we achieved to get balanced sublattices.
- While the first publication concerning the decoherence in Rydberg ensembles was published before my arrival[60], I built the optics and took the data for the two next publications[24, 149].
- I built and characterized the “piezo-mirrors” currently used on the JQI experiment for Floquet excitation (see App.A).
- At LCFIO, I assembled from scratch a new experimental setup for cold atom experiments under the supervision of T. Lahaye. I also performed series of tests in an optomechanical mount at 77 K.

Palaiseau, France, October 2018

Éric Magnan

PUBLICATIONS

PUBLICATIONS BY THE AUTHOR

T. Boulier *et al.*, “Parametric instabilities in a 2D periodically-driven bosonic system: Beyond the weakly-interacting regime”, *submitted to PRX* (2018) ([arXiv:1808.07637](https://arxiv.org/abs/1808.07637))

E. Magnan *et al.*, “A low-steering piezo-driven mirror.”, *RSI* **89**, 073 110 (2018). (doi: [10.1063/1.5035326](https://doi.org/10.1063/1.5035326))

J.T. Young *et al.*, “Dissipation induced dipole blockade and anti-blockade in driven Rydberg systems”, *PRA* **97**, 023 424 (2018). (doi: [10.1103/PhysRevA.97.023424](https://doi.org/10.1103/PhysRevA.97.023424))

T. Boulier *et al.* “Spontaneous avalanche dephasing in large Rydberg ensembles”, *PRA* **96** 053 409 (2017). (doi: [10.1103/PhysRevA.96.053409](https://doi.org/10.1103/PhysRevA.96.053409))

OTHER RELEVANT PUBLICATIONS FOR THIS WORK

E. A. Goldschmidt *et al.*, “Anomalous Broadening in Driven Dissipative Rydberg Systems.”, *PRL* **116**, 113 001 (2016) (doi: [10.1103/PhysRevLett.116.113001](https://doi.org/10.1103/PhysRevLett.116.113001))

J. E. Johnson and S. L. Rolston “Interactions between Rydberg-dressed atoms.”, *PRA* **82**, 033 412 (2010) (doi: [10.1103/PhysRevA.82.033412](https://doi.org/10.1103/PhysRevA.82.033412))

INTRODUCTION

Many phenomena observed in condensed matter physics are still not properly understood today. Physicists are able to write simplified theoretical models that capture the essence of the phenomena, but these models are still too complicated to be solved when the number of interacting particles is larger than a few tens[103]. This is especially true when the interactions are long-range or when dissipation is present because the system is not well-enough shielded from the fluctuations of its environment.

The field of quantum simulation has emerged as one approach to solve these problems[55, 88]. It consists in building artificial experimental systems that are ruled by the idealized models proposed by the theorists. Measuring the properties of these engineered systems gives access to properties of the model that is otherwise impossible to calculate.

Over the last 20 years, several experimental platforms for quantum simulation have been proposed, including superconducting circuits[121], interacting photons[70], trapped ions[152] and cold atoms[19, 76]. Among them, laser-cooled atoms prepared in highly-excited “Rydberg” states are promising candidates[127, 145]. The van der Waals interaction between two atoms scales as $\propto n^{11}$ (where n is the principal quantum number), allowing strong interactions even at interatomic distances of a few micrometers[53]. Moreover, the interaction is fully controllable with lasers or static electric fields. Remarkably, the interaction can also be mapped onto spin Hamiltonians, which are relevant to many models proposed in condensed matter physics[83, 147].

Among Rydberg-based quantum simulators, two different approaches have emerged. On one hand, atoms trapped in optical lattices allow to engineer large arrays of atoms with a fixed geometry where several thousands of particles are separated by intersite distances of $0.5\ \mu\text{m}$ [84, 99]. On the other hand, arrays of individual microtraps allow to produce mesoscopic structures of arbitrary geometry containing several tens of atoms at tunable interatomic distances $\geq 3\ \mu\text{m}$ [10, 117]. These two solutions allow to address the atoms individually, *i.e.* detect and manipulate each atom independently of its neighbor.

Interatomic distances plays a major role in both types of simulators. In the case of atoms in individual microtraps, the large distances between the atoms requires to work at high Rydberg states ($n > 50$) in order to get strong enough interactions. As the radiative lifetime scales with the Rydberg level ($\propto n^3$), it can reach several hundreds of microseconds. This timescale is much larger than the usual times of the experiment

($\sim 100 \text{ ns} - 1 \mu\text{s}$) and allows to observe the coherent evolution of the ensemble of interacting atoms. This is an ideal system to explore interaction induced dynamics in an elementary closed many-body system.

On the opposite, atoms in optical lattices are much closer to each other and do not necessitate high levels of Rydberg states. Principal quantum numbers around $n = 20$ are typically sufficient to produce visible interactions. The typical lifetimes of such states is relatively short ($5 \mu\text{s}$) and can lead to dissipation and relaxation of the system. Relaxation to equilibrium is predicted to hide interesting phenomena, notably the spontaneous formation of an antiferromagnetic order[98]. The model predicts an oscillation between two anti-ferromagnetic configurations — seeing this effect in the laboratory would be an experimental realization of an elementary open many-body system.

Both types of simulators are limited by the radiative lifetime of Rydberg states, leading to a regime where the atoms are effectively frozen in space during the experiment. However, major effects related to the mechanical motion of the atoms have been predicted to exist, notably non-linear dynamics[110] and exotic phases such as supersolidity[107]. The timescale of these effects is directly linked to the trapping frequencies of the optical lattice (typically in the kHz range), and thus requires atomic lifetimes in the range $1 - 10 \text{ ms}$.

In recent years, “Rydberg-dressing” has been proposed as a solution to increase the lifetime of Rydberg ensembles by several orders of magnitude while maintaining relatively strong interactions[23, 58, 87]. The proposal consists in coherently admixing a large fraction of ground state atoms with a small fraction of Rydberg states, resulting in a mixture combining long lifetime and long interaction ranges. While this approach has been successful with two atoms[86], deviations to the theory have been seen in all experiments using larger ensembles[1, 46, 54, 60].

In this thesis, we investigate the two types of Rydberg-based quantum simulators. In a first serie of experiments performed at Joint Quantum Institute (University of Maryland, USA), we study the physics of a Bose-Einstein Condensate loaded into optical lattices and excited to the $18S$ level. We show that the spontaneous apparition of a population in nearby Rydberg states triggers an avalanche of decoherence responsible for the anomalies observed in Rydberg dressing experiments in large ensembles. The decoherence emerges from stimulated emission induced by blackbody radiation followed by diffusion via resonant dipole-dipole interaction between states of opposite parity. This type of physics being extremely complex, we use simple scalings based on mean-field approximations to analyze the effects.

We then investigate the time evolution of the several Rydberg populations in the system. While some populations can be directly measured by fluorescence, others require indirect schemes: we use a “pump-probe” technique to decouple the production of pollutant states from their observation. Our measurements show a good agreement with mean-field models. Though Rydberg dressing does not seem applicable for large scale quantum simulators, we show that the decoherence can be mitigated to some extent by several simple techniques such as stroboscopic excitation or using cut-off cavities. The use of a cryostat to inhibit blackbody radiation emerges as a particularly efficient solution, at the cost of being technically demanding.

Experiments performed in an array of microtraps at the Laboratoire Charles Fabry at Institut d’Optique (Palaiseau, France) show that the size of the atomic structures is limited by two-body collisions with the background residual gas. Using a cryostat could reduce the pressure by several order of magnitude in a process called cryopumping, where gaseous particles freeze at the contact of cold walls and stick to them. However, this types of experiment uses optomechanical components under vacuum: their adaptation to a cryogenic environment is bound to be challenging. We present the first investigations concerning the optomechanical design at 4 K.

This thesis is divided as follows:

- A. The first part (see Part.i) is an introduction to the techniques of atom cooling and trapping and Rydberg excitation. While Ch.1 provides some details about the production of ultracold gases in optical lattices, Ch.2 is dedicated to the physics of Rydberg states.
- B. The second part (see Part.ii) covers experimental investigations of the spontaneous onset of decoherence in large Rydberg ensembles done at JQI at University of Maryland. In Ch.3, we detail steady-state observations, Ch.4 explores the time evolution of the Rydberg populations.
- C. The third part (see Part.iii) concerns the design of a new apparatus using a 4 K cryostat with high-precision optomechanical components inside. This work was done at LCFIO. Our first tests are gathered in Ch.5.

CONTENTS

I	A HOMOGENEOUS GAS OF ULTRACOLD ATOMS WITH TUNABLE INTERACTIONS	3
1	ULTRACOLD ATOMS IN DEEP OPTICAL LATTICES	5
1.1	Optical traps for neutral atoms	6
1.1.1	Energy lightshifts	6
1.1.2	Harmonic traps	7
1.1.3	Optical lattices	9
1.2	Bose-Einstein Condensation	11
1.2.1	Condensation in a cubic box	12
1.2.2	Condensation in a harmonic potential	13
1.3	Loading Bose-Einstein Condensates in deep lattices	13
1.3.1	Bose-Hubbard model	14
1.4	Experimental setup	15
1.4.1	Magnetic equipment	15
1.4.2	Initial cooling equipment	15
1.4.3	Magnetic timeout	16
1.4.4	Evaporative cooling system	17
1.4.5	Imaging system	17
1.5	An exotic optical lattice	19
1.5.1	Intrinsic phase-stability	20
1.5.2	Loading ultracold atoms into the optical lattice	21
1.5.3	Controlling the atomic density	22
2	RYDBERG ATOMS	23
2.1	Generalities	24
2.1.1	Quantum defect theory	24
2.1.2	Rydberg lifetimes	25
2.2	Interactions between Rydberg atoms	27
2.2.1	van der Waals and dipole-dipole regimes	27
2.2.2	Rydberg blockade	28
2.2.3	Choosing the Rydberg state for our experiment	30
2.2.4	Interactions between $18S$ and nP atoms	31
2.3	Experimental production of Rydberg atoms	33
2.3.1	Two-level excitation scheme	33
2.3.2	Ultrastable cavity	33
2.3.3	Rydberg lasers	34
2.3.4	Calibrations of the Rabi frequency	35
2.3.5	Detection of Rydberg atoms	37
2.3.6	Towards experimentations	39

II	SPONTANEOUS DEPHASING IN LARGE RYDBERG ENSEMBLES	41
3	ANOMALOUS BROADENING IN LARGE RYDBERG ENSEMBLES	43
3.1	Elements of theory: Rydberg dressing	44
3.1.1	A naive approach to Rydberg dressing	44
3.1.2	Rydberg dressing in a pair of atoms	45
3.1.3	Experimental implications	47
3.2	Rydberg dressing in large ensembles	49
3.2.1	Experimental parameters	49
3.2.2	Experimental observables	49
3.2.3	Initial observations	51
3.3	Shortlisting the broadening causes	54
3.3.1	Microscopic arrangement	54
3.3.2	Lifetime measurement	55
3.4	Steady-state scalings	57
3.4.1	Van der Waals scaling	57
3.4.2	Dipole-dipole scaling	59
4	INVESTIGATIONS OF THE DYNAMICS OF THE RYDBERG POPULATIONS	63
4.1	Dynamics of the nS population	65
4.1.1	Mean-field modeling	65
4.1.2	Dynamics of the nS population	67
4.1.3	A stroboscopic experiment	69
4.2	Dynamics of the $n'P$ population	71
4.2.1	A pump-probe technique	71
4.2.2	Steady-state cross-broadening	72
4.3	Dynamical cross-broadening	76
4.3.1	Cross-broadening homogeneous mean-field model	76
4.3.2	Dynamical cross-broadening experiment	77
4.4	Possible workarounds	79
4.4.1	Stroboscopic approach	80
4.4.2	Microwave cavities	80
4.4.3	Cryogenic temperatures	82
4.5	Perspectives for Rydberg dressing	86
III	RYDBERG ATOMS IN A CRYOSTAT	87
5	DESIGNING CRYOGENIC RYDBERG EXPERIMENT	89
5.1	Arbitrary structures up to 72 atoms	90
5.1.1	Pairs of interacting Rydberg atoms	90
5.1.2	Building arbitrary arrays of microtraps	91
5.1.3	An atom-by-atom assembler	93
5.1.4	Building synthetic 3D structures	95
5.2	Towards structures of ≥ 300 atoms	95
5.2.1	Motivations	95
5.2.2	Limitations of the current setup	96
5.2.3	From UHV to XHV	98

5.3	First steps of a cryogenic assembler	101
5.3.1	A new cold atoms apparatus	101
5.3.2	Choice of a cryocooler	104
5.4	Aspheric lenses in a cryostat	106
5.4.1	Challenges	106
5.4.2	A cost-effective testing system	107
5.4.3	Thermal deformation of the mount	108
5.4.4	Stress in the lenses	110
5.4.5	Further development of the cryogenic experiment	111
IV	APPENDIX	115
A	APPENDIX A: PUBLICATION	117
B	APPENDIX B: TECHNICAL DRAWINGS FOR A FIRST OP- TOMECHANICAL MOUNT	125
	BIBLIOGRAPHY	129

Part I

A HOMOGENEOUS GAS OF ULTRACOLD
ATOMS WITH TUNABLE INTERACTIONS

The experimental platform of this thesis work consists in a homogenous frozen ideal gas of ultracold atoms.

Using a magneto-optical trap followed by evaporative cooling, we bring a thermal vapor down to quantum degeneracy (see Sec.1.2). The resulting Bose-Einstein condensate (BEC) has a macroscopic size and exhibits purely quantum properties. Because of its accessibility and tunability, this state of matter is an excellent platform to probe quantum physics[40].

Optical lattices are periodic patterns of light resulting from the interference of two or more optical beams[18]. Trapping a BEC into such a structure completely modifies its physics. In particular, increasing the depth of the lattice sites allows to observe a quantum phase transition from a superfluid to a Mott-insulator[65, 84]. In our experiment, we load the BEC into a very deep lattice, resulting in a cubic insulator close to unit filling (see Sec.1.3). The resulting sample, which has little to no interactions due to large interatomic distances ($\sim 0.5 \mu\text{m}$), is a homogeneous ideal gas of ultracold atoms. Long-range and well-controlled interactions can be added later on to the system in a process discussed Ch.2.

Over the years, the association of a BEC with optical lattices has led to a variety of experiments[17], notably including excitation into the Rydberg state[104] or periodic shaking of the optical lattice[151]. In particular, Bose gases in optical lattices have become one of the most popular platforms for quantum simulation[19] and many-body quantum experiments[20].

In this chapter, we present the generic concepts involved in the preparation of the ideal gas. We use the dressed-state picture to introduce energy lightshifts and show that they can be used to generate tailor-made trapping potentials, such as harmonic traps and optical lattices (see Sec.1.1). We briefly explain the concept of Bose-Einstein condensation (see Sec.1.2) and show how ultracold atoms in deep lattices can form an interaction-free homogenous frozen gas (See sec.1.3). We finally provide a brief overview of our experimental apparatus (see Sec.1.4).

1.1 OPTICAL TRAPS FOR NEUTRAL ATOMS

Among the many types of atom-photon interactions, we focus here on a conservative process called energy lightshifting. Using simple arguments, we recall how light affects the energy levels of a quantum system and show how this effect can be used to spatially confine atoms.

1.1.1 ENERGY LIGHTSHIFTS

Let's consider an atom as a two-level quantum system with ground state $|g\rangle$, excited state $|e\rangle$ separated by an energy $\hbar\omega_0$.

When immersing this atom into a light field, a possible approach consists in studying the system [atoms + photons in the mode][41].

Assuming N photons with energy $\hbar\omega$, the ground state $|g, N\rangle$ has an energy $N\hbar\omega$. After absorption of a photon, the excited state $|e, N-1\rangle$ has an energy $\hbar\omega_0 + (N-1)\hbar\omega$. The interaction between the field and the atom can be written

$$\hat{V} = \frac{\hbar\Omega_1(\mathbf{r})}{2} (\hat{\sigma}_+ \hat{a} + \hat{\sigma}_- \hat{a}^\dagger) \quad (1)$$

where \hat{a} and \hat{a}^\dagger are the usual creation and annihilation operators. The excitation and decay operators $\hat{\sigma}_+$ and $\hat{\sigma}_-$ define as

$$\hat{\sigma}_+ = |e\rangle\langle g| \quad (2a)$$

$$\hat{\sigma}_- = |g\rangle\langle e| \quad (2b)$$

$\Omega_1(\mathbf{r})$ can be understood as the Rabi frequency at \mathbf{r} when only one photon is in the mode.

The interaction \hat{V} can only couple states of the dressed atom of same multiplicity,

$$\langle e, N-1 | \hat{V} | g, N \rangle = \frac{\hbar\Omega_1(\mathbf{r})}{2} \sqrt{N} \quad (3)$$

We usually define it as the Rabi frequency as Ω , where

$$\Omega(\mathbf{r}) = \Omega_1(\mathbf{r}) \sqrt{N} \quad (4)$$

In the multiplicity $\{|g, N\rangle, |e, N-1\rangle\}$, the Hamiltonian writes

$$\hat{H} = \frac{\hbar}{2} \begin{pmatrix} \Delta & \Omega(\mathbf{r}) \\ \Omega(\mathbf{r}) & -\Delta \end{pmatrix} + \varepsilon_N \quad (5)$$

with $\varepsilon_N = (N-1/2)\hbar\omega + \hbar\omega_0/2$ and $\Delta = \omega - \omega_0$. We introduce the mixing angle $\vartheta(\mathbf{r})$ as

$$\cos(2\vartheta(\mathbf{r})) = \frac{\Delta}{\sqrt{\Delta^2 + \Omega^2(\mathbf{r})}} \quad \sin(2\vartheta(\mathbf{r})) = \frac{\Omega(\mathbf{r})}{\sqrt{\Delta^2 + \Omega^2(\mathbf{r})}} \quad (6)$$

The eigenvectors of the previous hamiltonian define as

$$|1(N)\rangle = \cos(\vartheta)|g, N\rangle + \sin(\vartheta)|e, N-1\rangle \quad (7a)$$

$$|2(N)\rangle = \sin(\vartheta)|g, N\rangle + \cos(\vartheta)|e, N-1\rangle \quad (7b)$$

The energies associated to these eigenstates write

$$E_N(\mathbf{r}) = \pm\varepsilon_N \pm \frac{\hbar}{2}\sqrt{\Delta^2 + \Omega^2(\mathbf{r})} \quad (8)$$

where $+$ is for the higher level and $-$ is for the lower level.

As we can see from Eq.(8), the energy levels are shifted by the interaction. This light-induced modification of the eigenenergies is usually referred as lightshifting. In the limit of large detunings $|\Delta| \gg |\Omega(\mathbf{r})|$, the lightshift writes

$$V(\mathbf{r}) = \mp \frac{\hbar\Omega^2(\mathbf{r})}{4\Delta} \quad (9)$$

where $-$ is for the higher level and $+$ is for the lower level. As far as the ground state is concerned, the lightshift lowers the energy for red-detuned light $\Delta < 0$ and increases it for blue-detuned light $\Delta > 0$.

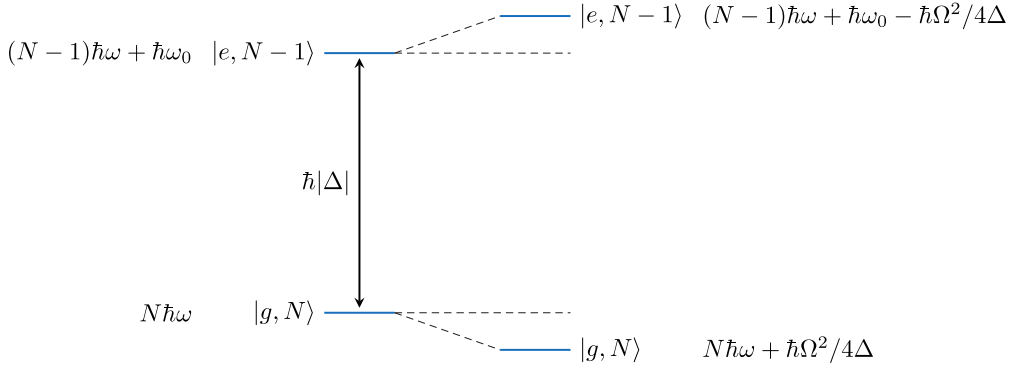


Figure 1 – **Energy lightshift**

Shifting of the energy levels of a two-level quantum system in the red-detuned case ($\Delta < 0$).

1.1.2 HARMONIC TRAPS

Atoms tend to localize at the minimum of their ground state energy. Combining this behavior with energy lightshifts, it is possible to induce forces and create trapping potentials with light. One of the simplest manner to engineer such trap consists in using a tightly focused gaussian beam.

In the semi-classical approach, the Rabi frequency can be directly related to the electric field

$$\hbar\Omega(\mathbf{r}) = -d_0\mathcal{E}(\mathbf{r}) \quad (10)$$

where d_0 is the atomic dipole moment and $\mathcal{E}(\mathbf{r})$ the amplitude of the electric field at position \mathbf{r} .

The irradiance of a tightly focused laser beam propagating along z writes

$$I(r, z) = I_0 \left(\frac{w_0}{w(z)} \right)^2 \exp \left(-\frac{2r^2}{w(z)^2} \right) \quad (11)$$

where $r^2 = x^2 + y^2$, w_0 is the waist of the beam and $w(z)$ its $1/e^2$ diameter at position z , which writes

$$w(z) = w_0 \sqrt{1 + (z/z_R)^2} \quad (12)$$

where z_R is the Rayleigh length and writes

$$z_R = \frac{\pi\omega_0^2}{\lambda} \quad (13)$$

Introducing the impedance of free space η , the Rabi frequency corresponding to a gaussian beam can be written

$$\Omega^2(\mathbf{r}) = \frac{d_0^2 I(\mathbf{r})}{2\eta\hbar^2} \quad (14)$$

Combining Eq.(9), (11) and (14) and assuming $r^2 \ll w_0^2$, the energy shift of the atomic ground state induced by a gaussian beam writes

$$V_{\text{harm}}(r, z) = V_0 \left(\frac{w_0}{w(z)} \right)^2 \left(1 - 2\frac{r^2}{w(z)^2} \right) \quad (15)$$

where $V_0 = d_0^2 I_0 / (8\Delta\eta\hbar)$.

In the case of a red-detuned laser ($\Delta < 0$), the potential is minimum at $\mathbf{r} = \mathbf{0}$, so that the atoms localize at the maximum of intensity (see Fig.2).

The trap depth is given by $V_{\text{harm}}(r = 0, z = 0)$. In the case of cold atoms, $kT \ll V_0$, so that the atoms gather at the center of the trap. The dipole potential can be approximated as a harmonic oscillator

$$V_{\text{harm}}(r, z) = -V_0 \left[1 - 2 \left(\frac{r}{\omega_0} \right)^2 - \left(\frac{z}{z_R} \right)^2 \right] \quad (16)$$

This type of trap is usually anisotropic and characterized by its trapping frequencies, which define as $\omega_r = (4V_0/m\omega_0^2)^{1/2}$ and $\omega_z = (2V_0/mz_R^2)^{1/2}$

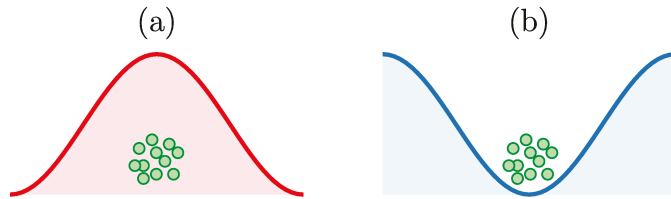


Figure 2 – **Red and blue detuned harmonic traps**

- (a) Atoms localize at the maximum intensity in a red-detuned trap,
 (b) Atoms localize at the minimum of intensity in a blue-detuned trap.

where m stands for the atomic mass, $m = 86.91 \text{ u} (= 1.44 \times 10^{-22} \text{ g})$ for ^{87}Rb .

Another experimental setting is the ratio I/Δ , where I is the intensity of the light. It is simple to show that spontaneous emission scales a $\Gamma_{\text{sc}} \propto (\Gamma/\Delta)^2 I/I_{\text{sat}}$ whereas the trapping depth varies as $V \propto (\Gamma/\Delta) I/I_{\text{sat}}$, where Γ is the natural linewidth of the transition[67]. Spontaneous emission, which leads to heating of the sample, is overall harmful and should be limited as much as possible. The usual solution consists in maximizing both I and Δ , so that V remains constant but Γ_{sc} goes to zero.

1.1.3 OPTICAL LATTICES

The interference pattern of two contrapropagating waves can be used to engineer an optical lattice, *ie.* a potential that varies periodically in space. Two gaussian beams interfering with each other create a periodic arrangement of light maxima in which the atoms can localize.

Assuming a wave propagating along \mathbf{e}_x , $\mathcal{E}_1(x, t) = \mathcal{E}_0 \sin(k_x x - \omega t + \phi_1)$ and a wave of same intensity propagating in the opposite direction, $\mathcal{E}_2(x, t) = \mathcal{E}_0 \sin(k_x x + \omega t - \phi_2)$, the resulting interference can be written

$$\mathcal{E}(x, t) = 2\mathcal{E}_0 \sin(k_x x - \Phi) \cos(2\omega t - \varphi) \quad (17)$$

where $\Phi = (\phi_1 + \phi_2)/2$ and $\varphi = (\phi_1 - \phi_2)/2$. The wavevector k_x relates to the optical wavelength $k_x = 2\pi/\lambda$.

Here we note that modulating the phase $\Phi = \Phi(t)$ would result in a time-dependent motion of the interference pattern. As a matter of fact, periodic modulations open a wide range of very interesting experimental possibilities, including Floquet engineering[48]. While this type of physics has not been investigated in this thesis, I have built the necessary equipment to perform such experiments with the JQI apparatus. The resulting publication is presented in App.A.

For the remaining of our development, we will consider $\Phi = 0$. From Eq.(17), the standing wave produces a modulation of the ground state energy

$$V_{\text{latt},1d}(x) = V_0 \sin^2(k_x x) \quad (18)$$

In the case of two waves propagating along the same axis, $k_x = 2\pi/\lambda$ and the fringe spacing defines as $i_0 = \lambda/2$. Introducing an angle θ between the two beams leads to a reduction of the wavevector, $k_x(\theta) = k_x \sin(\theta/2)$ and an increase of the interfringe, $i(\theta) = i_0 / \sin(\theta/2)$ (see Fig.3).

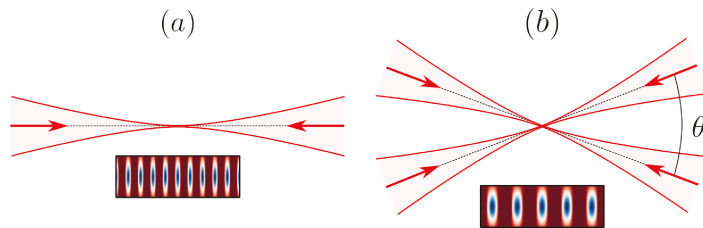


Figure 3 – **Lattice spacings**

(a) Two contra-propagating beams crossing at 180° lead to a $\lambda/2$ intersite distance, (b) Beams crossing at a lower angle lead to an increase of the lattice spacing.

The trapping depth is usually expressed in units of energy recoil E_r ,

$$E_r = \frac{\hbar^2 k_x^2}{2m} \quad (19)$$

The passage to higher dimensionalities can be done by superimposing several unidimensional lattices on top of each other. In the three-dimensional case, the resulting electric field writes

$$V_{3d}(\mathbf{x}) = V_x \sin^2(k_x x) + V_y \sin^2(k_y y) + V_z \sin^2(k_z z) + \frac{m}{2} \left(\omega_x^2 x^2 + \omega_y^2 y^2 + \omega_z^2 z^2 \right) \quad (20)$$

The last term of the previous equation corresponds to the contribution of the harmonic trap. The combination of the lattice with an optical dipole trap leads to inhomogeneities in the trapping potential — the center is deeper than the sides[17].

A precaution must be taken here: cross-interferences between the sublattices are usually undesirable and must be eliminated. In practice, several techniques are possible. The most popular consists in shifting the frequency of the sublattices, so that $2\pi(\nu_x - \nu_y) \gg \omega_{i,\text{latt}}$. In practice, $|\nu_x - \nu_y| \gtrsim 5 \text{ MHz}$ is usually sufficient. Another technique consists in crossing the polarization: assuming that the two sublattices form exactly a 90° angle, their cross-interference can be eliminated by setting their polarizations orthogonally. As we will see later, both techniques are used on the apparatus.

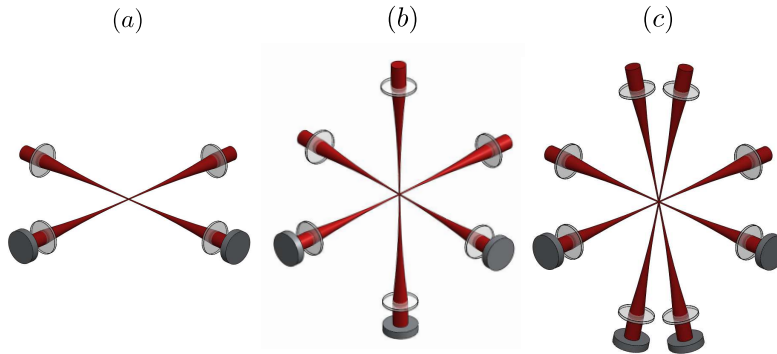


Figure 4 – **Examples of optomechanical setups for optical lattices**

Two independent crossed beams lead to an array of tubes (a), adding a third pair of beams produces a tridimensional array (b). The vertical spacing can be magnified by crossing the vertical beams at a non-zero angle (c). The lasers beams are in red, the mirrors in dark grey, the lenses in light gray.

1.2 BOSE-EINSTEIN CONDENSATION

Optical and magnetic trapping allow to cool neutral atoms to extremely low temperatures. Starting in the middle of the 1980s, remarkable advances in these techniques led to the discovery of a new phase of matter: Bose-Einstein condensates.

In this section, we show that bosons exhibit a gregarious behavior at low temperature and that a significant fraction of a bosonic ensemble can reach quantum degeneracy. This process, called Bose-Einstein Condensation, was initially predicted by S. Bose and A. Einstein in 1924[22, 49]. A major argument of the theory is the *indistinguishability* of bosons, a property that implies strong deviations from Boltzmann statistics. Producing a Bose-Einstein Condensate requires extremely low temperatures, a condition that can be met with optical traps.

The canonical derivation of Bose-Einstein condensation involves statistical mechanics and thermodynamics[40]. The starting point of the demonstration consists in evaluating the average occupancy of a state j with energy E_j for a bosonic sample of N particles at temperature T and chemical potential μ . This number is given by the Bose-Einstein law, which writes[66]

$$N_j = \frac{1}{e^{(E_j - \mu)/k_B T} - 1} \quad (21)$$

1.2.1 CONDENSATION IN A CUBIC BOX

Assuming a homogenous ideal gas of N identical bosons of mass m in a cubic box of typical size L , the eigen-states are plane waves characterized by their impulsion $\mathbf{p} = \hbar\mathbf{k}$ and eigen-energies

$$E_{\mathbf{p}} = \frac{|\mathbf{p}|^2}{2m} \quad (22)$$

with

$$\mathbf{p} = \frac{2\pi\hbar}{L}\mathbf{n} \quad (23)$$

with $\mathbf{n} = (n_x, n_y, n_z) \in \mathbb{Z}^3$. The ground state corresponds to $\mathbf{p} = \mathbf{0}$ and $E_{\mathbf{0}} = 0$.

Using Eq.(21), it is possible to evaluate the average number of particles in the state p and

$$N_{\mathbf{p}} = \frac{1}{e^{(E_{\mathbf{p}} - \mu)/k_B T} - 1} \quad (24)$$

and the total number of particles

$$N = \sum_{\mathbf{p}} N_{\mathbf{p}} \quad (25)$$

For each $N_{\mathbf{p}}$ to be positive, Eq.(24) imposes $\mu < E_{\mathbf{0}}$. Since the condensation corresponds to a gathering in the state of lowest energy, we decompose the total number of particles between the ones in the ground state ($N_{\mathbf{0}}$) and the ones in all excited states (N_{exc}). We find

$$N_{\mathbf{0}} = \frac{Z}{1 - Z} \quad (26)$$

with the fugacity $Z = \exp(\mu/k_B T)$. Since μ is negative, $0 < Z < 1$. This implies an upper boundary for N_{exc} .

$$N_{\text{exc}} < N_{\text{exc}}^{(\text{max})}(T) = \sum_{p \neq 1} \frac{1}{\exp(E_{\mathbf{p}}/k_B T) - 1} \quad (27)$$

In three dimensions, this sum is finite. Bose-Einstein condensation is predicted by this very upper boundary: one expect a gathering of $N_{\mathbf{0}}(T) = N - N_{\text{exc}}^{(\text{max})}(T)$ particules in the ground state. This result is a major deviation from Boltzmann statistics, which only predicts an accumulation of particles in the ground state in the absence of thermal activation.

1.2.2 CONDENSATION IN A HARMONIC POTENTIAL

The previous reasoning can be applied to many types of potentials such as harmonic potentials.

Assuming a harmonic trap with typical trapping frequency $\bar{\omega} = (\omega_x\omega_y\omega_z)^{1/3}$, the corresponding energy levels are non-degenerate. We enumerate them using the index $j \in \mathbb{N}$, which leads to their energies

$$E_j = \left(j + \frac{1}{2}\right) \hbar\bar{\omega} \quad (28)$$

The condition $\mu < E_0$ now becomes $\mu < 3\hbar\bar{\omega}/2$. The upper bound for the number of excited states becomes

$$N_{\text{exc}}^{(\text{max})}(T) = \sum_{n_x, n_y, n_z \neq 0} \frac{1}{\exp[\hbar(\omega_x n_x + \omega_y n_y + \omega_z n_z)/k_B T] - 1} \quad (29)$$

When increasing the number of particles ($N \rightarrow \infty$), the level spacing becomes smaller and smaller, so that the previous sum can be replaced by an integral,

$$N_{\text{exc}}^{(\text{max})}(T) = \iiint_0^\infty \frac{dn_x dn_y dn_z}{\exp[\hbar(\omega_x n_x + \omega_y n_y + \omega_z n_z)/k_B T] - 1} \quad (30)$$

The previous integral reduces to

$$N_{\text{exc}}^{(\text{max})}(T) = \zeta(3) \left(\frac{k_B T}{\hbar\bar{\omega}}\right)^3 \quad (31)$$

With this, we can extract the critical temperature of condensation, T_c ,

$$k_B T_c = 0.94 \hbar\bar{\omega} N^{1/3} \quad (32)$$

T_c typically variates from a few μK to a few hundreds of nK depending on N and $\bar{\omega}$.

1.3 LOADING BOSE-EINSTEIN CONDENSATES IN DEEP LATTICES

Bose-Einstein condensates are usually produced in harmonic traps. Due to the harmonic confinement, the density profile is gaussian. Atoms also interact with each other, mostly via two-body collisions. In this part, we show that confining ultracold atoms in an optical lattice can lead to the production of a homogeneous ideal gas of ultracold atoms.

For the purpose of this thesis, we require an ensemble of ultracold atoms free of any interactions and uniformly distributed in space. One way to do it consists in loading a Bose-Einstein Condensate into a deep optical lattice using the superfluid to Mott-insulator transition. In this process, we load one atom per site, each lattice site being separated by $\sim \lambda/2$. Such distances are typically much larger than interatomic interactions ranges between atoms in the ground state, the gas is therefore free of interactions.

1.3.1 BOSE-HUBBARD MODEL

Ultracold atoms in optical lattices can be described by the Bose-Hubbard Hamiltonian, which writes

$$\hat{H} = -J \sum_{\langle i,j \rangle} \hat{a}_i^\dagger \hat{a}_j + \sum_i (\varepsilon_i - \mu) \hat{n}_i + \frac{1}{2} U \sum_i \hat{n}_i (\hat{n}_i - 1) \quad (33)$$

where J is the hopping term capturing the tunneling of bosons between the traps and U is the onsite energy. This term is related to the scattering length from contact interactions. μ is the chemical potential, $\varepsilon_i = V_{\text{harm}}(\mathbf{r}_i)$ a correcting factor that takes in account the inhomogeneities in the external trapping potential. In our case, this term captures the curvature of the harmonic trap.

In the limit $J \gg U$, the atoms are delocalized over the entire lattice and the sample is superfluid. On the contrary, when $U \gg J$, the atoms become strongly confined and the tunneling is negligible. It is possible to show that under these conditions, the configuration that minimizes the energy corresponds to unit filling: each site is occupied by only one atom for an appropriate density. This state is called the Mott-insulator phase.

Both regimes minimize the energy of the system: it is possible to connect them adiabatically by slowly increasing the ratio U/J , *i.e.* progressively increasing the optical lattice depth. Experimentally, the depth is controlled by the optical power of the lattice light: higher optical power results in deeper optical lattice depths. A Mott insulator can thus be produced by performing an adiabatic passage from the superfluid to the Mott insulator phase by progressively ramping up the optical power of the lattice light.

Superfluid and Mott-insulator phases are not specific to quantum gases: superfluidity has been encountered in ^4He [89] and the Mott insulator has been originally developed to explain anomalous insulation in metal oxides[116].

1.4 EXPERIMENTAL SETUP

This section is dedicated to the experimental setup developed at JQI. The apparatus involves generic methods to cool atoms down to quantum degeneracy. The experiment was first built in the 2000s[102] but went through deep modifications ten years after[32]. Notably, the entire apparatus was moved from the NIST (Gaithersburg, MD) to the JQI at University of Maryland (College Park, MD) in October 2015. The reconstruction started shortly before my arrival at JQI. During my first months in the team, I participated to the assembly of the scientific features (notably the Rydberg setup, described in Chapter 2 and the optical superlattice).

As far as BEC production is concerned, the apparatus is a relatively standard machine. Yet, two major peculiarities deserve to be pointed out:

1. The experiment uses a magnetic trap as a reservoir for a dipole trap. This system enables to overcome the usual magnetic trap limitations (notably Majorana spin-flip losses[28]) as well as those of the far-detuned dipole trap (need for prohibitively high laser power).
2. Contrary to most BEC sequences, the BEC is held in a purely magnetic trap for a relatively long time (~ 1 s) before the evaporative cooling. This “dark” stage allows to move bulky optical components and switch laser beams during this time.

1.4.1 MAGNETIC EQUIPMENT

The main chamber is a standard spherical octagon equipped with two independent sets of coils (see Fig.5). The top and bottom windows are recessed.

A pair of anti-Helmoltz coils oriented along the vertical axis (\mathbf{z}) and placed under vacuum generates a magnetic quadrupole. Under typical conditions, $\partial_{\mathbf{z}}B = 0.12 \text{ T m}^{-1}$ for the MOT, and $\partial_{\mathbf{z}}B = 0.48 \text{ T m}^{-1}$ for the magnetic trap. Three additional pairs of coils are oriented along the main axes ($\mathbf{x}, \mathbf{y}, \mathbf{z}$). Each pair is in the Helmholtz configuration and can produce a small magnetic shift.

1.4.2 INITIAL COOLING EQUIPMENT

After being slowed down by a Zeeman slower, atoms enter the chamber from the left port and are captured by a magneto-optical trap (MOT) constituted of six independent laser beams in (see Fig.6) ~ 5 cm diameter. Under typical conditions, the slower laser and the Zeeman repumping lasers are respectively set to 30 mW and 15 mW. Once optimized, the MOT captures $N = 9 \times 10^8$ atoms in 3 s. The temperature of the cloud reaches 30 μK after polarization gradient cooling[42].

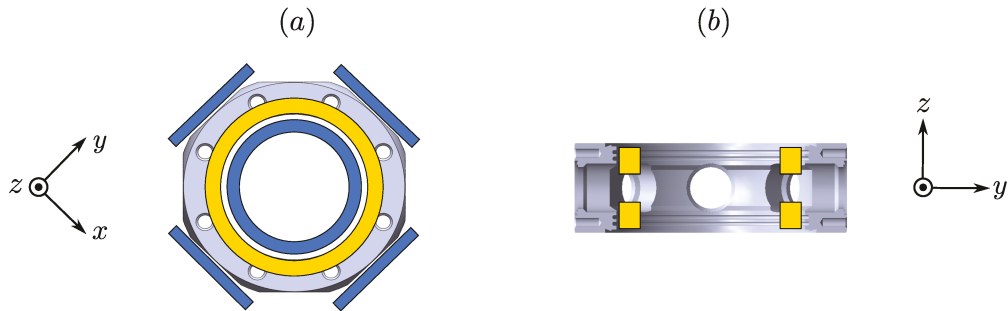


Figure 5 – **Sketch of the main chamber**

The chamber (in gray) is equipped with a pair of anti-Helmholtz coils along the vertical axis (in yellow) and three pairs of shim coils (in blue) along $(\mathbf{x}, \mathbf{y}, \mathbf{z})$. (a) Top view of the main chamber, (b) focus on the quadrupole coils installed under vacuum.

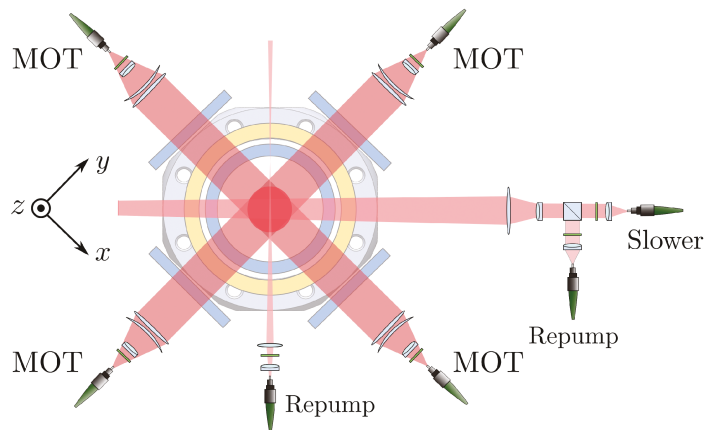


Figure 6 – **Sketch of the MOT optics**

The Zeeman beams are combined with a polarizing beam splitter (PBS). The magneto-optical trap is constituted of six independent laser beams. The repumping beam for the MOT is provided by an independent source.

1.4.3 MAGNETIC TIMEOUT

Lack of optical access is a common issue in BEC production. Large MOT beams tend to reduce the loading time but can limit optical access for the other beams.

Some experiments take this issue as an opportunity to separate the apparatus in two chambers: the MOT chamber and the BEC chamber. Using a relatively low diameter nipple between the two allows to set a high differential pressure. The partially cooled cloud is generally magnetically transferred from one chamber to the other[64]. Despite their elegance, these systems can be difficult to engineer, especially on the magnetic side.

In comparison, the experiment at JQI uses a relatively simple single-chamber design (see Fig.7). All MOT beams are deflected by pneumatically actuated mirrors[31]. In upper position, the mirrors are obstructing the viewports, only allowing the MOT beams to reach the center of the chamber. In lower position, all other beams can reach the viewports.

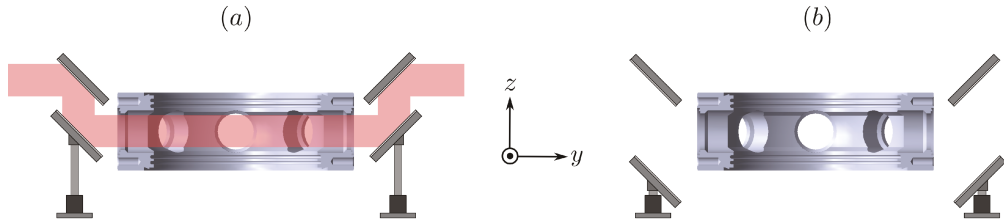


Figure 7 – **Sketch of the pneumatic mirrors**

The MOT beams are reflected by pneumatic mirrors. (a) In upper position, the MOT beams access the viewports, (b) In lower position, other beams can reach the chamber.

This technique necessitate a short time of light extinction (~ 1 s), corresponding to the mirror translation time. For this purpose, the atoms are held in a purely magnetic trap after MOT loading and before dipole trap activation.

1.4.4 EVAPORATIVE COOLING SYSTEM

The dipole trap in which evaporative cooling is performed consists of two $\lambda = 1064$ nm elliptical beams crossing at nearly 90° . These relatively high power beams (~ 25 W of total optical power) are brought to the table by high-power hollow core fibers[136]. Each beam is equipped with a small pick-off sent to a photodiode for power stabilization (see Fig.8).

The two beams are elliptical, with ellipse parameters a and b . Once focused at the center of the trap, their typical parameters are $a_1 = 30 \mu\text{m}$, $b_1 = 80 \mu\text{m}$ (Dipole 1, propagating along \mathbf{y}) and $a_2 = 70 \mu\text{m}$, $b_2 = 275 \mu\text{m}$ (Dipole 2, propagating along \mathbf{x}). Dipole 1 is typically more confining than Dipole 2, leading to unbalanced trap frequencies $\omega_x = 50$ Hz, $\omega_y = 10$ Hz and $\omega_z = 130$ Hz.

1.4.5 IMAGING SYSTEM

The experiment is equipped with two CCD cameras set to perform absorption imaging.

A Point Grey Flea 3 camera takes pictures from the side of the experiment (see Fig.9). The imaging plane is parallel to the (\mathbf{x}, \mathbf{z}) plane. With its modest performances ($5 \times 5 \mu\text{m}^2$ pixel area, 1.3 Mpx), this camera is well-suited for in-situ imaging, time-of-flight measurements and Stern-

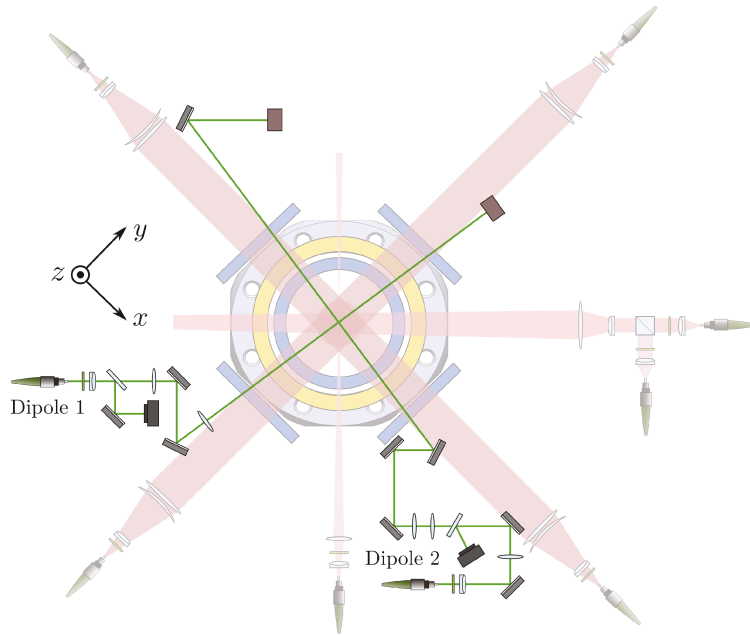


Figure 8 – **Sketch of the dipole beams**

The crossing dipole trap is constituted of Dipole 1 propagating along x and Dipole 2 along y .

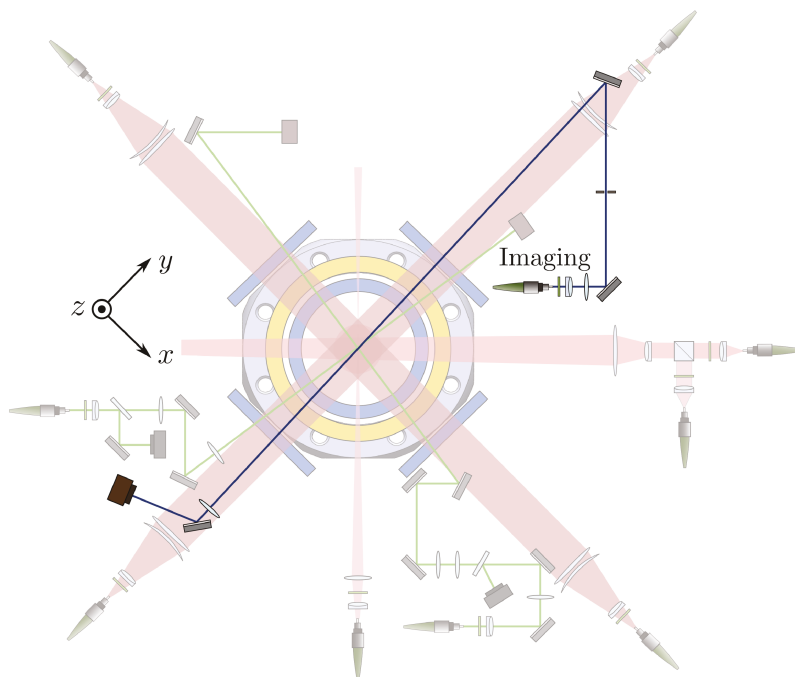


Figure 9 – **Sketch of the imaging beam**

Optical path for the Point Grey Flea 3.

Gerlach analysis.

A Princeton Instrument PIXIS takes pictures of the atoms from below. The imaging plane is parallel to the (\mathbf{x}, \mathbf{y}) plane. This camera is designed to image the atoms after a 27 ms time-of-flight (TOF). This camera is pre-

ferred for quantitative analysis such as Kapitza-Dirac measurements[62] used to calibrate the lattice depth.

Overall, a typical BEC sequence takes approximately 16 s (see Fig.10), most of the time being dedicated to the dipole evaporation. The total duration of the sequence can be slightly modified (notably the MOT loading time) depending on the quality of the vacuum pressure and the size of the BEC.

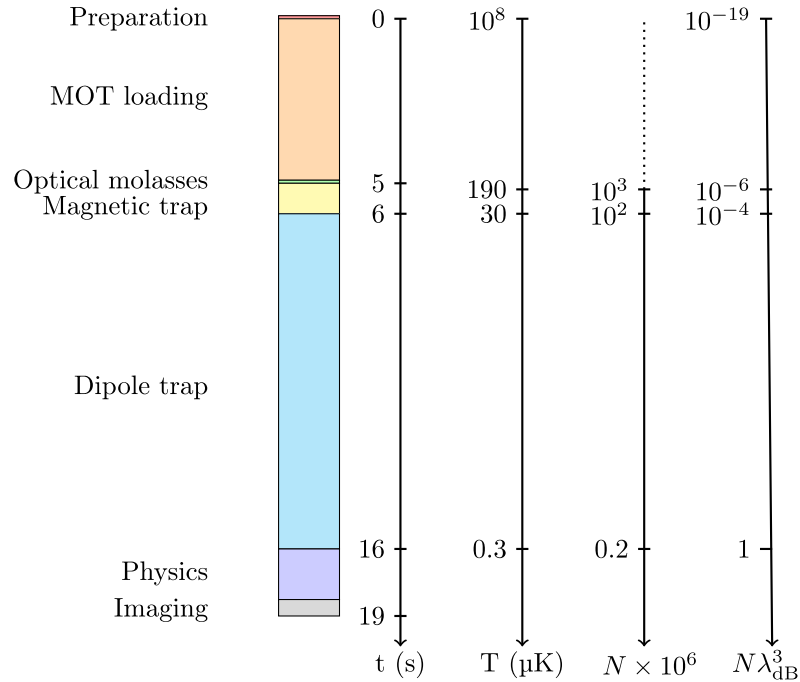


Figure 10 – Typical sequence to produce a BEC

1.5 AN EXOTIC OPTICAL LATTICE

The experiment at Joint Quantum Institute is equipped with an exotic optical lattice capable of generating pairs of double-wells[131]. Along with the other types of tunable, non-cubic lattices (*i.e.* the Zurich experiment[138]), these optical lattices are often referred as superlattices.

Contrary to usual cubic lattices, the horizontal interference pattern is produced by a single laser folded onto a retro-reflected bowtie. Controlling the polarization allows to dynamically modify the interference pattern: if the beams are polarized along the lattice plane, they can only interfere with their retro-reflexion. This leads to a standard $\lambda/2$ lattice. However, when the polarization is orthogonal to the $2d$ -plane, all beams interfere, leading to a λ lattice. The vertical interference pattern is produced by a pair of beams crossing at 20 degrees, which leads to a layer spacing of $2.34 \mu\text{m}$.

Experimentally, the system includes two Pockels-cells which can vary the polarization of the light during the experiment (see Fig.11). We use $P \approx 200$ mW of $\lambda = 813$ nm laser light, which leads to intersite spacings of 813 and 407 nm for the two sublattices.

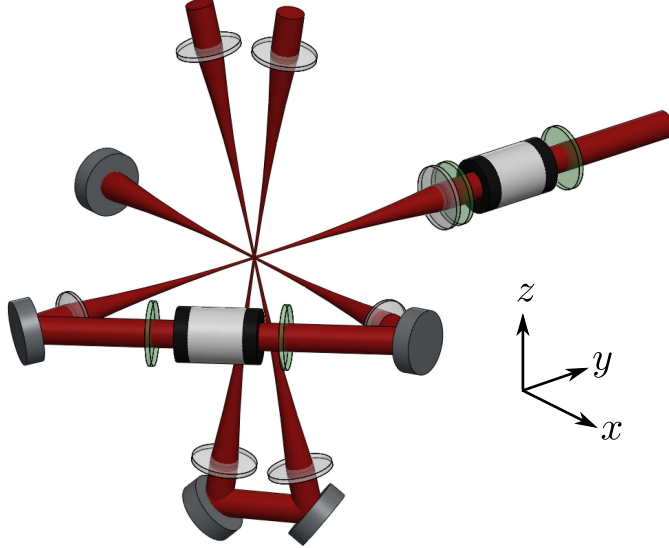


Figure 11 – **Bowtie-shaped lattice**

The relative intensity and positions of the two sublattices are controlled by two Pockels cells (Cylindrical black and white components) inserted between pairs of half-wave plates (in green).

1.5.1 INTRINSIC PHASE-STABILITY

When engineering a superlattice, spatial drifts between the sublattices are a major concern. Small dephasing between the light beams, *e.g.* due to vibrational noise in the mirrors can lead to an uncontrolled deformation of the lattice pattern.

The bowtie structure is naturally phase-stable[131]: since any dephasing affects all beams simultaneously, changing the phase translates the entire lattice without altering its structure.

The superlattice at JQI is a superposition of a $\sin^2(\lambda/2)$ lattice oriented along \mathbf{x} and \mathbf{y} and a $\sin^4(\lambda)$ lattice along $\mathbf{x} + \mathbf{y}$ and $\mathbf{x} - \mathbf{y}$,

$$I_{\text{lattice}} = \alpha I_{xy} + \beta I_z \quad (34a)$$

$$I_{xy}(x, y)/I_0 = 2 \cos(2kx - 2\theta_{xy} - 2\varphi_{xy}) + 2 \cos(2ky + 2\varphi_{xy}) + 4 \quad (34b)$$

$$I_z(x, y)/I_0 = 16 \left[\cos\left(\frac{k}{2}(x + y) - \frac{\theta_z}{2}\right) \right]^2 \left[\cos\left(\frac{k}{2}(x - y) - \frac{\theta_z}{2}\right) - \varphi_z \right]^2 \quad (34c)$$

where $\theta_{xy}, \varphi_{xy}, \theta_z, \varphi_z$ represent path length differences and $k = 2\pi/\lambda$ is the norm of the wave-vector. I_{xy} correspond to the *in-plane* situation, where the polarization of the beams is in the plane of the lattice (defined by \mathbf{x} and \mathbf{y}). Conversely, I_z is obtained when the beams are polarized along \mathbf{z} , which is orthogonal to the lattice plane.

In practice, electro-optic components (Pockels cells) are set to produce differential phase-shifts between the *in-plane* and *out-of-plane* configurations. Controlling the phase-shifts $\delta\varphi = \varphi_{xy} - \varphi_z$ and $\delta\theta = \theta_{xy} - \theta_z$ and the relative intensity I_{xy}/I_z allows to engineer a lattice of double-wells (see Fig.12). The orientation and the relative depths of the wells can be dynamically controlled by the same parameters.

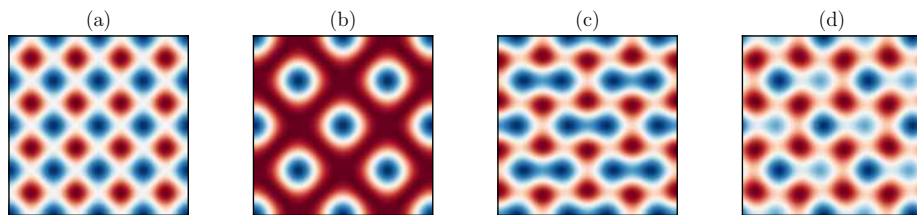


Figure 12 – **Examples of superlattices**

(a) Purely $\lambda/2$ lattice ($I_z = 0$), (b) purely λ lattice ($I_{xy} = 0$), (c) equilibrated pairs of wells ($I_{xy}/I_z = 9$, $\delta\theta = \pi/2$), (d) disequilibrated pairs of traps ($I_{xy}/I_z = 4$, $\delta\theta = \pi/3$).

Pairs of isolated dimers are a remarkable tool for quantum simulation. However, the possibilities of this superlattice have not been broadly used in this thesis work. Several earlier publications have used this tool for its true worth[93].

1.5.2 LOADING ULTRACOLD ATOMS INTO THE OPTICAL LATTICE

A typical sequence produces a condensate of $N = 4 \times 10^4$ atoms in the state $|5S_{1/2}, 1, -1\rangle$. Once the atoms reach quantum degeneracy, the sample is adiabatically loaded into the optical lattice. The power of the lattice beam is ramped up in 300 ms, reaching approximately 150 mW in the horizontal and the vertical beams.

The lattice depth is estimated by Kapitza-Dirac diffraction[62, 90] (See Fig.13). In a nutshell, the technique consists in sending a short pulse of the lattice light onto the sample and wait for the atoms to interfere. The shape and intensity of the resulting interference pattern provides informations about the geometry and depth of the optical lattice. Under typical conditions, the lattice depth is $\sim 50 - 70 E_r$.

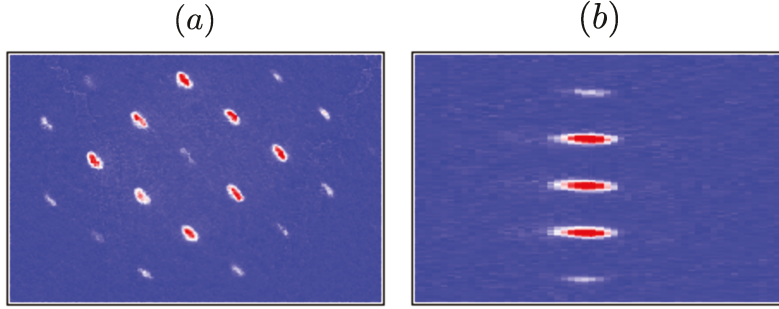


Figure 13 – **Lattice diffraction by Kapitza-Dirac**

Typical diffraction patterns of the $2d$ optical lattice (a) in the $\lambda/2$ configuration at ~ 60 Er and the vertical lattice (b). The lattice depth is extracted from the relative intensity of the diffraction orders.

1.5.3 CONTROLLING THE ATOMIC DENSITY

In its standard configuration, the optical lattice has an intersite distance of $\lambda/2 = 406$ nm leading to a density of approximately 2.5 atoms/ μm^3 . However, it is possible to empty half of the lattice sites. The resulting checkerboard structure has an intersite distance of λ and a density ≈ 0.6 atoms/ μm^3 . As we will show in Ch.3, being able to change the microscopic arrangement can help to identify the range of many-body phenomena.

The production of the checkerboard pattern takes advantage of desequilibrated double-wells and single-site addressing in a process described on Fig.14.

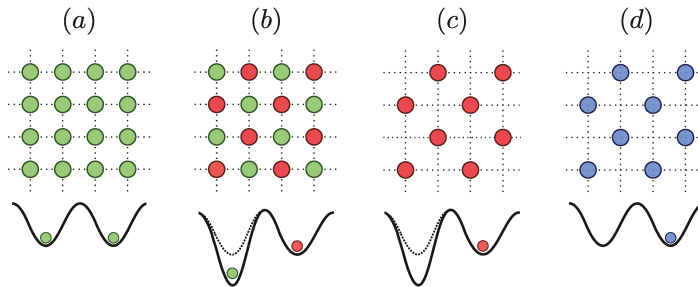


Figure 14 – **Production of a checkerboard arrangement of the lattice**

We start the procedure with a $\lambda/2$ lattice close to unit filling, atoms are in the $\bullet = |5S_{1/2}, F = 1, m_F = -1\rangle$ state (a). We use the superlattice feature to superimpose a λ modulation on top of the $\lambda/2$ lattice and create a double-wells structure. Half of the population is then transferred to the $\bullet = |5S_{1/2}, F = 2, m_F = 0\rangle$ state, which is magnetically insensitive (b). We impose a strong magnetic field gradient which blows away the magnetically sensitive population. This effectively creates the checkerboard structure (c). We go back to a pure $\lambda/2$ lattice, the populations can then be transferred to another sublevel of the $5S_{1/2}$ if needed (d).

Rydberg atoms are atoms with a high principal quantum number n , which gives them exaggerated properties[37, 53]. The remarkable behavior of Rydberg states include tunable polarizability ($\propto n^7$), long radiative lifetimes ($\propto n^3$), and extremely large interaction strength ($C_6 \propto n^{11}$), where C_6 is the van der Waals interaction coefficient. Besides, their sensibility to external fields allows to tailor their properties, notably near Förster resonances[124].

While Rydberg atoms have long been studied in hot vapors or in atomic beams, the remarkable advances in laser sources and high-resolution absorption spectroscopy now allow to study Rydberg states in cold samples. At low temperatures, the motion of the nuclei are almost frozen during the lifetime of the Rydberg states; this, combined with the extremely large interaction strength, enables direct observation and control of the interatomic interactions[12]. This has been used to measure the interaction between pairs of atoms and now constitutes the cornerstone of several many-body quantum simulators[9, 105].

Both experiments discussed in this thesis are based on cold Rydberg atoms. On one hand, the experiment at JQI investigates the dissipation of a large ensemble ($N = 40000$) of Rydberg atoms trapped in a tridimensional optical lattice. On the other hand, the LCF teams focuses on the dynamics of smaller ensembles ($N \leq 72$) in arbitrary geometries. The typical interatomic distances ($\sim 0.5 \mu\text{m}$ at JQI, $3 \mu\text{m}$ to tens of μm at LCF) play a major role in both experiment, they notably determine the Rydberg level compatible with each platform.

In this chapter, we introduce some generalities concerning the physics of Rydberg atoms and show that Rydberg excitation combined with a Bose-Einstein condensate (see Ch.1) allows to produce a gas of ultracold atoms with tunable interactions. We provide some insight concerning Rydberg lifetimes (see Sec.2.1) as well as interactions between pairs of atoms (see Sec.2.2). We motivate the choice of the $18S$ level for the experiment at JQI and provide details about this experimental setup (see Sec.2.3).

2.1 GENERALITIES

Atoms in the Rydberg state have a high principal quantum number, typically $n \geq 10$ [53]. These levels being very close to ionisation, the electron is very loosely bound to the cationic core. These states have exaggerated properties, notably in their polarizability and interaction strength.

In the semi-classical approach, an alkali Rydberg atom can be described as a single electron orbiting far away from the cationic core. The interaction between the core and the electron can be described with the usual Coulomb potential over long distances,

$$V_{\text{Coulomb}} \propto -1/r \quad (35)$$

In the classical picture, the electron has an elliptical Kepler orbit around the core, with long axis proportional to n^2 and small axis determined by the angular momentum of the valence electron l .

2.1.1 QUANTUM DEFECT THEORY

The starting point of our investigation consists in calculating the energy of the Rydberg states. One peculiarity of Rubidium (compared to Hydrogen) is the presence of other electrons in the inner shells. As long as the angular momentum l is high enough, these electrons perfectly shield the nucleus charges and the atom is hydrogen-like to a very good approximation. However, for low angular momentum (typically $l \leq 3$), the trajectory of the electron becomes very elliptical and the valence electron penetrates the higher electronic shells. The shielding is no longer perfect and corrections must be applied. This also induces a deviation from the pure coulombic potential at short ranges.

As originally noted by J.R. Rydberg himself[125], this phenomenon can be taken in account by simply applying a phenomenological correcting factor to the principal quantum number n . Quantum defect theory[130] consists in treating the Hydrogen atom problem with a non-integer principal quantum number $n_{\text{eff}} = n - \delta_{nlj}$, where δ_{nlj} defines as

$$\delta_{nlj} = \delta_{0lj} + \frac{\delta_{2lj}}{(n - \delta_{0lj})^2} + \frac{\delta_{4lj}}{(n - \delta_{0lj})^4} + \dots \quad (36)$$

where the values of δ_i are species dependent and tabulated. For nS states of ^{87}Rb , $\delta_{0nS} = 3.131$ and $\delta_{2nS} = 0.178$ [100].

From there, the energy of a Rydberg state of principal quantum number n and orbital angular momentum l is

$$E_{n,l} = -\frac{R_y}{n_{\text{eff}}^2} \quad (37)$$

With the Rydberg constant R_y ,

$$R_y = \frac{Z^2 e^4 m_e}{2(4\pi\epsilon_0 \hbar)^2} \quad (38)$$

Z is the nucleus charge, e the elementary electronic charge, m_e the mass of the electron and ϵ_0 the vacuum permittivity.

2.1.2 RYDBERG LIFETIMES

The lifetimes of Rydberg states strongly depend on their principal quantum number and typically scale as $\tau_{n_{\text{eff}}} \propto n_{\text{eff}}^3$ [53]. Longer timescales can be accessed with higher Rydberg states, but experimental difficulties (*e.g.* narrow lines, extreme sensitivity to external fields) prevent from using Rydberg states higher than $n \sim 120$. Experimentalist rather tend to use Rydberg states within the range $n = 30 - 70$, corresponding to lifetimes in the range $50 \mu\text{s} - 100 \mu\text{s}$.

These lifetimes are well suited to probe phenomena in the MHz range, such as measuring the van der Waals interaction between Rydberg atoms separated by a few microns[12]. However, other experiments require longer experimental timescales. This is notably the case of phenomena involving the mechanical response of a sample trapped in an optical trap. The typical frequencies of the optical trap being in the kHz range, experimental timescales larger than 1 ms are necessary. As we discuss in Ch.3, there has been a global effort to address issue[23, 87], notably with the aim of using Rydberg atoms for many-body quantum simulation.

Rydberg atoms decay by two majors channels: spontaneous emission and radiative transfer. When calculating the lifetime, it is common to separate the two contributions. As radiative transfers are thermally induced, the lifetime due to spontaneous emission only corresponds to the lifetime at zero-temperature. The decay rate between two states $|e\rangle$ and $|g\rangle$ with an electric dipole moment $e\langle e|r|g\rangle$ and separated by an energy $\hbar\omega_{eg}$ is given by the Einstein coefficient[105]

$$A = \frac{2e^2\omega_{eg}^3}{3\epsilon_0 c^3 \hbar} \langle e|r|g\rangle \quad (39)$$

The lifetime at zero temperature can be estimated with the empirical equation[26, 53]

$$\tau_e(0\text{ K}) = \gamma_e^{-1}(0\text{ K}) = t_S n_{\text{eff}}^\epsilon \quad (40)$$

where t_S is specific to nS states. t_S and $\epsilon \approx 3$ are specie-dependent and experimentally determined.

Numerous analyses[63, 71, 139] have provided values for the fitting parameters, namely $t_S = 1.43$ ns and $\varepsilon = 2.94$ for ^{87}Rb [53].

Radiative transfers to nearby states are characterized by the Einstein B coefficient, which defines $B = AN(\omega)$, where $N(\omega)$ is the number of photons in the mode,

$$N(\omega) = \frac{1}{e^{\hbar\omega/k_bT} - 1} \quad (41)$$

The lifetime of the state $|e\rangle$ at a temperature T , $\tau_i(T)$ is given by the sum of all contributions

$$\tau_e^{-1}(T) = \sum_f A + \sum_f AN(\omega_{ef}) \quad (42)$$

And we define the natural linewidth as $\gamma_e = \tau_e^{-1}$.

Direct computation of the lifetime is not entirely trivial. In particular, calculating the Einstein A coefficient necessitates to evaluate the radial integral of the dipole transition. This calculation can be done with several approaches, depending on the Rydberg level of interest. The Bates-Damgaard method[11] is adapted to relatively low Rydberg levels ($n \leq 15$) while the Numerov method, which works under the Coulomb approximation, captures higher Rydberg states ($n \geq 15$)[153].

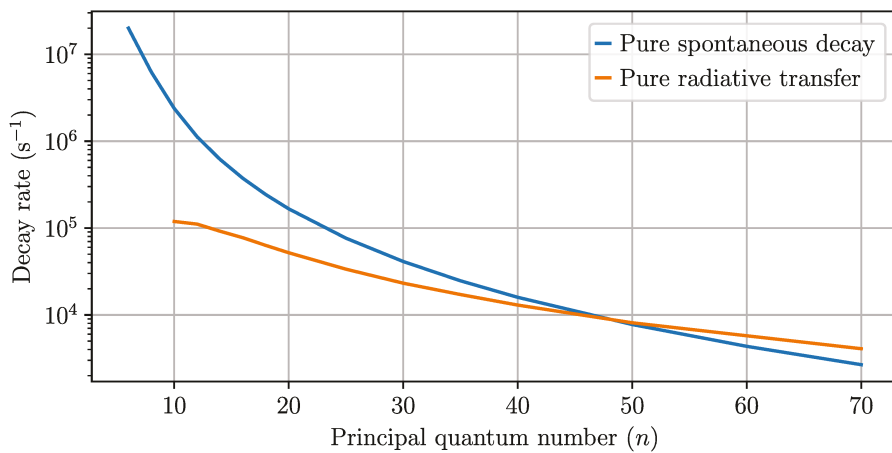


Figure 15 – **Decay rates for spontaneous emissions and purely black-body radiative transfers**

Blackbody transfers to nearby states of opposite parity dominates for large principal quantum numbers. This phenomenon is due to the reduction of the energy between adjacent states, which scales as n^{-3} .

The semi-classical approach developed by D'yachkov and Pankratov[39] is an interesting alternative as it provides orthogonal and normalized continuum wavefunctions, resulting in a better estimate of the decay rates[14].

Softwares based on this method are accessible online, notably N. Šibalić's [Alkali Rydberg Calculator \(ARC\)](#). We use this platform to calculate the decay rate as a function of the Rydberg level (see Fig.15). At $T = 300$ K, blackbody induced transfer dominate for $n \geq 48$.

2.2 INTERACTIONS BETWEEN RYDBERG ATOMS

In this section, we give some insights concerning the interactions between Rydberg atoms. Taking in account the ‘‘Rydberg blockade’’ we show that principal quantum numbers around 18 are the best suited for the JQI experiment.

2.2.1 VAN DER WAALS AND DIPOLE-DIPOLE REGIMES

Due to their strong polarizability, Rydberg atoms can have long-range interactions. In the limit where the two atoms at stake are separated by a distance R much larger than their size, the interaction potential is dominated by the dipole-dipole term[29]

$$\hat{H}_{dd} = \frac{1}{4\pi\epsilon_0 R^3} [\hat{\mathbf{d}}_A \cdot \hat{\mathbf{d}}_B - 3(\hat{\mathbf{d}}_A \cdot \mathbf{u})(\hat{\mathbf{d}}_B \cdot \mathbf{u})] \quad (43)$$

where $\mathbf{u} = \mathbf{R}/R$ is a unitary vector pointing from atom A to atom B .

The dipole matrix elements $d_{A,B}$ capture the transition from the initial Rydberg state $|r\rangle$ to the other dipole-coupled states, $|r'\rangle$ and $|r''\rangle$. We introduce the Förster defect, which corresponds to the energy difference between the dipole-coupled pairs,

$$\delta_F = E_{r'} + E_{r''} - 2E_r \quad (44)$$

The largest contribution to \hat{H}_{dd} corresponds to the potential given by the pair state that minimizes $|\delta_F|$. In general, the coupling is dominated by one two-atom state, so that the problem simply reduces to a two-level system. Typically, the energy difference between $|ns, ns\rangle$ and $|np, (n-1)p\rangle$ is usually much smaller than any other two-atom state, so that the problem reduces to the coupling $|ns, ns\rangle \leftrightarrow |np, (n-1)p\rangle$.

The Hamiltonian of the two atoms reduced in the basis $|np, (n-1)p\rangle$ writes

$$\mathcal{H} = \begin{pmatrix} 0 & C_3/R^3 \\ C_3/R^3 & \delta_F \end{pmatrix} \quad (45)$$

with eigenvalues

$$\Delta E_{\pm} = \frac{\delta_F}{2} \pm \frac{1}{2} \sqrt{\delta_F^2 + 4 \left(\frac{C_3}{R^3} \right)^2} \quad (46)$$

This leads to two asymptotic behaviors depending on R . In the limit $C_3/R^3 \ll \delta_F$, the $|ns, ns\rangle$ and $|np, (n-1)p\rangle$ states are hardly admixed. The energy levels are shifted by

$$\Delta E_{ns,ns} \approx \frac{1}{4\delta_F} \left(\frac{C_3}{R^3}\right)^2 = \frac{C_6}{R^6} \quad (47)$$

This is the van der Waals regime. In practice, the state $|nl, nl\rangle$ can be coupled to many other $|n'l', n''l''\rangle$ states, where previous reasoning was only taking in account the largest contribution. A better estimation consists in summing the contribution of each coupling. The result yields the C_6 coefficient,

$$C_{6nl} = \sum_{n'l'n''l''} \frac{|\langle nl, nl|V(R)|n'l', n''l''\rangle|^2}{\delta_F(n'l'n''l'')} \quad (48)$$

For $18S$, $C_6(18S) = 27 \text{ kHz } \mu\text{m}^6$. It is quite clear that $C_6 \propto n_{\text{eff}}^{11}$, as on one hand, we have $C_3 \propto d^2 \propto n_{\text{eff}}^4$; on the other hand, $\delta_F \propto n_{\text{eff}}^3$, yielding to the n_{eff}^{11} scaling.

When $C_3/R^3 \gg \delta_F$, the two states are strongly admixed and the two eigenenergies of the Hamiltonian become

$$\Delta E_{\pm} \approx \pm \frac{C_3}{R^3} \quad (49)$$

where the states are $|\pm\rangle = (|ns, ns\rangle \mp |np, (n-1)p\rangle)/\sqrt{2}$. This is the dipole-dipole regime.

The transition between the van der Waals and dipole-dipole regimes occurs at the van der Waals radius, which defines as

$$R_{\text{vdW}} = (C_6/|\delta_F|)^{1/6} \quad (50)$$

2.2.2 RYDBERG BLOCKADE

The interaction between Rydberg atoms can lead to extreme energy shifts. This can lead to a “blockade”, in which the presence of one Rydberg atom prevents its neighbors from being excited.

Considering a system of two atoms A and B separated by a distance R , the two-atom pair can be described by four different states, $|g, g\rangle$, $|g, r\rangle$, $|r, g\rangle$ and $|r, r\rangle$, where $|g\rangle$ represents the ground state and $|r\rangle$ the Rydberg state. Assuming the van der Waals regime, we expect the state $|r, r\rangle$ to be shifted by an energy U_{vdW} , the shifting of the other states being negligible. As a consequence, a laser tuned on resonance with one of the atoms will become off-resonant with the other atom. This is the phenomenon of “Rydberg blockade”, in which the excitation of one atom to the Rydberg state prevents the other one from being excited.

Driving the Rydberg transition results in the excitation of a superposition of states

$$|\psi_+\rangle = \frac{1}{\sqrt{2}} (|r, g\rangle + |g, r\rangle) \quad (51)$$

In the blockaded regime, the system undergoes a Rabi oscillation with frequency of $\sqrt{2}\Omega$ between the states $|g, g\rangle$ and $|\psi_+\rangle$, where Ω defines as the Rabi frequency of the single atom, $\Omega = dE/\hbar$.

On crucial parameter is the “blockade radius”, which defines as

$$R_b = \left(\frac{C_6}{\hbar\Omega} \right)^{(1/6)} \quad (52)$$

In the case of N atoms within the blockade sphere, the system oscillates between the collective ground state $|g, g, g, \dots, g\rangle$ and the collective excited state

$$|\psi_c\rangle = \frac{1}{\sqrt{N}} \sum_{i=1}^N |g, g, \dots, r_i, \dots, g\rangle \quad (53)$$

at a frequency $\Omega_c = \sqrt{N}\Omega$.

The physics of the blockaded regime is very rich and is an interesting platform to engineer many-body quantum systems. This phenomenon has been used in many experimental works, such as the production of C-NOT quantum gates and quantum information processing[85, 126, 141].

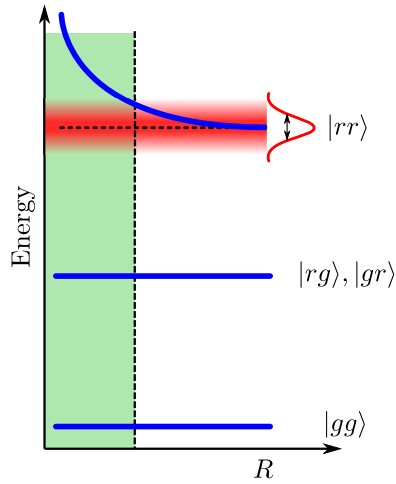


Figure 16 – **Blockade regime**

The blockaded regime (in green) occurs when the interaction potential (solid blue line) becomes larger than the laser linewidth (in red).

2.2.3 CHOSING THE RYDBERG STATE FOR OUR EXPERIMENT

The choice of the Rydberg level is driven by the interaction strength. Since we aim to excite all atoms into the Rydberg state, the blockade regime must be avoided. As the interatomic distance between the atoms is fixed by the optical lattice (see Ch.1), this imposes an upper limit to the Rydberg level we can use. At the same time, one must choose the highest possible Rydberg state in order to maximally benefit from the large interaction strength. A practical solution consists in matching the intersite distance with the blockade radius, $a \approx R_b$.

We calculate the C_6 coefficients and the natural linewidth of the $n \in [15, 21]$ S states using the [ARC Jupyter notebook](#) introduced in Sec.2.1.1. We find that the highest Rydberg level with blockade radius lower than the intersite distance is $18S$ (see Fig.17).

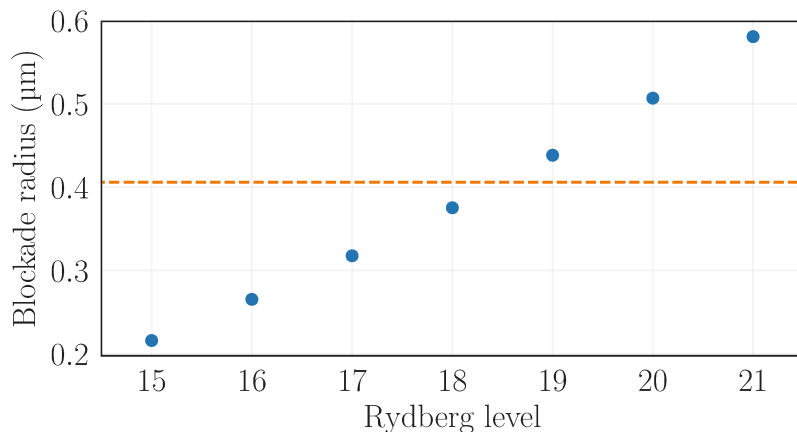


Figure 17 – **Choosing an adapted Rydberg level**

We compare the intersite distance (dashed orange line) to the blockade radius associated with the $n \in [15, 21]S$ states. The $18S$ level combines a maximum interaction strength with a blockade radius smaller than the intersite distance.

Using the ARC, we find $C_6(18S) = 27.17 \text{ kHz } \mu\text{m}^6$. From Sec.2.1.2, we calculate the lifetime of $18S$. We estimate the lifetime at zero-Kelvin, $\tau_{18}(0 \text{ K}) = 4.0 \mu\text{s}$ and at room temperature $\tau_{18}(300 \text{ K}) = 3.3 \mu\text{s}$, leading to a natural linewidth $\Gamma_{18S}/2\pi = 48.6 \text{ kHz}$. This combined leads to $R_b(18S) = 0.38 \mu\text{m}$.

Knowing C_6 allows to evaluate R_{vdW} . Considering the coupling $|18S, 18S\rangle \leftrightarrow |18P, 17P\rangle$, we find $\delta_F = h \times -193 \text{ GHz}$, leading to $R_{\text{vdW}, 18S} = 72 \text{ nm}$. The minimum interatomic distance in the lattice being $\lambda/2 = 406 \text{ nm}$, we are well in the van der Waals limit.

2.2.4 INTERACTIONS BETWEEN $18S$ AND nP ATOMS

In Sec.2.1.2, we showed that Rydberg atoms can transfer to nearby states due to blackbody radiation. This is a well-known phenomenon, which was first observed in thermal beams in the early 1980s[38]. In particular, atoms transfer to states of opposite parity due to selection rules, meaning that a $|nS\rangle$ atom will trigger the apparition of $|n'P\rangle$ states, with $n \approx n'$. In this part, we briefly review the interaction between these states.

We have established in Sec.2.2.3 that $|nS\rangle = |18S\rangle$ is the best choice for our experiment. Assuming $T = 300$ K, we calculate the rate of the blackbody radiative transfers to nearby $|n'P\rangle$ states with the ARC Library (see Fig.18). The simulation shows that about $b = 20\%$ of the $18S$ atoms transfer to a nearby $|n'P\rangle$ state. The $|n'P\rangle$ population is mostly gathered in four states: $18P_{1/2}$, $18P_{3/2}$, $17P_{1/2}$ and $17P_{3/2}$. The remaining $1 - b$ atomic fraction decays back to the ground state.

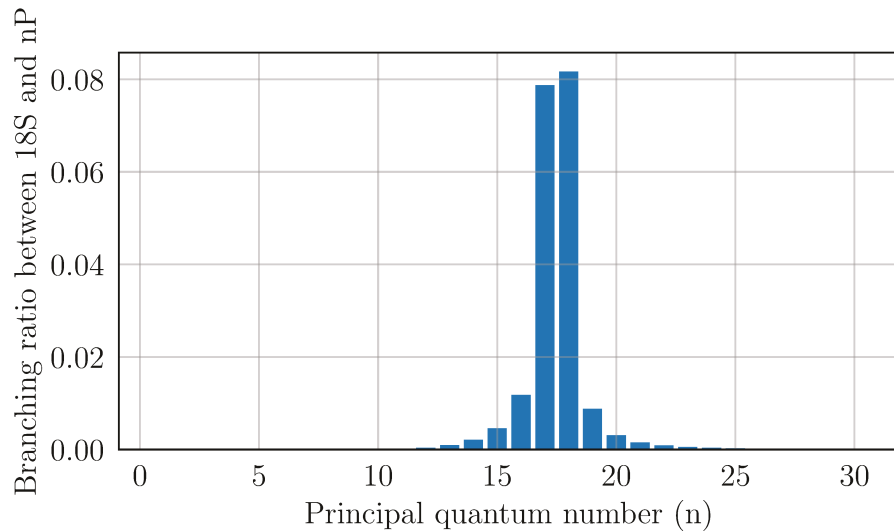


Figure 18 – **Branching ratios from $18S$ to nearby states of opposite parity**

The transfers to $18P$ and $17P$ are clearly predominant, with respectively $b_{18P} = 8.1\%$ and $b_{17P} = 7.8\%$.

The interaction between $|18S\rangle$ and the $|n'P\rangle$ states is expected to be much longer range than the one between two $|nS\rangle$ states. We evaluate the C_3 coefficients associated with these states. We find

$$\begin{aligned}
 C_3(18S_{1/2}-18P_{1/2}) &= 7.7 \text{ MHz } \mu\text{m}^3 \\
 C_3(18S_{1/2}-18P_{3/2}) &= 22.5 \text{ MHz } \mu\text{m}^3 \\
 C_3(18S_{1/2}-17P_{1/2}) &= 5.3 \text{ MHz } \mu\text{m}^3 \\
 C_3(18S_{1/2}-17P_{3/2}) &= 16.5 \text{ MHz } \mu\text{m}^3
 \end{aligned} \tag{54}$$

We take the opportunity to plot the corresponding energy shift $\Delta E = C_3/R^3$ as a function of the interatomic distance R (see Fig 19). Assuming that the blockade regime corresponds to the natural linewidth, $\Delta E \approx \Gamma_0$, the blockade radii are more than an order of magnitude larger than the intersite distance in the lattice.

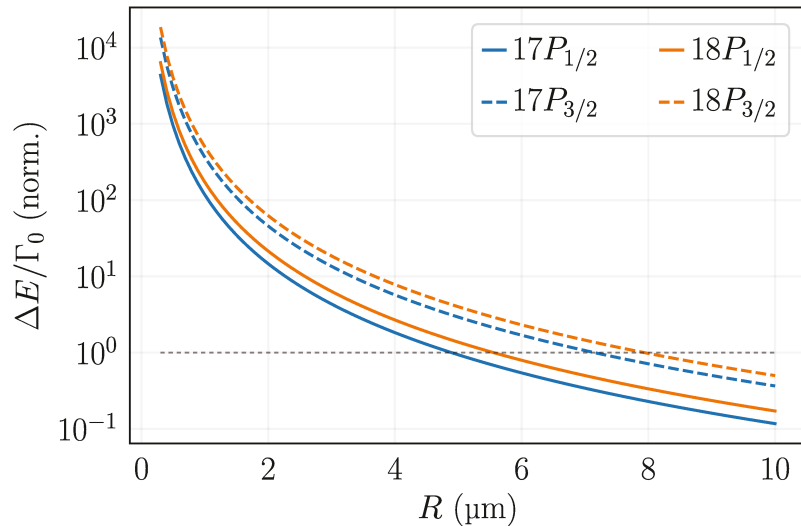


Figure 19 – **Dipole-dipole interactions between 18S and $n'P$ states**

We trace in semi-logarithmic scale the normalized energy shift $\Delta E/\Gamma_0$ as a function of the interatomic distance R . We calculate for the four principal $n'P$ states. The dashed gray line corresponds to $\Delta E = \Gamma_0$.

2.3 EXPERIMENTAL PRODUCTION OF RYDBERG ATOMS

2.3.1 TWO-LEVEL EXCITATION SCHEME

The $n = 5$ and $n = 18$ levels are approximately separated by 980 THz. Exciting this transition requires an intense source of photons at 300 nm, which can be relatively difficult to find, and expensive. We use a generic method based on a two-photon scheme, in which the transition is driven by two photons of lower energy (see Fig. 20). This allows to couple the $5S_{1/2}$ state to the $18S_{1/2}$ level.

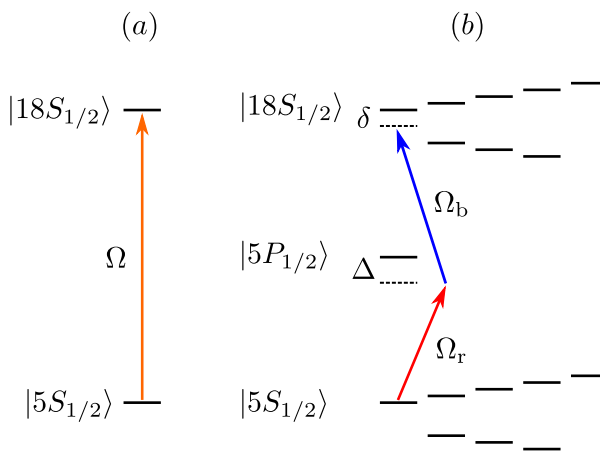


Figure 20 – **Two-photon excitation**

The Rydberg transition (a) is driven by a two-photon process (b).

We excite the $5S_{1/2} - 18S_{1/2}$ transition with intermediate state $5P_{1/2}$ state and detuning $\Delta/2\pi = 235$ MHz. We couple the $|5S_{1/2}, F = 2, m_F = -2\rangle$ and the $|18S_{1/2}, 2, -2\rangle$ levels by combining a σ_+ red photon and a σ_- blue photon. Assuming single-photon Rabi frequencies Ω_r and Ω_b , the resulting two-photon Rabi frequency is given by

$$\Omega = \frac{\Omega_r \Omega_b}{2\Delta} \quad (55)$$

The corresponding lightshift is given by

$$\Delta E = \frac{\Omega_r^2 - \Omega_b^2}{4\Delta} \quad (56)$$

2.3.2 ULTRASTABLE CAVITY

The Rydberg excitation scheme on the JQI experiment is quite conventional: both lasers are stabilized by means of a Pound-Drever-Hall lock (PDH)[16] on an ultrastable cavity. The Fabry-Pérot cavity serves as frequency reference, the error signal is based on a measurement of the light

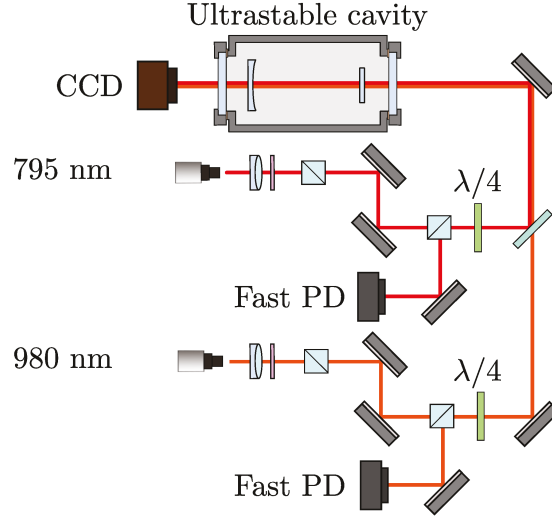


Figure 21 – **Cavity lock**

Both lasers are locked via a PDH scheme. The error signal is captured by two rapid photodiodes that measure the cavity rejection. A CCD camera provides an image of the transmission which allows to visualize the cavity mode.

rejected from the cavity (see Fig.21).

We use a hemispherical Fabry-Pérot cavity of approximate length $d = 15$ cm. The two mirrors are coated for $\lambda_r = 795$ nm and $\lambda_{2b} = 980$ nm. We estimate the linewidth of the cavity to be lower than 10 kHz. For stability purposes, the cavity is placed under vacuum and is temperature stabilized. In order to measure the laser frequency, we use a cavity-based wavemeter (HighFinesse), with precision up to a few tens of MHz: over two years, we have not seen any drift of the cavity resonance.

2.3.3 RYDBERG LASERS

2.3.3.1 RED LASER SOURCE

The light source at $\lambda_r = 795$ nm is a **Toptica DL Pro**. This Rydberg laser is divided into three outputs: the main one to the atoms, a pick-off for the lock and a very-low power output for the optical wavemeter. Its linewidth of this laser is measured by self-heterodyning[118] and is typically 150 kHz.

The experiment and the cavity work at different frequencies. We typically divide the laser into two beams, the frequency of the laser being set to the frequency of the experiment ν_{exp} while the frequency of the locking beam is tuned to the cavity resonance ν_{cav} by an electro-optic modulator (EOSpace). With our cavity, we typically have $\nu_{\text{cav}} = \nu_{\text{exp}} \pm 1.6$ GHz. Furthermore, the PDH technique requires a local oscillator, which we create with the same EOM and arbitrary set at 20 MHz (see Fig.22).

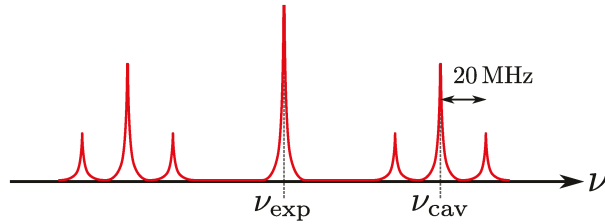


Figure 22 – **Basic diagram of the spectrum of lock input light**
(*Not to scale*).

2.3.3.2 BLUE LASER SOURCE

The blue laser ($\lambda_b = 495 \text{ nm}$) is generated by a Toptica SHG-TA Pro, which is an amplified, cavity-doubled laser diode centered on $2\lambda_b = 980 \text{ nm}$. Similarly to the red laser, this one is equipped with a two-stage frequency lock, the fast one feeding back on the diode current, the slow one on the piezo-actuated grating. The doubling cavity is controlled by a separate PDH lock which centers the resonance on the pump frequency. This PDH is fed-back by a FALC, which is a fast frequency controller provided by Toptica.

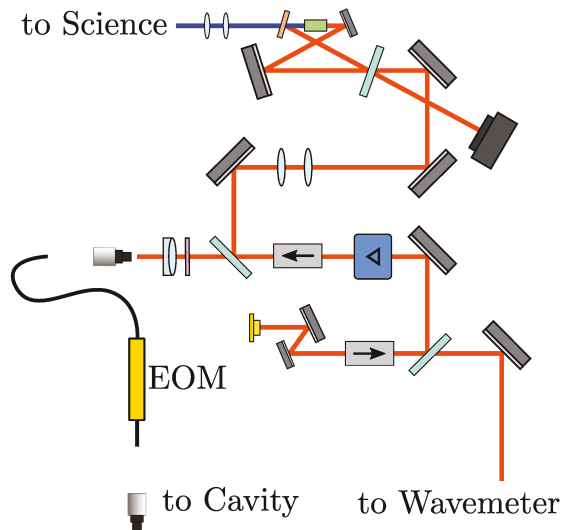


Figure 23 – **495 nm laser source**

The Rydberg blue laser is a frequency doubled and amplified $\sim 980 \text{ nm}$ laser diode. We use the pump light for the cavity lock and the frequency measurement on the wavemeter.

2.3.4 CALIBRATIONS OF THE RABI FREQUENCY

In order to characterize the driving strength, the two single-photon Rabi frequencies must be calibrated independently. In both cases, we use the lightshift (see Ch.1) to connect the single-photon Rabi frequency with the measured optical power.

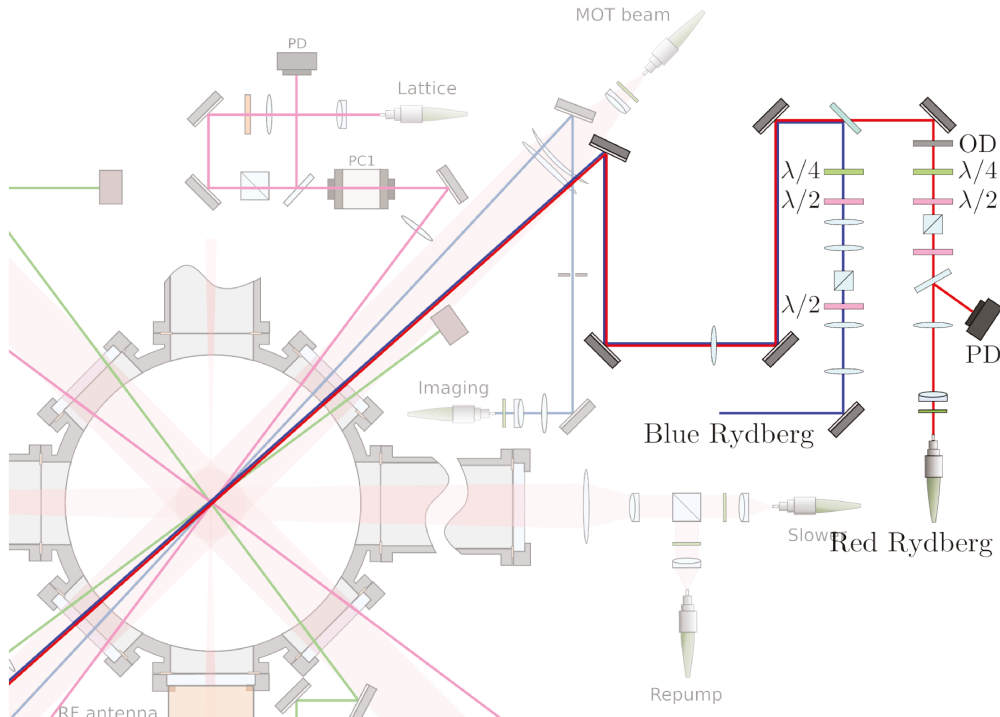


Figure 24 – **Diagram of the Rydberg beams**

The blue and red beams are combined with a dichroic plate before being sent to the atoms. Their polarizations can be independently set to any arbitrary ellipse. The power of the blue beam is set constant during the experiment, a pick-off on the red beam allows to calibrate very precisely the two-photon Rabi frequency. The blue path contains two couples of relay lenses which compensate for aberrations.

For the red laser, we measure the lightshift $\Delta\nu_r$ induced on the microwave transition $|5S_{1/2}, 1, -1\rangle \leftrightarrow |5S_{1/2}, 2, -2\rangle$ as a function of the optical power P_r . The lightshift evolves linearly with the optical power, so that

$$\Delta\nu_r = \alpha P_r = \frac{\Omega_r^2}{4\Delta} \Leftrightarrow \Omega_r = 2\sqrt{\alpha\Delta P_r} \quad (57)$$

where α is measured experimentally.

The Rabi frequency of the blue laser is directly measured on the Rydberg transition. We measure the depopulation of the ground state by spectroscopy. We then vary the optical power of the blue laser and measure the induced lightshift, $\Delta\nu_b$. Similarly than the previous calibration, we observe a linear evolution of the “blue” lightshift with the optical power, $\Delta\nu_b \propto P_b$.

Under typical conditions, $P_b = 100$ mW, leading to $\Omega_b/2\pi = 20$ MHz. P_r can be tuned from a few hundreds of pW to a few hundreds of μ W, leading to two-photon Rabi frequencies around 0.1 – 150 kHz.

2.3.5 DETECTION OF RYDBERG ATOMS

The experiment at JQI does not allow a direct measurement of the Rydberg population. However, it is possible to characterize it *post-mortem*. We perform spectroscopy via pumped atoms: after several cycles of excitation, we measure the populations in the various sublevels of the ground state manifold. Since most sublevels were initially not populated, the number of atoms in these states reflects the efficiency of the Rydberg excitation.

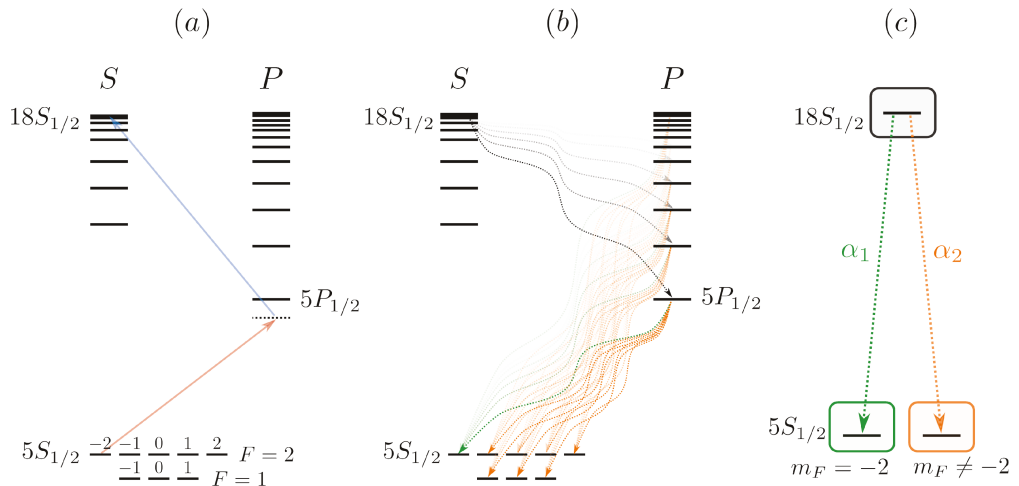


Figure 25 – **Desexcitation of the Rydberg states**

(a) We drive the transition $|5S_{1/2}, F=2, m_F=-2\rangle \rightarrow |18S_{1/2}, F=2, m_F=-2\rangle$ using a two-photon excitation. (b) There are multiple desexcitation paths from the $18S$ state. While some atoms decay back to the initial state (green paths), others end up in $m_F \neq -2$ sublevels of the ground state manifold (orange arrows). (c) We reduce the problem to a 3-level system: the $18S_{1/2}$ level (gray box), the initial state ($|5S_{1/2}, 2, -2\rangle$, green box) and all the other states of the ground state manifold gathered in one (orange box). Calculating the contribution of each path allows to extract the branching ratios between these states: 55% of the excited atoms decay back the initial state ($\alpha_1 = 0.55$), while the remaining end up in other sublevels of the ground state manifold ($\alpha_2 = 0.45$).

The populations are separated in time of flight with a Stern-Gerlach magnetic field gradient and measured via absorption imaging (see Fig. 26). The absorption beam being constituted of $\lambda = 780$ nm and $\lambda = 795$ nm light, populations in both manifolds can absorb the light. Some states

having the same magnetic properties, the populations are mixed as follows

$$\begin{aligned}
 N_{-2} &= N_{2,-2} \\
 N_{-1} &= N_{2,-1} + N_{1,1} \\
 N_0 &= N_{2,0} + N_{1,0} \\
 N_1 &= N_{2,1} + N_{1,-1} \\
 N_2 &= N_{2,2}
 \end{aligned}
 \tag{58}$$

With $N_{i,j}$ the atom number in the state $F = i, m_F = j$.

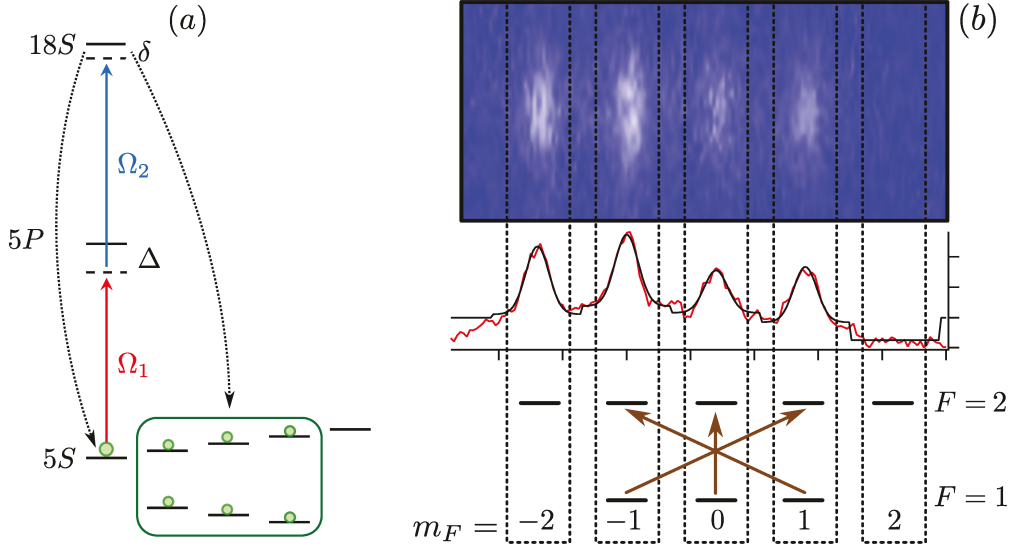


Figure 26 – **Detection via pumped atoms**

The populations of the ground state sublevels are separated in time of flight with a Stern-Gerlach magnetic field gradient. Since several sublevels have the same magnetic sensitivity, the 8 populations only lead to 5 distinct clouds of atoms. The brown arrows show the blending between the sublevels.

Only the populations in the N_{-1}, N_0 and N_1 are relevant for this measurement: N_{-2} contains atoms that have not been excited and N_2 is typically zero. We extract the fraction of Rydberg states by fitting the populations

$$\rho_R = \frac{N_{-1} + N_0 + N_1}{N}
 \tag{59}$$

where N is the total atom number.

To evaluate quantitatively the pumping rate, one must calculate the branching ratios between the different levels of the system. There exist a vast number of desexcitation paths (see Fig. 25b), but in our case, the problem can be reduced to a 3-level system (see Fig. 25c). The branching ratios between these states can be calculated by summing the contributions of

the most representative paths. This requires to know the rate of each transition (calculable with the [ARC Library](#)) and the repartition between the sublevels (calculable with the dipole matrix elements). Though we do not detail the calculation here, we have used $\alpha_1 = 0.55$ as the branching ratio from $18S_{1/2}$ to $|5S_{1/2}, 2, -2\rangle$ in the following. To get a quantitative value for the pumping rate, ρ_R must be rescaled by $1 - \alpha_1 = 0.45$.

2.3.6 TOWARDS EXPERIMENTATIONS

In this part, we have presented an apparatus allowing to produce an homogenous frozen gas of Rydberg atoms. Combining a Bose-Einstein condensate loaded into tridimensional optical lattices (see [Ch.1](#)) and Rydberg excitation (see [Ch.2](#)), this setup is an excellent platform to simulate large many-body quantum systems.

However, the short distance between neighboring lattice sites imposes to use relatively low Rydberg levels (see [Sec.2.2.3](#)). In our case, the lifetime of $18S$ atoms ($\tau_{18S} = 3.3 \mu\text{s}$) can be a limiting factor for some experiments. In particular, some proposals for quantum simulation with Rydberg states impose to measure the mechanical response of the sample, a measurement that typically requires $1 - 10$ ms.

In the next part (see [Part.ii](#)), we investigate a proposal aiming to increase the lifetime of low Rydberg states. We experimentally observe an unexpected onset of decoherence that complicates the implementation of the technique.

Part II

SPONTANEOUS DEPHASING IN LARGE
RYDBERG ENSEMBLES

ANOMALOUS BROADENING IN LARGE RYDBERG ENSEMBLES

When using Rydberg atoms in an optical lattice, the short intersite distance ($\sim 0.5 \mu\text{m}$) imposes to use relatively low Rydberg levels ($n=20$) to avoid Rydberg blockade, hence relatively short lifetimes ($\tau = 5 \mu\text{s}$). Unfortunately, a vast number of phenomena are related to the mechanical properties of the sample, which, given typical trapping frequencies in the kHz range, impose experimental timescales of several milliseconds.

Rydberg dressing is a proposal aiming to increase the lifetime of Rydberg atoms[23, 58, 87]. Coherently admixing a small fraction of Rydberg atoms with a much larger fraction of ground state atoms is predicted to result in a mixture combining long-range interactions and long lifetimes. This idea has triggered many theoretical and experimental proposals[4, 72, 73, 77, 87, 97, 107, 122], including methods to produce new states of matter such as supersolids[74], rotons[73] and solitons[110]. Rydberg dressing has been experimentally successful with a pair of atoms[86], but several experiments in large Rydberg ensembles have reported major deviations from the theory[1, 7, 46]. Deformations of the Rydberg spectra attributed to interaction-induced decoherence and anomalous depopulation of the ground state have notably been observed by the Houston team[1, 46].

In this chapter, we present our investigations of Rydberg dressing in an optical lattice. We interpret our observations in terms of an interaction-induced onset of decoherence due to resonant dipole-dipole interactions between Rydberg states of opposite parity. This type of many-body problem being extremely correlated, we circumvent the difficulty by using simple scalings based on mean-field assumptions.

This chapter begins with a brief overview of Rydberg dressing (see Sec.3.1). We then present experimental observations in the steady-state regime (see Sec.3.2), followed by steady-state scalings resulting from the hypothesis of an interaction-induced dephasing. We show that the dephasing is beyond pure Van der Waals interactions and involves resonant dipole-exchange scaling as C_3/R^3 (see Sec.3.4).

3.1 ELEMENTS OF THEORY: RYDBERG DRESSING

Many-body systems with long-range interactions are the cornerstone of many proposals concerning Hamiltonian engineering[87]. Complex states of matter, such as dipolar crystals[33], supersolids[21, 61], checkerboard phases[92], rotons[73] and solitons[110] could be produced in many-body systems with strong dipole-dipole interactions. These phases usually assume particles with typical electric dipole moments of 2 to $5ea_0$, which have notably been achieved with polar molecules prepared in their rovibrational ground state[35, 122].

There is a strong interest in producing such large dipole moments in quantum gases experiments using alkali atoms. Rydberg excitation has been identified as a potential solution, because the dipole moment of Rydberg states increases rapidly with their principal quantum number ($\propto n^4 ea_0$) and can become extremely large. However, the short lifetime of Rydberg states has been a limiting factor so far. Most experiments involve the mechanical properties of the BEC, which, given the typical trapping frequencies of the lattice traps (~ 1 kHz) require 1 – 10 ms of experimental time. Rydberg lifetimes (1 – 100 μ s) are typically 3 orders of magnitude lower than these requirements.

Rydberg dressing is a proposal aiming to tackle this issue. It consists in coherently admixing a small fraction of Rydberg states with a much larger fraction of ground state atoms, resulting in mixture that combines the advantages of each states. With a small fraction of Rydberg atoms (*e.g.* 1%), the mixed state would combine a long lifetime (~ 10 ms) and a sufficiently large dipole moment for the proposed applications. The lifetime and interaction range of the would be both adjustable by the choice of the Rydberg level n and by the fraction of Rydberg atoms in the system. First proposed in 2002[23], Rydberg dressing triggered a vast interest in the community.

3.1.1 A NAIVE APPROACH TO RYDBERG DRESSING

A usual description of Rydberg dressing consists in assuming a pair of two-level atoms with ground state $|g\rangle$ and Rydberg state $|r\rangle$ [87, 106]. The mixed-state results from the coherent admixture of both states and writes

$$|\psi\rangle = \alpha|g\rangle + \beta|r\rangle \quad (60)$$

Assuming a detuning δ and a Rabi frequency Ω , the fraction β can be defined in first approximation as

$$\beta = \frac{\Omega}{2\delta} \quad (61)$$

Rydberg states can be pumped with an off-resonant continuous wave. In the hypothesis of a two-photon scheme (see Ch.2), the intermediate detuning Δ must be large with respect to the Rabi frequency, $\Delta \gg \Omega_1, \Omega_2, \Gamma$ in order to ensure coherent coupling between $|g\rangle$ and $|r\rangle$.

Introducing the dipole operator for spontaneous decay of the Rydberg state \hat{d} , the mixture would have a decay rate[87]

$$\gamma \propto |\langle g|\hat{d}|\psi\rangle|^2 \propto \beta^2 \gamma_r \quad (62)$$

where γ_r is the natural decay rate of the Rydberg state. Since β can be set very small, $|\psi\rangle$ has potentially a much longer lifetime than $|r\rangle$.

The dipole-dipole interaction between two dressed states could be calculated as follows

$$\varepsilon_{\text{int}} = \langle \psi|U_{\text{dd}}|\psi\rangle = \beta^2 \langle r|U_{\text{dd}}|r\rangle = \beta^2 \varepsilon_r \quad (63)$$

where U_{dd} the usual dipole operator and ε_r the full interaction energy between two Rydberg states. ε_r strongly depends on the Rydberg level n and the distance between the atoms. In fact, the phenomenon of Rydberg blockade (see Ch.2), not considered in this equation, leads to interaction energies much lower than the one presented in Eq.(63).

3.1.2 RYDBERG DRESSING IN A PAIR OF ATOMS

A correct estimation of the interaction energy can be done by calculating the dressed state for two atoms simultaneously[87]. The interaction Hamiltonian could be described as a 4×4 matrix in the basis ($|gg\rangle, |gr\rangle, |rg\rangle, |rr\rangle$), but the antisymmetric state is uncoupled. The problem can therefore be reduced to a 3×3 matrix in the dressed-state basis ($|gg\rangle, 1/\sqrt{2}(|rg\rangle + |gr\rangle), |rr\rangle$), and we get

$$\hat{\mathcal{H}} = \hbar \begin{pmatrix} 0 & \Omega/\sqrt{2} & 0 \\ \Omega/\sqrt{2} & \delta & \Omega/\sqrt{2} \\ 0 & \Omega/\sqrt{2} & 2\delta + U_{\text{vdw}} \end{pmatrix} \quad (64)$$

Considering that the interaction at stake is the dipole-dipole interaction, we can take $U_{\text{vdw}} = C_6/R^6$, with R the interatomic distance. The interaction leads to very different behaviors depending on the sign of C_6 (see Fig.27). A negative C_6 triggers an avoided crossing when the laser is 2-photon resonant with the dipole-shifted $|rr\rangle$ state, $2\delta = C_6/R^6$. Analyzing the energy of the eigenstate connecting with the ground state (which is the state of interest in the context of Rydberg dressing), we note that the energy slowly varies with R inside the avoided crossing but rapidly falls off at larger distances. Conversely, when $C_6 > 0$, there is no avoided crossing but the eigenenergy is also R -independent at short distances ($R \lesssim 0.5 \mu\text{m}$ for $n = 40$ and $C_6/2\pi = 0.9 \text{ GHz } \mu\text{m}^6$). This independence is the direct

consequence of the Rydberg blockade: in the blocked regime, the coupling to the $|rr\rangle$ state become off-resonant and significantly diminishes the fraction of $|rr\rangle$ states in the mixture.

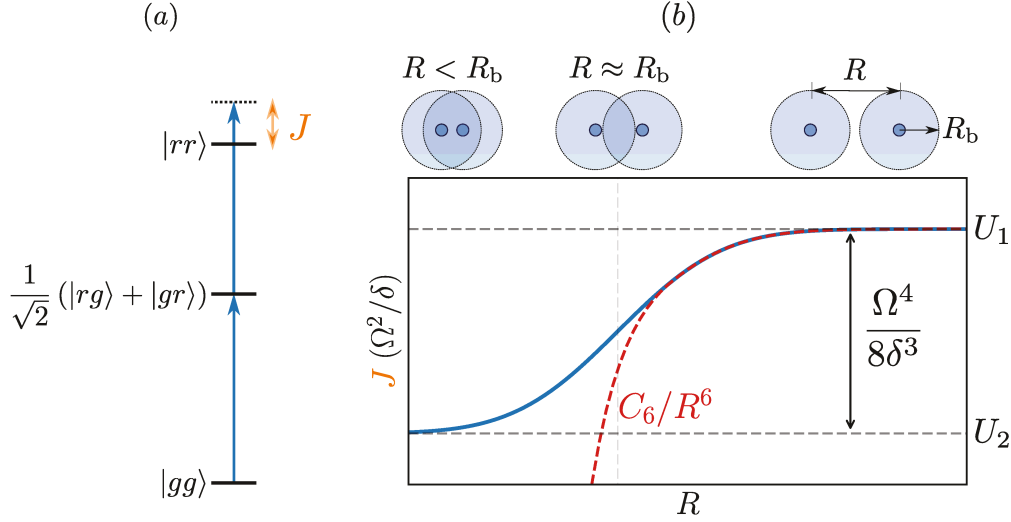


Figure 27 – **Binary Rydberg dressing potential**

(a) Energy diagram of the Rydberg-dressed two-atom system. The interaction potential J shifts the energy of the $|rr\rangle$ level. (b) Schematic representation of the Rydberg-dressed ground-state interaction potential as a function of the interatomic distance. The interaction potential (blue curve) deviates from the usual van der Waals potential (dotted red curve) at short distances due to Rydberg blockade (see cartoons above). The resulting soft-core potential is a signature of Rydberg dressing and has been observed by the team of G.W. Biedermann[86].

Due to the Rydberg blockade, the composition of the mixed state depends on the interatomic distance, a behavior that is not captured by Eq.(61). To calculate β , a possible method consists in extracting the eigenstates of the system: the eigenvector with the lowest energy corresponds to a state predominantly populated by ground state atoms mixed with a small fraction of two-excited states and is therefore the state of interest for Rydberg dressing. Using this state, the fraction of Rydberg atoms becomes[87]

$$\beta = |2\langle rr|\psi\rangle|^2 + \frac{1}{2}|\langle gr|\psi\rangle + \langle rg|\psi\rangle|^2 \quad (65)$$

From there, it is possible to calculate the asymptotic behaviors of the ground state energy in the two limits $U_{dd} \gg \delta$ and $U_{dd} \ll \delta$ [87].

In the limit of small R , the dipole energy is much larger than the laser detuning, $U_{\text{dd}} \gg \delta$. Atoms are fully blockaded and the state $|rr\rangle$ cannot be excited. The energy of the ground state reduces to

$$U_2 = \frac{\hbar\delta}{2} \left(1 - \sqrt{\frac{2\Omega^2}{\delta^2} + 1} \right) \quad (66)$$

To evaluate the interaction energy, we take the difference between this energy and the ground state energy without interactions, and get

$$\frac{E_{\text{int}}}{\hbar} \underset{U_{\text{dd}} \gg \delta}{\sim} \frac{1}{8} \frac{\Omega^4}{\delta^3} \quad (67)$$

In the case of large distances, the energy shift due to the interactions becomes negligible compared to the detuning, $U_{\text{dd}} \ll \delta$. The system is not blockaded, and the previous expression of the Rydberg fraction applies, $\beta \sim \Omega/2\delta$. The doubly-excited state has a fraction β^2 and the interaction between two doubly-excited states is expected to evolve as $\langle rr|U_{\text{dd}}|rr\rangle \sim \beta^4$. The ground state energy value dependent on R scales as

$$\frac{E_{\text{int}}}{\hbar} \underset{U_{\text{dd}} \ll \delta}{\sim} \frac{1}{16} \frac{\Omega^4}{\delta^4} U_{\text{vdw}} \sim \frac{1}{16} \frac{\Omega^4}{\delta^4} \frac{C_6}{R^6} \quad (68)$$

Taking in account the energy of the ground state without interactions, the total energy at large distances has the asymptotic value

$$U_1 = \hbar\delta \left(1 - \sqrt{\frac{\Omega^2}{\delta^2} + 1} \right) \quad (69)$$

3.1.3 EXPERIMENTAL IMPLICATIONS

The previous results can be interpreted in terms of experimental requirements and perspectives. From a low Rydberg state, *e.g.* $n = 20$, $\tau_{20} = 5 \mu\text{s}$, reaching a mixture lifetime of $\tau_{\text{m}} \geq 1 \text{ ms}$ imposes $\beta \leq 0.07$.

For the dressing to be visible, the interaction energy must be of the same order of magnitude than other energies in the system. In the case of a BEC in an optical lattice, the onsite energy (see Ch.1) is typically in the range $U \sim 1 - 10 \text{ kHz}$. Given Eq.(67), $\Omega/2\pi = 10 \text{ MHz}$ and $\delta/2\pi = 100 \text{ MHz}$ would match the requirements while maintaining an acceptable value of β .

In the particular case of a BEC trapped in optical lattices, the avoided crossing should impact the correlation function of the sample and potentially lead to new phases of matter. The apparition of 4 phases of matter has been predicted: superfluid, mesoscopic supersolid, ring-shaped crystal and classical crystalline[122]. These predictions have been done in a 2d optical lattice with Rydberg state $n = 20$, conditions that are very close

to those available in our experiment.

The intersite distance matches the blockade radius on the JQI experiment (see Ch.2). This setup is a good opportunity to characterize the region around the avoided crossing, and possibly find a way towards the production of a supersolid. However, only a limited fraction of the parameter space can be explored: $\Omega/2\pi$ can range from 0 to 150 kHz at best.

As a starting point, we characterize the Rydberg states produced on the experiment. As we will show in the next part, strong dephasing perturbs the system and strongly modifies its physics (see Sec.3.2.3.1). These effects are believed to have negative implications on Rydberg dressing.

3.2 RYDBERG DRESSING IN LARGE ENSEMBLES

The first series of Rydberg dressing experiment follows the excitation and detection schemes presented in Ch.2. We excite the $|5S_{1/2}, F = 2, m_F = -2\rangle \rightarrow |18S_{1/2}, F = 2, m_F = -2\rangle$ transition via an off-resonant two-photon excitation with intermediate detuning $\Delta/2\pi = 235$ MHz. The detection is performed via pumped atoms which are separated in time of flight with a Stern-Gerlach magnetic field gradient. All experiments (unless mentioned otherwise) are performed in the tridimensional cubic lattice (see Ch.1) with intersite distance $\lambda/2 = 406$ nm.

3.2.1 EXPERIMENTAL PARAMETERS

The experiment has three main experimental parameters: the two-photon Rabi frequency Ω , the two-photon detuning δ (see Ch.2) and the density of atoms in the ground state available for Rydberg excitation ρ_0 . As mentioned in the previous chapter, the Rabi frequency is directly related to the optical power in each beam. In practice, we keep the blue laser at $P_b = 100$ mW and set Ω manually with P_r . The two-photon detuning δ is controlled by an AOM.

We control the atomic density available for Rydberg excitation by microwave transfer between the sublevels of the ground state manifold. The BEC is produced in the $|5S_{1/2}, F = 1, m_F = -1\rangle$ level while the Rydberg transition starts in the $|5S_{1/2}, F = 2, m_F = -2\rangle$: a tunable rapid adiabatic passage[109] between the two states allows to load an arbitrary atomic fraction $0 \leq f \leq 1$ into the $|5S_{1/2}, F = 2, m_F = -2\rangle$ state.

Due to the Rydberg detection scheme (See Ch.2), atoms remaining in the $|5S_{1/2}, F = 1, m_F = -1\rangle$ level must be transferred into another, “non-participating” sublevel. We shelve this population into the $|5S_{1/2}, 2, 2\rangle$ state with three consecutive microwave rapid adiabatic passages. Atoms excited to the Rydberg state tend to decay back to the sublevels $m_F \leq 1$: the $|5S_{1/2}, F = 2, m_F = 2\rangle$ sublevel does not participate to the detection and can be used as a reservoir for the $1 - f$ fraction.

3.2.2 EXPERIMENTAL OBSERVABLES

3.2.2.1 RESONANT PUMPING RATE R_0

We measure the resonant pumping rate R_0 by measuring the depopulation of the initial state as a function of the excitation time τ_k . The red laser, however, also weakly drives the D_1 line. An accurate measurement of R_0 must take in account the depopulation due to this transition. We

measure the depopulation of the ground state with and without the blue laser (see Fig.28), leading to

$$\begin{aligned}\rho_0^{(r+b)}(t) &= \alpha \exp(-R^{(r+b)}t) \\ \rho_0^{(r)}(t) &= \beta \exp(-R^{(r)}t)\end{aligned}\quad (70)$$

R_0 can be extracted from $R^{(r+b)}$ and $R^{(r)}$. Since the experiment is run in the steady-state regime, the technique used to measure the population cannot be applied to the initial state of the excitation. Knowing that 55% of the atoms decay back to this state, we can extract the resonant pumping rate from all other states using a 45% scaling.

$$R_0 = \frac{R^{(r+b)} - R^{(r)}}{0.45}\quad (71)$$

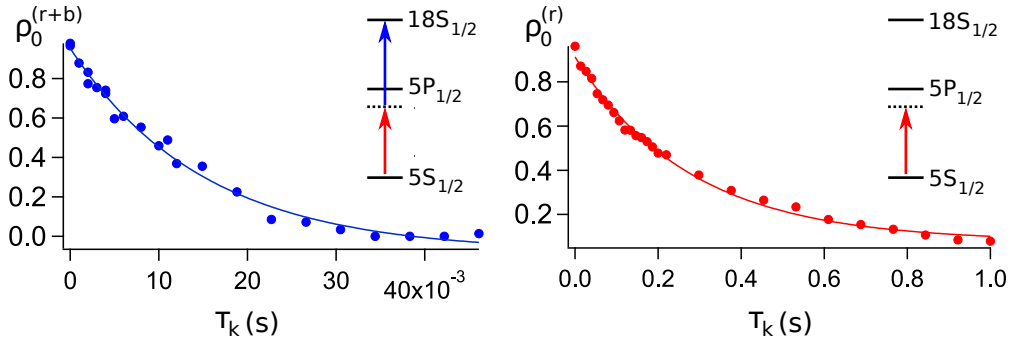


Figure 28 – **An example of resonant pumping rate measurement**

We measure $R^{(r+b)}$ (*left*) and $R^{(r)}$ (*right*) independently. Note the different timescale in the axis. This measurement was performed with $\Omega/2\pi = 13\text{kHz}$.

The depopulation due to the $5S - 5P$ transition only is relatively small, we typically observe two orders of magnitude of difference between $R^{(r+b)}$ and $R^{(r)}$. In the range $\Omega/2\pi = [0.1, 150]\text{kHz}$, the typical values of the resonant pumping rate are in the range $R_0 = [0.1, 15]\text{ms}^{-1}$.

3.2.2.2 WIDTH OF RYDBERG SPECTRA Γ

We extract the transition width from spectroscopy via pumped atoms (see Fig.29). We excite the Rydberg transition during a fixed excitation time $\tau_k \geq 3 \times 2\pi/\Gamma_0$, sufficiently long to build up the population in the ground state sublevels but short enough to avoid fully depopulating the ground state. Using the detection technique presented in Ch.2, we scan the two-photon detuning δ and observe the spectrum of the transition. The spectra are symmetrical, we extract the full width at half-maximum Γ from a Lorentzian fit,

$$R = \frac{R_0}{1 + 4\delta^2/\Gamma^2}\quad (72)$$

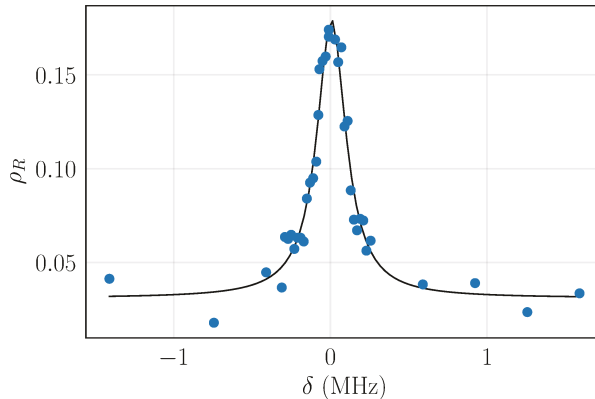


Figure 29 – **An example of Rydberg spectrum**

Measurement performed with $\Omega/2\pi = 3\text{ kHz}$ and $\rho_0 = 57\ \mu\text{m}^{-3}$ (*i.e.* $f = 1$), leading to $\Gamma = 5\Gamma_0$.

3.2.3 INITIAL OBSERVATIONS

While Rydberg dressing has been an experimental success with a pair of atoms[86], experiments with large Rydberg ensembles started to raise concerns as early as 2010. Increasing the number of particles completely modifies the nature of the phenomenon: the physics of the problem can become very challenging to capture theoretically, particularly in the presence of dissipation and strong correlations[46]. In the following years, theoretical efforts using low-intensity expansions[133], Monte-Carlo simulations[6] and density-matrix cluster expansions[128] made progress in understanding several regimes of the problem. However, the promise of large scale Rydberg dressing started to fade away as suspicion of excessive decoherence emerged[1]. Shortly after we published our first article on the topic[60], a clear signature of level shifting and interaction-induced decoherence was also observed in the Houston experiment[46].

In our first publication, we systematically measured the evolution of Γ and R_0 as a function of δ and Ω , in the steady-state regime. This first serie of experiments help ruling away the most obvious sources of broadening. Additional measurements, notably using the superlattice feature, helped estimating the range of the phenomenon. We finally identified a mechanism compatible with these observations.

3.2.3.1 GIANT BROADENING

We observe a giant broadening when increasing Ω (see Fig.30). The spectra maintain their lorentzian shape but exhibit extremely large width, up to $\Gamma/2\pi = 9\text{ MHz}$ (obtained for $\Omega/2\pi = 150\text{ kHz}$, $\rho_0 = 57\ \mu\text{m}^{-3}$), corresponding to $\Gamma = 200\Gamma_0$.

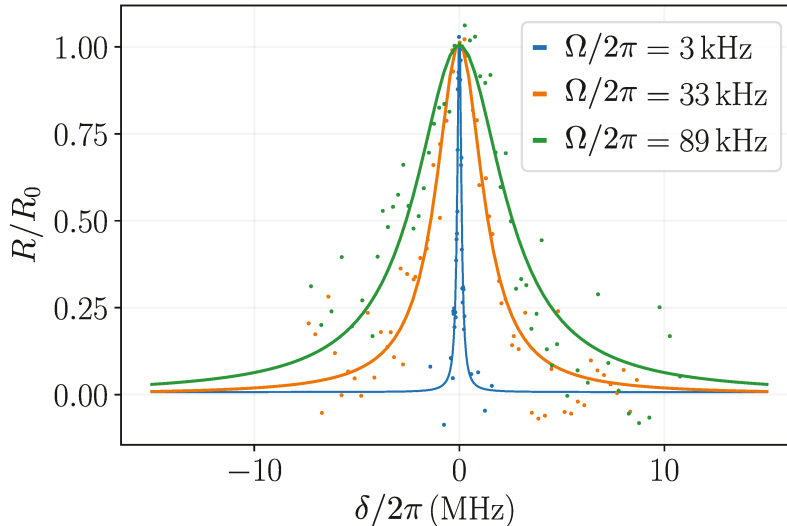


Figure 30 – **Giant broadening of the Rydberg transition**

When increasing Ω , we observe a considerable broadening leading to widths up to $200\Gamma_0$. Here we have normalized each measurement by $R_0(\Omega)$ for the sake of clarity. These data were taken with $\rho_0 = 57 \mu\text{m}^{-3}$.

3.2.3.2 EVOLUTION OF R_0 WITH Ω

Over $\Omega = 0 - 175$ kHz, R_0 strongly deviates from the single-particle theory. We observe a quadratic turn-on ($\Omega \lesssim 70$ kHz) followed by a linear behavior at higher driving frequencies (see Fig.31). The resonant pumping rate is much lower than expected and does not exhibit a saturation at high Ω , as would be expected in the standard single-atom theory and purely homogeneous broadening. This results are incompatible with a superatom behavior or pure homogeneous dephasing and rather point towards a more complex mechanism involving interactions.

We compare experimental results to the single-atom resonant pumping rate[51]

$$R_{0,\text{single}} = \frac{\Gamma_0 \Omega^2}{2\Omega^2 + \Gamma_0^2} \quad (73)$$

Remarkably, R_0 is compatible with single-atom theory when we take Γ as the measured transition linewidth.

$$R_0 = \frac{\Omega^2}{\Gamma} \quad (74)$$

3.2.3.3 EVOLUTION OF Γ WITH Ω

Over the same range of Rabi frequencies, we observe a linear evolution of the measured width. The minimum measured linewidth is about $3 \times \Gamma_0$:

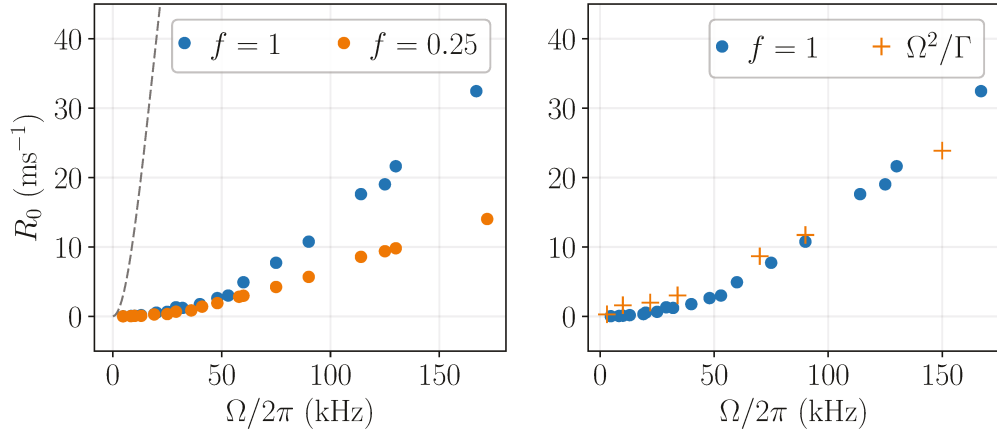


Figure 31 – **Evolution of the resonant pumping rate as a function of the driving strength**

(left) The measured resonant pumping rate strongly deviates from single-atom theory (grey dashed line). (right) R_0 is compatible with single-atom theory assuming $R_0 = \Omega^2/\Gamma$.

we attribute this limitation to experimental imperfections, such as inhomogeneities in the optical lattice and noise in the laser stabilization systems.

We compare the measured width to the hypothesis of pure power broadening (see Fig.32). In the case of pure power broadening, Γ would evolve as[51]

$$\Gamma_{\text{PB}} = \Gamma_0 \left(1 + 2 \frac{\Omega^2}{\Gamma_0^2} \right)^{1/2} \quad (75)$$

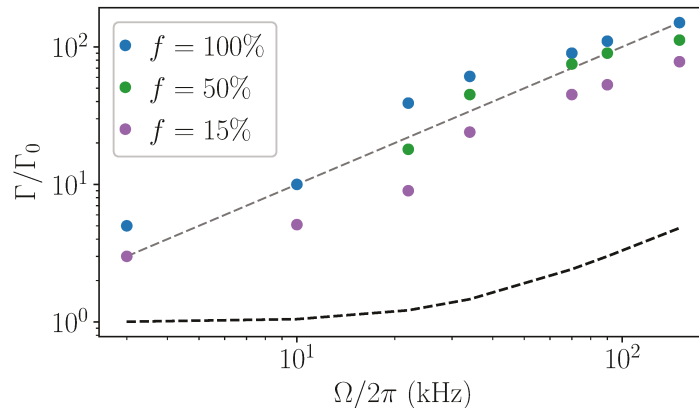


Figure 32 – **Evolution of the measured width**

Γ is linear width Ω . The dashed grey line is linear scaling. The dashed black line corresponds to the power broadening.

We note that Γ is linear with Ω , and power broadening predicts widths much lower than our observations.

3.3 SHORTLISTING THE BROADENING CAUSES

In this section, we detail the approach we followed to determine the mechanism underlying the anomalous broadening[60]. Conventional sources of broadening such as power broadening and pure dephasing were inconsistent with our observations, and previous publications suggested an interaction-induced mechanism[7]. We performed additional measurements to get specific insights into the phenomenon; these informations helped shortlisting two possible mechanisms, both involving interactions. Steady-state scalings finally led to a satisfactory explanation of the broadening.

3.3.1 MICROSCOPIC ARRANGEMENT

The effect of the microscopic arrangement on the broadening can provide a hint concerning the range of the phenomenon: a short-range effect would strongly depend on the geometry, while a long-range mechanism would only depend on the atomic density.

The superlattice (see Ch.1) allows to perform two specific tests: modify the intersite distance and control the lattice filling. Under usual conditions, loading a $N = 4 \times 10^4$ BEC into this optical lattice leads to overfilling, *i.e.* the number of atoms per site is larger than one and follows a Poissonian distribution. The corresponding density can be measured via site-dependent spectroscopy[34] and leads to $\rho_0 = 57 \mu\text{m}^{-3}$ in the usual $\lambda/2$ configuration.

A specific procedure (involving extremely narrow addressing pulses in pairs of unbalanced lattice sites) allows to empty every other site. This results in a checkerboard configuration with nearest neighbor distance $\sqrt{2}\lambda/2 = 574 \text{ nm}$ and density $\rho_0 = 20 \mu\text{m}^{-3}$.

A careful matching of the density of atoms allows to load a Mott insulator in both configurations: the resulting densities are $\rho_0 = 15 \mu\text{m}^{-3}$ in the $\lambda/2$ configuration and $\rho_0 = 7 \mu\text{m}^{-3}$ in the λ configuration.

We test all 4 configurations for two values of Ω , all other parameters unchanged (see Fig.33). As described in Sec.3.4.2, a long-range mechanism involving resonant dipole-dipole interactions C_3/R^3 is compatible with a relation of type $\Gamma \propto R_0 \rho_g v$, where v is a volumic term. This, combined with the observation $R_0 \approx \Omega^2/\Gamma$, leads to $\Gamma \sqrt{\rho_g v} \propto \Omega$. Once adjusted for their respective densities, all configurations lead to the similar width Γ , which is a strong indication towards a long-range mechanism based on resonant dipole-dipole interactions.

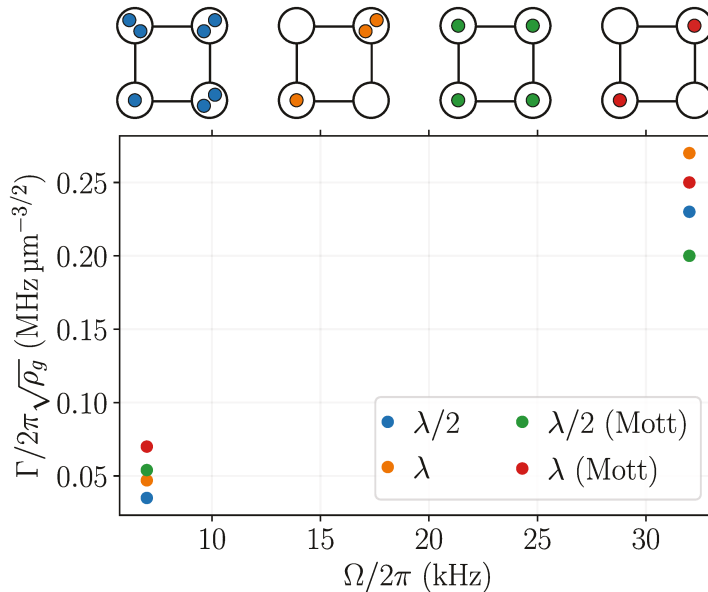


Figure 33 – **Correlation between the measured width and the microscopic arrangement**

Once adjusted for the density, the various microscopic arrangements and densities (see above cartoon) lead to similar widths. This points towards a long-range phenomenon depending only on ρ_g .

3.3.2 LIFETIME MEASUREMENT

The lifetime of an energy level is directly linked with its natural linewidth. In order to observe whether the broadening corresponds to a reduction of lifetime, we measure the lifetime of the $18S$ atoms by fluorescence. In case of reduction of the lifetime, the measurement would point towards a collective and cooperative effect such as superradiance[144].

We use a photon counting device (Laser Components Count 100-C-FC) to measure the fluorescence on the D_2 line. The number of collected photons is proportional to the number of $18S$ atoms in the system and scales with the optical pumping signal (see Fig.34). The photons of interest being at 780 nm, we use a dichroic filter placed in front of the detector to filter the excitation light at 795 nm.

We note that this measurement only provides a rough estimate of the lifetime because it does not take in account the many decay channels discussed earlier in this thesis (see Ch.2).

The measured lifetime is compatible with the natural lifetime $\tau_0 = 3.27 \mu\text{s}$ of the $18S$ level at $T = 300 \text{ K}$. This test has notably been performed with $\Omega/2\pi = 140 \text{ kHz}$, leading to $\Gamma = 200\Gamma_0$. This constatation

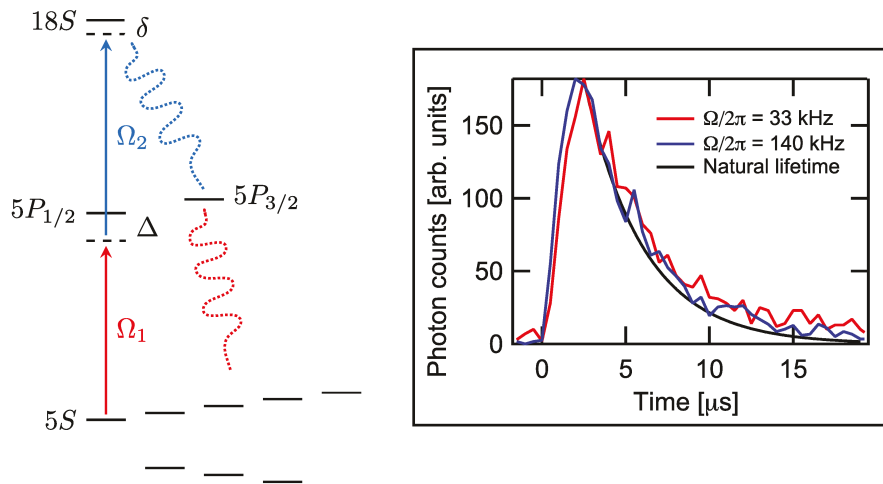


Figure 34 – **Time-resolved photon detection**

(*left*) we use a rapid amplified photodetector to measure the photons emitted by fluorescence from the D_2 line. (*right*) Our measurements are compatible with the natural lifetime of 18S.

rules out a mechanism involving superradiance.

3.4 STEADY-STATE SCALINGS

In this section, we identify the underlying cause of the broadening. We first gather our observations to shortlist the potential sources of broadening.

- The observed spectra are symmetrical, well characterized by Lorentzian distributions and with widths up to 8 MHz: this is incompatible with power-broadening or pure dephasing.
- The lifetime of the Rydberg state is unchanged: this does not match with superradiance.
- We observe $R_0 \propto \rho_g^{-1/2}$. At first sight, a modification of the resonant pumping rate could arise from a “superatom” behavior, where $N_s > 1$ atoms share a single Rydberg excitation due to Rydberg blockade. The resulting collective state has specific properties, such as a collective Rabi frequency $\Omega_s = \sqrt{N_s}\Omega$ [105]. However, if the broadening was caused by a superatom, the previous equation combined with the observation $R_0 \approx \Omega_s^2/\Gamma$ would lead to the scaling $R_0 \approx \rho_g \Omega/\Gamma$. This last equation does not match the observations and therefore rules out a superatom behavior.

At the same time, we observe that both Γ and R_0 evolve linearly with Ω , and Γ scales linearly with the *Rydberg* population. These are strong indications towards a mechanism involving interactions between Rydberg states. The effect is independent from the microscopic arrangement, which supports the hypothesis of a long-range interaction, such as the dipole-dipole interaction.

Modeling the effect of interactions in a large system is difficult: the complexity of the problem grows exponentially with the number of particles, leading to an extremely large parameter space in our case. Instead of developing a full model, we propose simple heuristic scalings based on our observations. These scalings are mean-field and do not take in account correlations in the system. We adapt our scalings to two types of interactions, Van der Waals (see Sec.3.4.1) and dipole-dipole (see Sec.3.4.2), and show that one captures the phenomenon much better than the other.

3.4.1 VAN DER WAALS SCALING

We first consider the case of Van der Waals interactions between the Rydberg states in the system. The knowledge of the lifetime of the $18S$ level allows to estimate the density of $18s$ atoms in the steady-state regime.

$$\rho_{18S} = \rho_g \frac{R_0}{\Gamma_0} \tag{76}$$

Assuming that the broadening is only due to van der Waals interactions between $18S$ atoms, we can build a scaling of the form

$$\Gamma = \Gamma_0 + C_6 \rho_{18S}^2 \quad (77)$$

In absence of Rydberg states, the transition width is unaltered ($\Gamma = \Gamma_0$). In presence of Rydberg states, the width of the transition increases with the square of the density weighted by the van der Waals coefficient C_6 . We use the square of the density for homogeneity purposes. This equation allows to compare the measured width with the hypothesis of a broadening mediated by van der Waals interactions (see Fig.35).

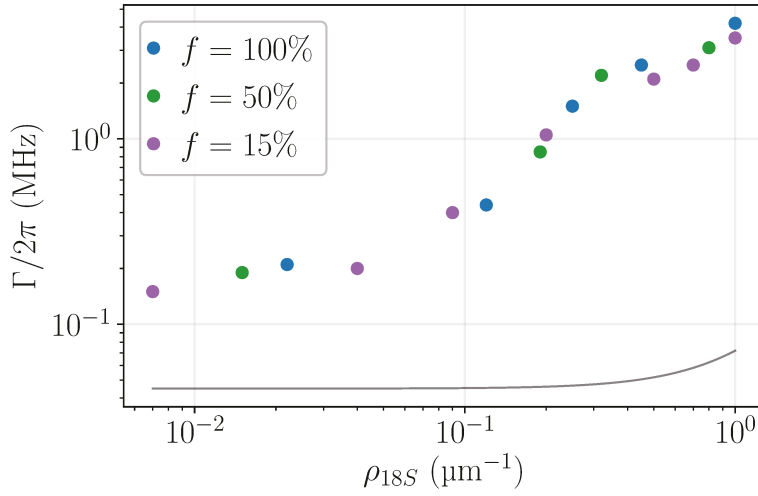


Figure 35 – **Evolution of Γ with ρ_{18S}**

The gray line corresponds to the Van der Waals scaling. There is a clear mismatch between experimental data and the scaling.

With this, we can introduce an interaction volume $\beta_6 = \sqrt{C_6/\Gamma_0}$, which leads to

$$\Gamma = \beta_6^2 \Gamma_0 \rho_{18S}^2 = \beta_6^2 \rho_g^2 \frac{R_0^2}{\Gamma_0} \quad (78)$$

where we have included Eq.(76).

Combining Eq.(78) and the observation $R_0 = \Omega^2/\Gamma$, we find

$$\Gamma = \left(\Omega^4/\Gamma_0\right)^{1/3} (\rho_g \beta_6)^{2/3} \quad (79a)$$

$$R_0 = \left(\Omega^2 \Gamma_0\right)^{1/3} (\rho_g \beta_6)^{-2/3} \quad (79b)$$

The Van der Waals scaling underestimates the width and the resonant pumping rate by almost an order of magnitude (see Fig.36). We reject this hypothesis and focus on the dipole-dipole interaction instead.

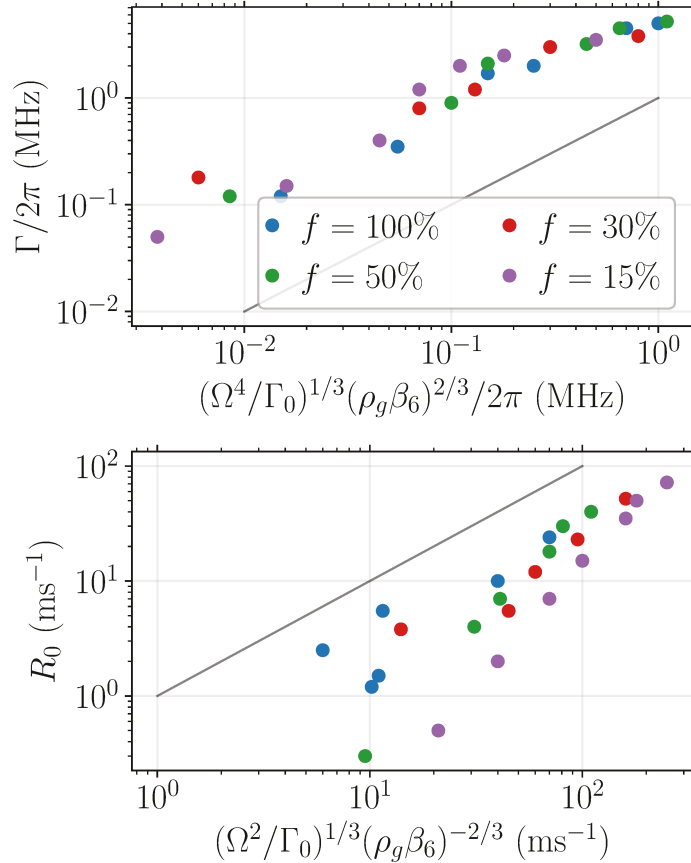


Figure 36 – Van der Waals scalings

The solid black line is unit linear scaling with unit slope. The Van der Waals scaling fails to capture the phenomenon.

3.4.2 DIPOLE-DIPOLE SCALING

As detailed in ch. 2, new Rydberg levels can spontaneously appear in a sample due to blackbody transfers. In the case of $18S$, the levels likely to appear include $17P$ and $18P$, and can interact with the $18S$ level via resonant dipole-dipole interaction, C_3/R^3 . This type of interaction being of much larger range than the Van der Waals interaction, the broadening might arise from it.

The density of each i^{th} nP state, $\rho_{nP}^{(i)}$, depends on its branching ratio $b_{nP}^{(i)}$ and natural linewidth $\Gamma_{nP}^{(i)}$. The density writes

$$\rho_{nP}^{(i)} = \rho_{18S} b_{nP}^{(i)} \frac{\Gamma_0}{\Gamma_{nP}^{(i)}} = \rho_g R_0 \frac{b_{nP}^{(i)}}{\Gamma_{nP}^{(i)}} \quad (80)$$

Assuming a broadening based on the dipole-dipole interaction, the measured width is expected to be of order of

$$\Gamma = \Gamma_0 + \sum_i |C_{3,nP}^{(i)}| \rho_{nP}^{(i)} \quad (81)$$

We use this first prediction to compare experimental data with the scaling (see Fig.37).

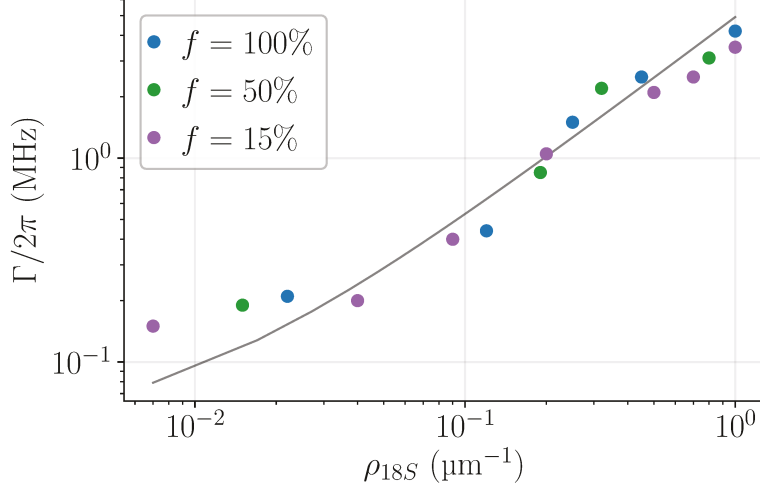


Figure 37 – **Evolution of Γ with ρ_{18S}** : the solid black line corresponds to the dipole-dipole scaling. The dipole-dipole scaling seems to capture much better the phenomenon than the Van der Waals scaling (light gray line).

Using Eq.(80) the previous result can be expressed in terms of an interaction volume β_3 , which writes

$$\beta_3 \approx \sum_i |C_{3, nP}^{(i)}| b_{nP}^{(i)} / \Gamma_{nP}^{(i)} \quad (82)$$

with the values presented in Ch.2, we find $\beta_3 = 108 \mu\text{m}^3$.

With this, we can rewrite the expression of Γ ,

$$\Gamma = \Gamma_0 + \beta_3 \rho_g R_0 \quad (83)$$

Assuming $\Gamma_0 \ll \Gamma$ (valid assumption in steady-state) and using the observation $R_0 \approx \Omega^2 / \Gamma$, we can express the observables (Γ, R_0) as a function of the parameters (ρ_g, Ω),

$$\Gamma = \Omega \sqrt{\rho_g \beta_3} \quad (84a)$$

$$R_0 = \frac{\Omega}{\sqrt{\rho_g \beta_3}} \quad (84b)$$

Similarly than before, we compare our experimental observations with these scaling laws (see Fig.38).

Our observations point towards a decoherence mechanism involving dipole-dipole interactions: as soon as the first Rydberg states are produced, blackbody transfers lead to the apparition of Rydberg states of

opposite parity. These states interact with each other, leading to a position and orientation-dependent level shifting of all Rydberg states. This level shuffling leads to a global dephasing in the sample, thus reducing the effective laser detuning and facilitating the production of additional Rydberg states. As the population of Rydberg states increases, the dephasing accelerates: we conclude to a mechanism of rapid avalanche dephasing.

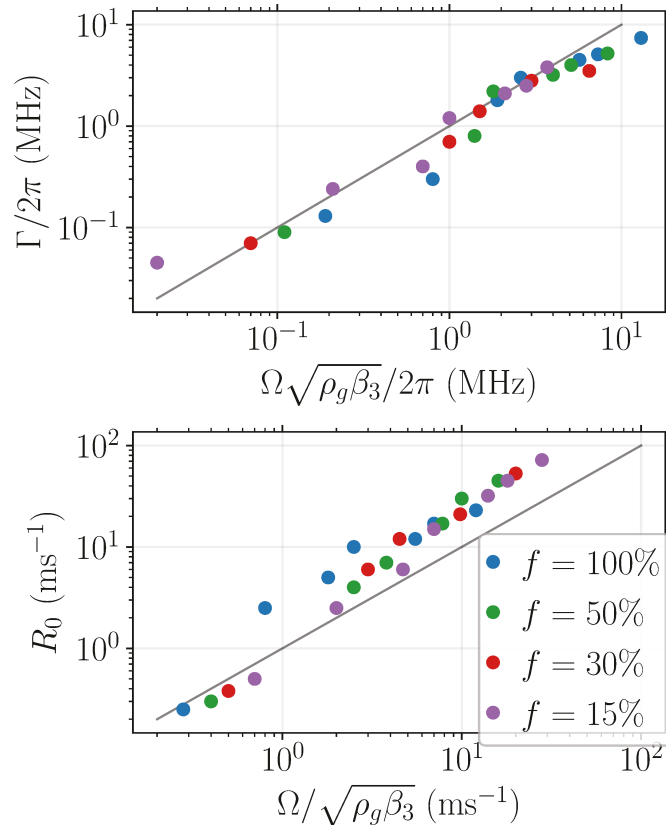


Figure 38 – **Dipole-dipole scalings**

The solid black line is unit linear scaling with unit slope. The dipole-dipole scaling fits well the phenomenon.

As a matter of fact, spontaneous emission and absorption of thermal fields have been seen as limiting factors for Rydberg experiments since their introduction in laboratories[38, 137]. These limitations had also been pointed out in the seminal paper on Rydberg dressing[23]. However, initial theoretical works did not consider the resulting interactions between Rydberg states of opposite parity, and neither the subsequent dephasing of the sample.

Despite their simplicity, the steady-state scalings presented in this chapter seem to capture reasonably well our observations. Since other experiments have led to similar conclusions[1, 46], we have a relatively strong confidence in the mechanism presented here. Nevertheless, parts of the

phenomenon — notably the dynamics — are still unexplored. We present further investigations in the next chapter.

INVESTIGATIONS OF THE DYNAMICS OF THE RYDBERG POPULATIONS

The previous chapter was dedicated to the steady-state analysis of a decoherence mechanism affecting large Rydberg ensembles (see Ch.3). We have postulated the spontaneous apparition of a new population of Rydberg atoms (the $n'P$ states) that trigger a rapid dephasing of the sample (see Fig.39). While the exact phenomenon involves strong correlations and is difficult to calculate, our mean-field steady-state scalings match the data relatively well.

In this chapter, we study the time evolution of the decoherence. We confirm the mechanism by investigating the dynamics of the two types of Rydberg populations in the system, namely the nS and the $n'P$ states (see Sec.4.1 and Sec.4.2). We show that whereas one population is directly accessible via fluorescence measurements, the other one requires the use of an indirect method. Our observations are completed by two models based on non-linear rate equations and mean-field assumptions. We note that the typical timescale of the problem is determined by the apparition of the first pollutant state. We show that the duration of the drive plays a key role in the dynamics and that the broadening can be slightly reduced by a careful choice of excitation time (See Sec.4.1.3).

We finally propose several techniques to mitigate the decoherence (See Sec.4.4). While none of them completely solves the problem, we note that microwave cavities can be remarkably efficient in the case of circular Rydberg states. We also identify cryogenic environments as a potential solution for Rydberg dressing in small many-body systems.

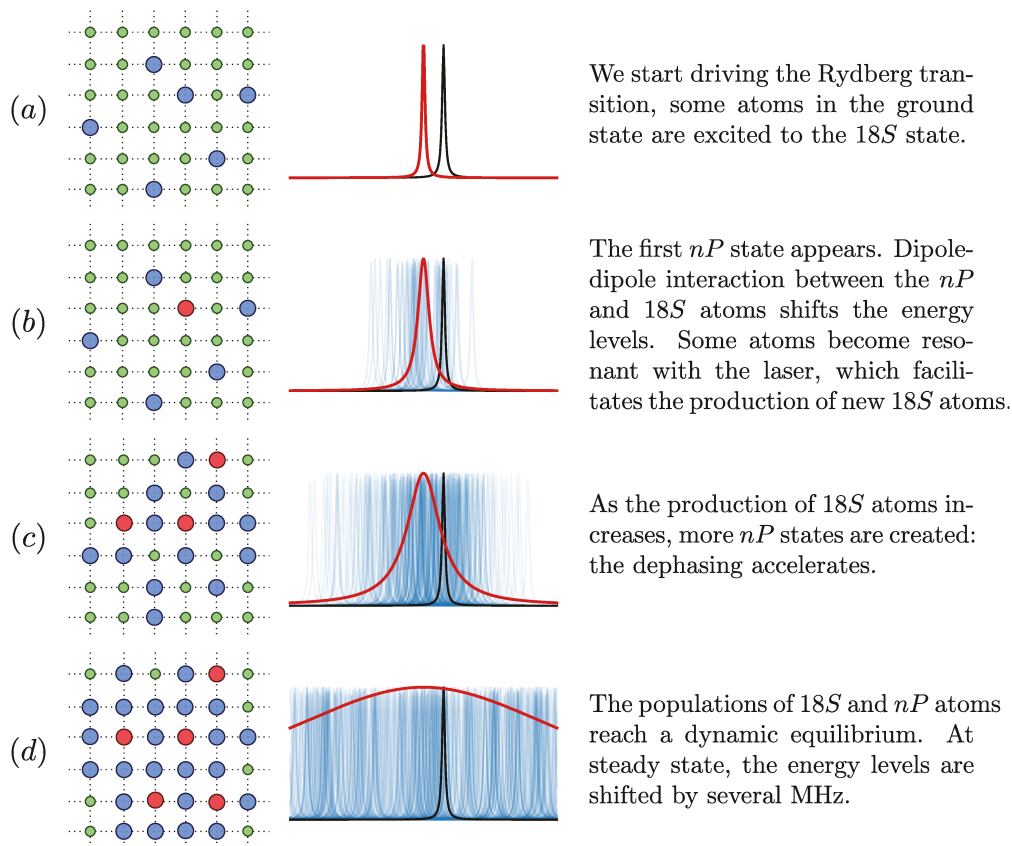


Figure 39 – **Broadening mechanism**

(*first column*) We represent the evolution of ground state atoms (in green), $18S$ states (in blue) and nP states (in red) in the optical lattice. (*second column*) The measured width (in red) corresponds to the average of the many individual spectra of the $18S$ atom (in blue). The laser excitation (in black) becomes more resonant as the broadening occurs.

4.1 DYNAMICS OF THE nS POPULATION

Decoherence in large Rydberg ensembles is the consequence of interactions between Rydberg atoms. Understanding the time evolution of the Rydberg populations is a critical step towards a full understanding of the phenomenon. Ultimately, controlling the populations could help mitigating the decoherence.

At first sight, the time evolution of the populations seems relatively complex: our initial observations suggest a highly correlated problem. This type of mechanisms is delicate to simulate and requires advanced simulation methods. Such an approach has been developed in our group[149], but we present here a much simpler model based on mean-field arguments.

These simulations can be compared to experimental data in order to confirm or infirm the model: as we will show in this section, the nS population can be measured directly by fluorescence. Observing the evolution of the pollutant population is more difficult and requires a specific technique discussed in the next section.

4.1.1 MEAN-FIELD MODELING

We describe the system with an ensemble of coupled non-linear rate equations based on phenomenological results and mean-field arguments. Although the physics behind involves strong correlations, this type of mean-field models is commonly adapted to situations with strong decoherence[6, 78].

Each atom is modeled as a three-level system, with a ground state $|g\rangle$, an excited state $|s\rangle$ and an ‘‘pollutant’’ state $|p\rangle$. We attribute to each $|i\rangle$ state a fraction ρ_i , so that the number of atoms in the state $|i\rangle$ is given by $N_i = \rho_i N$ and $\sum_i \rho_i = 1$. The levels are coupled by three transitions, $|g\rangle \rightarrow |s\rangle$, $|s\rangle \rightarrow |p\rangle$ and $|p\rangle \rightarrow |g\rangle$ to which we attribute the branching ratios b_1 , b_2 and b_3 (see Fig.40).

In our experiment the $|s\rangle$ state corresponds to the $18S$ level, the $|p\rangle$ state is a virtual state representing the four most probable pollutant states, $17P_{1/2}$, $17P_{3/2}$, $18P_{1/2}$, $18P_{3/2}$ (see Ch.2). We estimate the properties of the effective $|p\rangle$ state using a weighted average of the properties of these four states. Using the [ARC Library](#), we estimate $\Gamma_p = 25$ kHz, $b_1 = 0.49$, $b_2 = 0.18$ and $b_3 = 0.55$.

One should note that this picture is very simplified. In particular, there are many other desexcitation schemes than b_3 for $|p\rangle$. We also have $\sum_i b_i < 1$, which captures the fact that some atoms decay to sublevels of the ground state that are not the initial state of the Rydberg excita-

tion. When this occurs, the atoms cannot be repumped to the Rydberg state and are lost for the experiment.

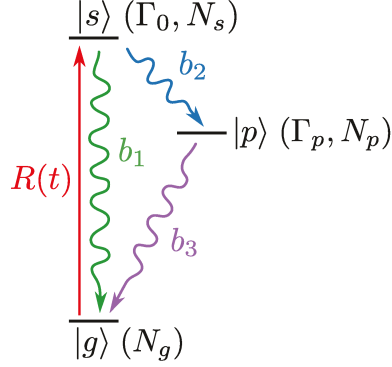


Figure 40 – **An effective three-level system**

Each atom is modeled as an effective three-level system, with ground state $|g\rangle$, Rydberg state $|s\rangle$ and pollutant Rydberg state $|p\rangle$. The levels are characterized by their lifetimes (Γ_0, Γ_p) , their populations (N_0, N_s, N_p) and their branching ratio (b_1, b_2, b_3) . The pumping rate R is time dependent because of the decoherence.

We assume the dephasing rate to be linear with the typical density of $n'P$ atoms

$$\Gamma(t) = \Gamma_0 + C_3 \rho_0 \rho_p(t) \quad (85)$$

We also consider the dephased pumping rate to be of the form

$$R(t) = \frac{\Gamma(t)}{2} \frac{2\Omega^2}{4\delta^2 + \Gamma^2(t)} \quad (86)$$

which corresponds to observations based on the steady-state limit studied in the previous chapter (see Ch.3). These two equations are based on mean-field arguments and do not take in account any inhomogeneities or cluster-like behavior.

With this, we can write the system of non-linear rate equations

$$\dot{\rho}_g(t) = -\rho_g(t)R(t) + \Gamma_0 b_1 \rho_s(t) + \Gamma_p b_3 \rho_p(t) \quad (87a)$$

$$\dot{\rho}_s(t) = \rho_g(t)R(t) - \Gamma_0 \rho_s(t) \quad (87b)$$

$$\dot{\rho}_p(t) = b_2 \Gamma_0 \rho_s(t) - \Gamma_p \rho_p(t) \quad (87c)$$

with Γ_0^{-1} the lifetime of $|s\rangle$ and Γ_p^{-1} the average lifetime of the pollutant states. We use Γ_0 (and not Γ) because the lifetime of the $|s\rangle$ is not altered by the dephasing. The decoherence is captured by the time evolution of

the pumping rate R .

We simulate the evolution of the populations for a resonant drive, $\delta = 0$ (see Fig.41). At early times, the model shows an overshoot of the $|s\rangle$ population followed by a maximum of the $|p\rangle$ population. The rapid growth of the $|s\rangle$ population happens before the creation of the first $|p\rangle$ atom, when R_0 is not yet altered. As soon as the first $|p\rangle$ atom appears, the resonant pumping rate decreases, thus reducing the number of $|s\rangle$ atoms. The massive decay of $|s\rangle$ atoms facilitates the apparition of a large number of $|p\rangle$. At longer times, both populations decrease due to the depopulation of the ground state.

The same simulation performed off-resonance ($\delta/2\pi = 2.1$ MHz) leads to slower dynamics (see Fig.42). Where the $|s\rangle$ population used to take only a fraction of $1\ \mu\text{s}$ to build up, it now requires nearly $15\ \mu\text{s}$ when the drive is off-resonant. This simply corresponds to a lower pumping rate at early times. We observe a similar — yet delayed — overshoot of the population followed by a global decrease of the Rydberg population.

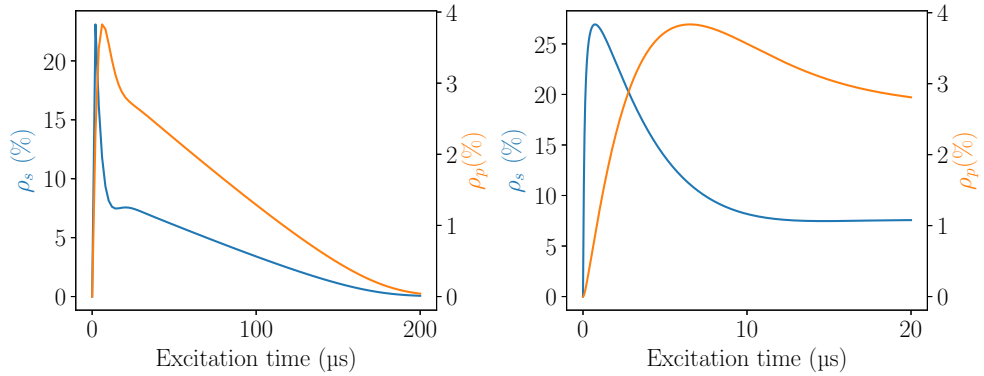


Figure 41 – **On-resonant $|s\rangle$ and $|p\rangle$ populations**

(left) We simulate the evolution of the $|s\rangle$ (blue) and $|p\rangle$ (orange) populations with $\Omega/2\pi = 140$ kHz and $\delta = 0$. (right) Zoom at early times.

4.1.2 DYNAMICS OF THE nS POPULATION

The evolution of the $|s\rangle$ population can be measured directly by fluorescence via pumped atoms. Similarly than in the previous chapter, we use the fact that the number of photons fluoresced on the $5S_{1/2} - 5P_{3/2}$ transition is proportional to the population of $|s\rangle$ atoms.

We collect the photons using a relay lens with high numerical aperture (NA=0.12) placed outside vacuum. A dichroic filter separates the fluorescence signal of the D₂ line ($\lambda = 780$ nm) from the Rydberg excitation photons ($\lambda = 795$ nm) slightly detuned from the D₁ line. We use a Laser

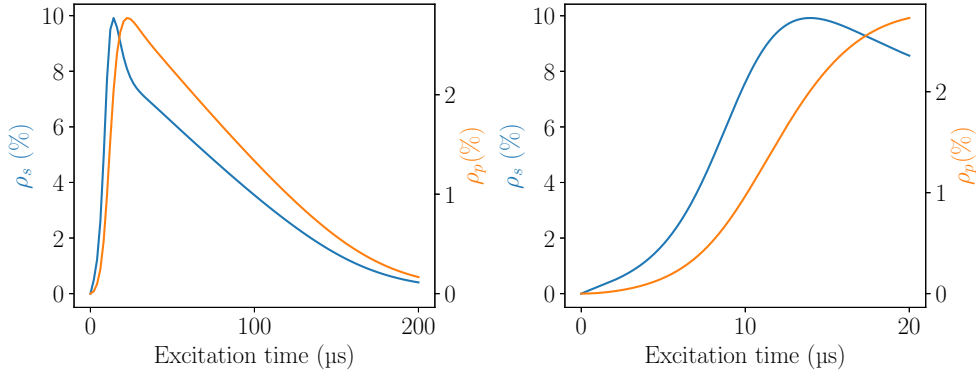


Figure 42 – **Off-resonant $|s\rangle$ and $|p\rangle$ populations**

(*left*) We simulate the evolution of the $|s\rangle$ (blue) and $|p\rangle$ (orange) populations with $\Omega/2\pi = 140$ kHz and $\delta/2\pi = 2.1$ MHz. (*right*) Zoom at early times.

Components Count 100-C-FC fibered avalanche photodiode to perform a time resolved detection. We typically collect less than 10 photons per run: obtaining quantitative data requires to build statistics over several hundreds of experiments.

On-resonance (see Fig.43) and off-resonance (see Fig.44) measurements show a good agreement with the model at long excitation times (typically a few tens of μ s), but discrepancies appear at shorter times. Since our model is based on mean-field arguments, we expect the predicted dynamics to be slower than the phenomenon. This translates into a slower increase of the width and a slower diminution of the resonant pumping rate in the model.

On-resonance data show an overshoot at early times, though much smaller than the one predicted. The strong correlations in the real system lead to a rapid disparition of the $|s\rangle$ population. Our model, which is slower because of its mean-field arguments, exhibits a delayed onset of decoherence. The population has more time to grow at the full single particle rate, hence leading to an overestimation of the $|s\rangle$ population at early times.

Off-resonant observations are also compatible with a beyond mean-field phenomenon. The quick growth of the Rydberg population is consistent with a rapid increase of the transition width. Due to its mean-field character, the width predicted by the model is growing slower, thus leading to an underestimation of both the off-resonant pumping rate and the Rydberg population.

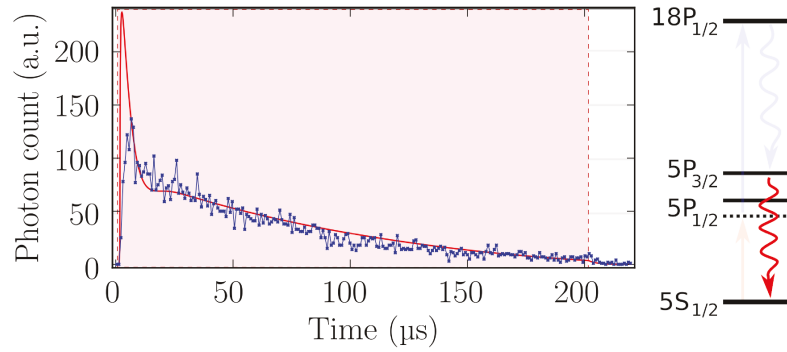


Figure 43 – **Time resolved measurement of the $|s\rangle$ population**

We drive the $5S_{1/2} \rightarrow 18S_{1/2}$ transition and measure the population of Rydberg state via the fluorescence of the D₂ line (*inset*). We excite the transition during 200 μs (red square) and compare the fluorescence measurement (blue trace) with the model (red trace). This data is taken with $\Omega/2\pi = 140$ kHz.

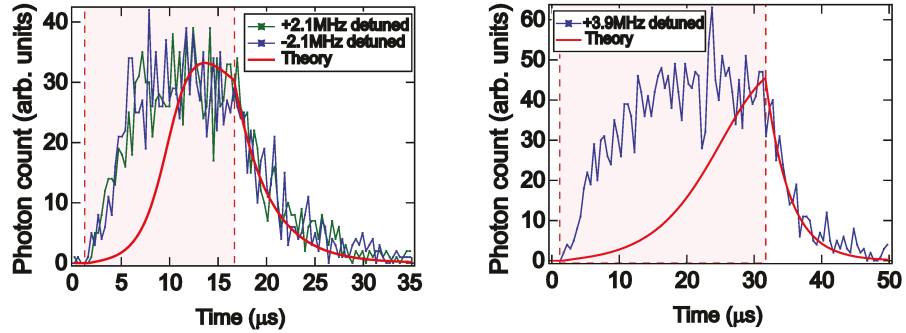


Figure 44 – **Evolution of the $|s\rangle$ population off-resonance**

We drive the transition during 200 μs (red square) and compare the fluorescence off the $5P - 5S$ transition with the model (red trace). The sign of the detuning (green and blue curves) does not modify the evolution of the population.

4.1.3 A STROBOSCOPIC EXPERIMENT

Along with understanding the phenomenon, mitigating the decoherence is a long-term goal. Our observations of the evolution of the $|s\rangle$ states already suggest a first experimental scheme.

Off-resonance fluorescence measurements show that the population of $|s\rangle$ states typically requires a few microseconds to build up. The population of $|p\rangle$ states is expected to be even slower to appear, thus providing several microseconds before the broadening occurs. This suggests using narrow excitation pulses separated by long dark times, so as to build up the $|s\rangle$ population without being affected by the decoherence.

Using this approach, the dressed interaction could be time-averaged over many pulses. This technique could be used for experiments where the observable does not rely on correlations being preserved during the dark time.

An estimate of the typical time available before the apparition of the first $|p\rangle$ state, τ_c , can be extracted from the lifetime of the $|s\rangle$ state, Γ_0 , weighted by the population in this state, N_s , and the branching ratio to the $|p\rangle$ state, b ,

$$\tau_c^{-1} = N_s b \Gamma_0 \quad (88)$$

and the number of $|s\rangle$ atoms in the system is given by

$$N_s = \frac{NR}{\Gamma_0} = \frac{R_0 \Gamma_0}{4\delta^2} \quad (89)$$

where we have assumed $\delta/\Gamma \gg 1$ which is always true at the beginning of the experiment. We combine the previous equations with the experimental observation $R_0 = \Omega^2/\Gamma$ and get

$$\tau_c = \frac{1}{bN\Gamma_0} \left(\frac{2\delta}{\Omega} \right)^2 \quad (90)$$

In the case of $n = 18$, $\Gamma_0 = 45$ kHz, $N = 40000$, assuming $\Omega/2\pi = 66$ kHz and $\delta/2\pi = 1$ MHz, we get $\tau_c = 10$ μ s.

To calculate the time-averaged dressing potential, we define the dark time $\tau_{\text{dark}} = A\tau_0$ with $A \gg 1$ and τ_0 the lifetime of the $|s\rangle$ state. Considering a short-distance dressing potential, $U_2 = \Omega^4/8\delta^3$ (see Ch.3), the interaction energy averaged over the pulses becomes

$$U^* = \left(\frac{\Omega^4}{8\delta^3} \right) \frac{\tau_c/\tau_0}{A + \tau_c/\tau_0} \quad (91)$$

Taking the optimistic conditions from[87], $\Omega/2\pi = 10$ MHz and $\delta/2\pi = 100$ MHz, we find $U_2 = 8$ kHz. Assuming $A = 18$ (corresponding to $\tau_{\text{dark}} = 80$ μ s, $\tau_0 = 4.5$ μ s, $n = 18$), the time-averaged interaction energy reduces to $U^* = 0.9$ kHz. All other parameters maintained, more reasonable values such as $\Omega/2\pi = 66$ MHz and $\delta/2\pi = 1$ MHz lead to $U_2 = 15$ Hz and $U^* = 1.7$ Hz. The interaction energy is still orders of magnitude below the typical resonance frequencies of the traps.

We perform the experiment with a serie of N_p pulses of length $t_p = 0.5 - 40$ μ s separated by 80 μ s of dark time. The number of pulses N_p is adjusted so that the total excitation time is kept constant. Experimentally, the pulses are performed with an AOM on the red laser while the blue laser is kept on during the full duration of the experiment.

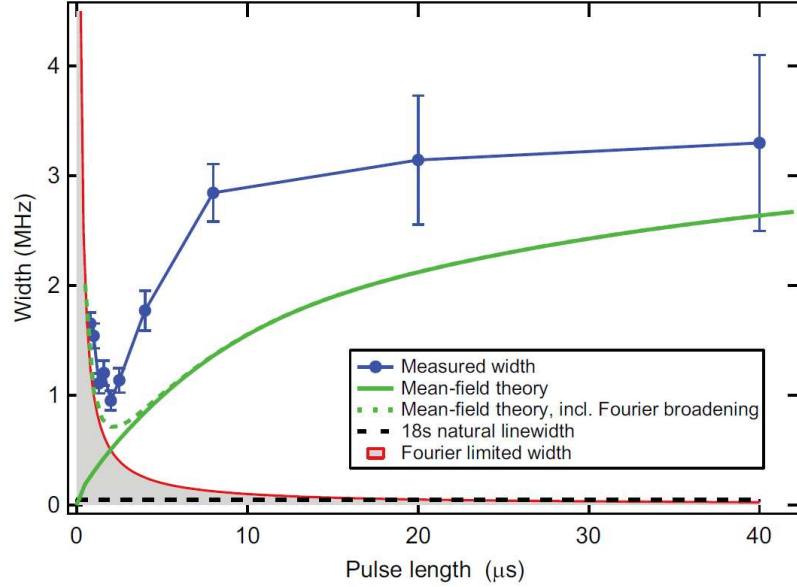


Figure 45 – **Evolution of the width of the Rydberg spectra as a function of the excitation time**

We excite the Rydberg transition stroboscopically at $\Omega/2\pi = 66$ kHz and measure the width of the transition. The number of pulses is chosen accordingly with the pulse duration, so that all datapoints have the same total excitation time. Errorbars corresponds to the residuals of Lorentzian fits. The model (in green) reproduces the trend while being slower than the data (blue dots). Short excitation times are limited by Fourier broadening (gray zone).

We observe a clear diminution of the measured width in the case of short pulses (see Fig.45). However, the minimum measured width is about 1 MHz, which is still more than 20 times the natural linewidth. We attribute this limitation to the Fourier limit, which leads to broad spectra at short pulse times.

Besides, this technique cannot be used for experiments requiring long coherence times because the coherence is reset at each excitation pulse. While succeeding in probing the dynamics of the phenomenon, there is little hope to use this technique for Rydberg dressing in large ensembles.

4.2 DYNAMICS OF THE $n'P$ POPULATION

4.2.1 A PUMP-PROBE TECHNIQUE

The symptoms of the decoherence in large Rydberg ensembles have been observed in several experiments, notably by the Houston team[1, 46, 60]. However, a measurement of the time evolution of the pollutant population is still missing in the literature. The desexcitation scheme of the $|p\rangle$ population is relatively complex and measurement techniques well-suited

for the $|s\rangle$ population cannot be used for the $|p\rangle$ population.

The evolution of the $|p\rangle$ population is difficult to measure because the creation and the detection of contaminants states are coupled: evaluating the $|p\rangle$ population by measuring the properties of a Rydberg transition creates additional $|p\rangle$ states that affect the transition. This mechanism of *self*-broadening, in which the Rydberg transition creates the contaminants and gets affected by them, prevents from using a single transition to measure the time-evolution of the contaminants.

In this section, we present an indirect method to count the $|p\rangle$ states. Our technique takes advantage of the fact that all sublevels of the $|s\rangle$ state can resonantly dipole-dipole interact with the contaminants. This suggests using two transitions at the same time, one as a sensor for the pollutant states (the “probe”), the another as an external source of contaminants (the “pump”). Both transitions are affected by their own contaminants (self-broadening), and by the contaminants produced by the other transition (cross-broadening). Creation and detection of additional contaminants are effectively decoupled, thus opening the door for dynamic investigations.

We model each atom as a six-level system, with two ground states $|g\rangle$ and $|g'\rangle$, two Rydberg nS states $|s\rangle$ and $|s'\rangle$, and two $n'P$ states $|p\rangle$ and $|p'\rangle$ (see Fig.46). The pump transition drives the $|g\rangle \rightarrow |s\rangle$ transition, the probe the $|g'\rangle \rightarrow |s'\rangle$. Weakly driving the probe creates a very limited number of $|s'\rangle$ states, and an even smaller number of $|p'\rangle$ states, so that the population of contaminant states is mostly represented by $|p\rangle$ states. Both the pump and the probe get broadened by their interaction with the contaminant states in the system. However, since the number of $|p'\rangle$ states is negligible, the probe has almost no self-broadening and is mostly affected by pure cross-broadening, making it an effective sensor for the $|p\rangle$ population.

4.2.2 STEADY-STATE CROSS-BROADENING

As a first experiment, we compare the properties of the probe transition with and without the presence of additional $|p\rangle$ states. This is done in the steady-state regime. Experimentally, we use the sublevels of the $5S_{1/2}$ and $18S_{1/2}$ to drive two independent transitions between these states.

We extend the results found in the previous chapter in the case of several sources of $|p\rangle$ states. Assuming N_t transitions $|g\rangle \rightarrow |s\rangle$ with resonant pumping rate $R_0^{(i)}$ and an atomic fraction available for Rydberg excitation $f^{(i)}$, we get a width for all transitions

$$\Gamma = \Gamma_0 + \beta_3 \rho_0 \sum_i^{N_t} R_0^{(i)} f^{(i)} \quad (92)$$

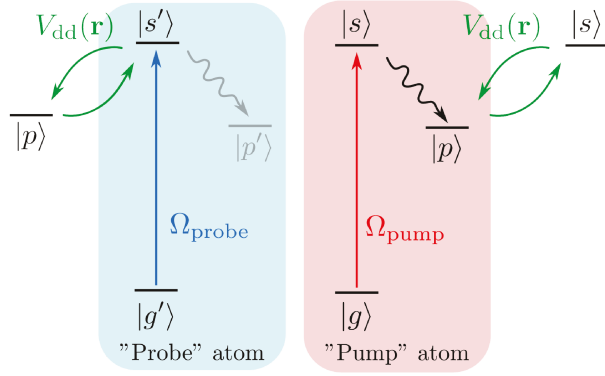


Figure 46 – **Principle of the pump-probe technique**

A pump transition $|g\rangle \rightarrow |s\rangle$ is used as a tunable source of pollutant states. A weakly driven $|g'\rangle \rightarrow |s'\rangle$ probe transition is affected by the additional states created by the pump. This transition serves as detector of pollutant states. Such scheme allows to separate the creation and detection of pollutant states.

Where β_3 is an average interaction volume defined as $\beta_3 = \sum |C_3^{(nP)}| b^{(nP)} / \Gamma^{(nP)}$, with $b^{(nP)}$ the branching ratio to the nP state and $\Gamma^{(nP)}$ its decay rate. For $18S$ and only considering the four most represented nP states, we find $C_3 = 13 \text{ MHz } \mu\text{m}^3$ (including the root mean square average of the angular dependency) and $\beta_3 = 108 \mu\text{m}^3$.

Using the fact that $R_0 \approx \Omega / \sqrt{\rho_0 \beta_3}$, we find

$$\Gamma = \Gamma_0 + \sqrt{\rho_0 \beta_3} \sum_i \Omega^{(i)} \sqrt{f^{(i)}} \quad (93)$$

With a similar development, we get

$$R_0 = \frac{1}{\sqrt{\rho_0 \beta_3}} \sum_i \frac{\Omega^{(i)}}{\sqrt{f^{(i)}}} \quad (94)$$

To test these equations, we compare the properties of the probe transition with and without an external source of pollutant states. The introduction of additional contaminants should lead to broader linewidths and increased resonant pumping rates.

4.2.2.1 EXPERIMENTAL SCHEME

We use the $|5S_{1/2}, F = 2, m_F = 1\rangle \rightarrow |18S_{1/2}, F = 1, m_F = -1\rangle$ as the probe and $|5S_{1/2}, F = 2, m_F = -2\rangle \rightarrow |18S_{1/2}, F = 2, m_F = -2\rangle$ as the pump (see Fig.47). Their initial states are populated with a fractional density $f_p \times \rho_0$ for the probe and $f_P \times \rho_0 = (1 - f_p) \times \rho_0$ for the pump. The two transitions are separated by the hyperfine splitting $\Delta_{HF}/2\pi = 10 \text{ MHz}$ of the $18S_{1/2}$ Rydberg state.

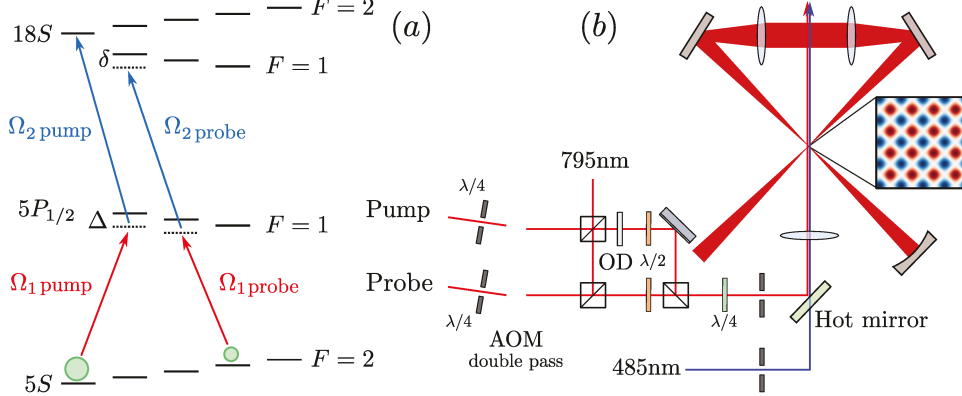


Figure 47 – **Setup for the pump-probe technique**

(a) We use the $5S_{1/2}$ and $18S_{1/2}$ sublevels to drive two independent transitions. (b) The two transitions share the same blue laser. The red laser is a superposition of a σ^+ and a σ^- beam which independently drive the probe and the pump.

To optimize the contrast between the “probe only” and the “probe and pump” cases, we strongly imbalance the probe and the pump, resulting in a small broadening in the “probe only” case and a large broadening in the “probe and pump” case. However, both experiments must be performed during the same experimental time, thus limiting the possible range for Ω_p, Ω_P, f_p and f_P . At a given excitation time, too small values of Ω_p and f_p will not provide enough signal and too large values of Ω_P and f_P will fully depopulate the ground state.

4.2.2.2 MEASURED WIDTH

We drive the pump on resonance ($\delta_P = 0$) and perform spectroscopy on the probe. We compare the width of the probe with and without the pump (see Fig.48). The spectra taken in presence of additional pollutant states are clearly broader than the one without.

We set $f_p = 25\%$ and $\Omega_p/2\pi = 14$ kHz, which leads to a theoretical estimate of the pure self-broadened width $\Omega_p\sqrt{\beta f_p \rho_g} = 2\pi \times 570$ kHz. Our measurement leads to a slightly lower value, $\Gamma_{\text{self}} = 10 \times \Gamma_0 = 2\pi \times 450$ kHz. Driving the pump transition with $f_P = 75\%$ and $\Omega_P/2\pi = 20$ kHz, we expect a width of order of 2 MHz. The measured width is quite lower, $\Gamma_{\text{self+cross}}/2\pi = 860$ kHz.

The discrepancy between the data and the scalings might be partly explained by the timing of the excitation: we drive both transitions during the same excitation time ($t_k = 300$ μ s). The population of pollutant states is not fully built up when we start the spectroscopy, which might lead to an overestimation of the pollutant population (see the inset of Fig.48). We have also considered that all resonant dipole-dipole interactions in the system are characterized by the same C_3 , which is a questionable

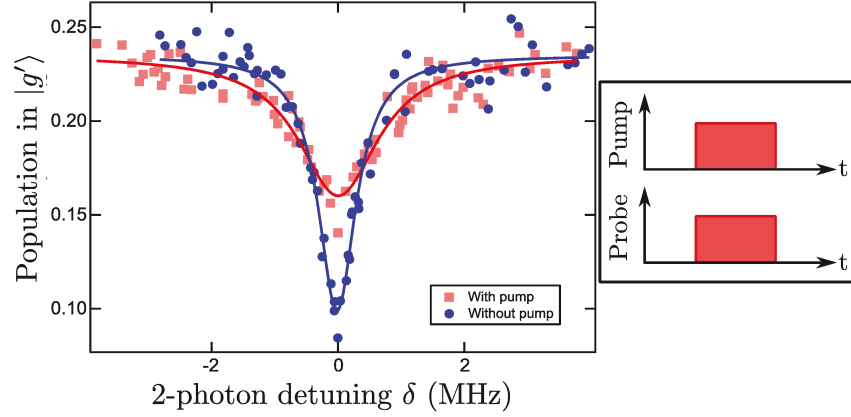


Figure 48 – **Effect of the pump on the probe spectrum**

We compare the spectrum of the probe transition with (red curve) and without (blue curve) additional pollutant states.

hypothesis. The calculation of the C_3 is a weighted average of the C_3 characterizing the four most representative $n'P$ states in the system.

4.2.2.3 RESONANT PUMPING RATE

With the settings $f_p = 30\%$ and $\Omega_p = 2\pi \times 72$ kHz, we scan the excitation time t_k and measure the depopulation of the ground state of the probe transition. We then resume the experiment with the pump activated. This excitation is run before turning on the probe transition so that the population of pollutant states is fully built up during the experiment (see the inset of Fig.49). With $f_P = 70\%$ and $\Omega_P = 2\pi \times 84$ kHz, we get $R_{0,\text{self+cross}} = 0.50 \text{ ms}^{-1}$, which compares to $R_{0,\text{self}} = 0.29 \text{ ms}^{-1}$ without the pump (see Fig.49).

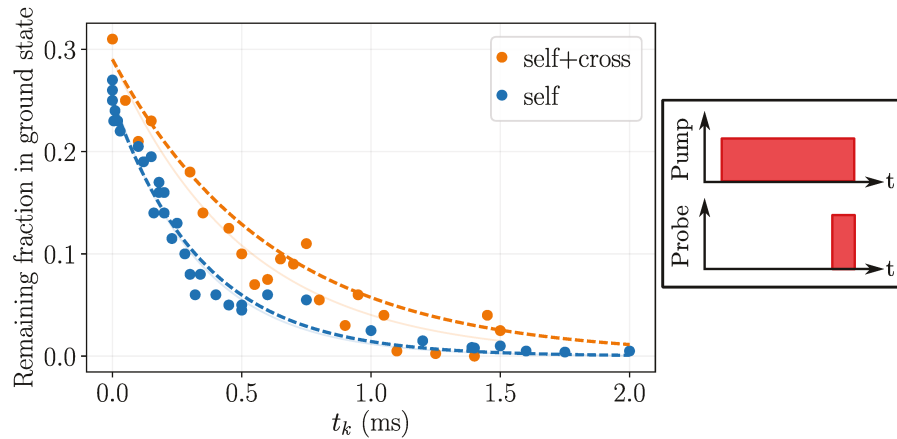


Figure 49 – **Steady-state pump-probe experiment**

We compare the resonant pumping rate with (orange) and without (blue) the additional pollutant states. Experimental data match the theory without adjustable parameters (dashed lines).

This time, the measurements show a remarkable agreement with the values expected from Eq.(94), which is a further confirmation of the technique.

4.3 DYNAMICAL CROSS-BROADENING

In this section, we combine the pump-probe technique and stroboscopic excitations to investigate the dynamics of the pollutant population.

4.3.1 CROSS-BROADENING HOMOGENEOUS MEAN-FIELD MODEL

The cross-broadening model is based on two coupled three-body systems similar to the previous ones (see Sec.4.1.1). Each atom i is described as a three-level system referred to as $|i, g\rangle$, $|i, s\rangle$ and $|i, p\rangle$. This effective six-level system captures the effect of the pump on the probe, and reciprocally.

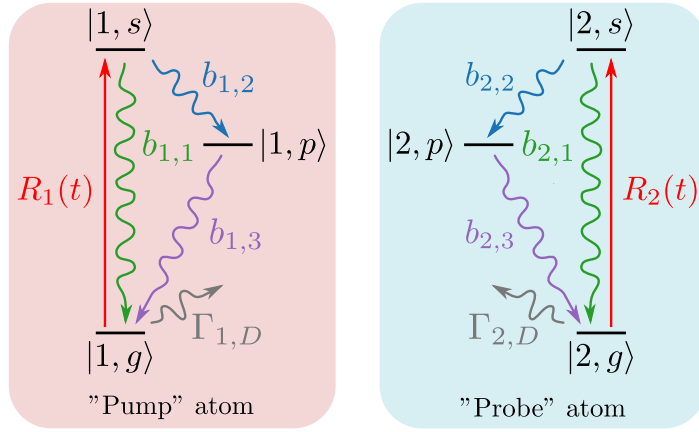


Figure 50 – **Model for the cross-broadening**

We model the experiment as an effective six-level system corresponding to two coupled three-level atoms.

In the following, we consider the states $|1, i\rangle$ as corresponding to the pump and $|2, i\rangle$ as corresponding to the probe. The system writes

$$\begin{aligned} \dot{\rho}_{1,g}(t) = & -\rho_{1,g}(t)R_1(t) + \Gamma_0 b_{1,1}\rho_{1,s}(t) \\ & + \Gamma_p b_{1,3}\rho_{1,p}(t) - \Gamma_{1,D}\rho_{1,g}(t) \end{aligned} \quad (95a)$$

$$\dot{\rho}_{1,s}(t) = \rho_{1,g}(t)R_1(t) - \Gamma_0\rho_{1,s}(t) \quad (95b)$$

$$\dot{\rho}_{1,p}(t) = b_{1,2}\Gamma_0\rho_{1,s}(t) - \Gamma_{1,p}\rho_{1,p}(t) \quad (95c)$$

$$\begin{aligned} \dot{\rho}_{2,g}(t) = & -\rho_{2,g}(t)R_2(t) + \Gamma_0 b_{2,1}\rho_{2,s}(t) \\ & + \Gamma_p b_{2,3}\rho_{2,p}(t) - \Gamma_{2,D}\rho_{2,g}(t) \end{aligned} \quad (95d)$$

$$\dot{\rho}_{2,s}(t) = \rho_{2,g}(t)R_2(t) - \Gamma_0\rho_{2,s}(t) \quad (95e)$$

$$\dot{\rho}_{2,p}(t) = b_{2,2}\Gamma_0\rho_{2,s}(t) - \Gamma_{2,p}\rho_{2,p}(t) \quad (95f)$$

In Eq.(95a),(95d), the last terms correspond to off-resonant scattering to the $5P_{1/2}$ state. Its rates evolves as $\Gamma_{i,D} = (\Omega_{1,i}/2\Delta_i)^2\Gamma_{5P}$, with $\Gamma_{5P} = 2\pi \times 6$ MHz. We use the same mean-field argument than before, which assumes that the dephasing rate depends on the density of contaminants.

$$R_1(t) = \frac{\Gamma_1}{2} \frac{2\Omega^2}{4\delta_1^2 + \Gamma_1^2} \quad (96a)$$

$$R_2(t) = \frac{\Gamma_2}{2} \frac{2\Omega^2}{4\delta_2^2 + \Gamma_2^2} \quad (96b)$$

We keep $\Gamma_p = 2\pi \times 25$ kHz and $C_3 = 2\pi \times 34$ MHz μm^3 for both the pump and the probe. The cross-broadening is captured by an effective interaction term $C_3^{(\text{cross})}$ which depends on the transitions at stake and is a fitting parameter for the model.

$$\Gamma_1(t) = \Gamma_0 + C_3\rho_0\rho_{1,p} + C_3^{(\text{cross})}\rho_0\rho_{2,p} \quad (97a)$$

$$\Gamma_2(t) = \Gamma_0 + C_3\rho_0\rho_{2,p} + C_3^{(\text{cross})}\rho_0\rho_{1,p} \quad (97b)$$

4.3.2 DYNAMICAL CROSS-BROADENING EXPERIMENT

To measure the evolution of the additional $|p\rangle$ states, we build up the population with a short pulse of pump light at $t = 0$ and measure the effect of the contaminants with a pulse of probe light after a delay Δt . Since the cross-broadening appears only when the additional $|p\rangle$ states and $|s\rangle$ states are both present in the system, we expect a maximal broadening at short delays and pure self-broadening for $\Delta t \gg \Gamma_0^{-1}$. The evolution of the width of the probe transition gives an estimate of the dynamics of the additional $|p\rangle$ states.

In practice, dynamical investigations of the $|s\rangle$ population (see Sec.4.1.2) show that the Rydberg population can take several tens of microseconds to build up, the precise timing depending on the two-photon detuning δ . We take $t_p = 20 \mu\text{s} \sim 3\tau_0$ for both the pump and the probe pulses. This value allows to investigate the the range $\delta/2\pi \in [-3, 3]$ MHz with sufficient signal but below saturation.

Probing a unique pump pulse leads to a small signal: we hence repeat the experiment several times, each new experiment separated by a long

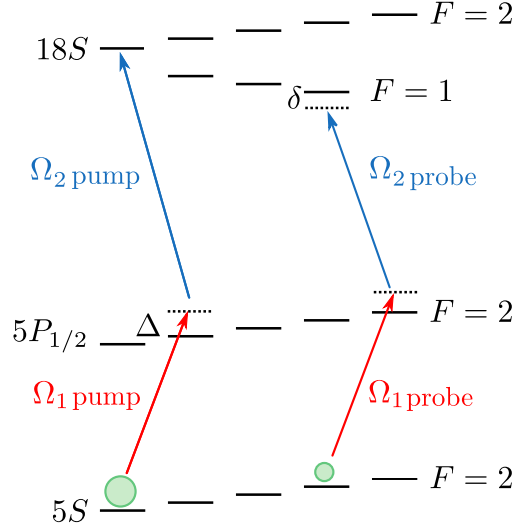


Figure 51 – **Dynamical pump-probe experimental setup**

Contrary to the steady-state experiment, this one uses a blue intermediate detuning: this allows to use the $|5P_{1/2}, F = 2, m_F = 2\rangle$ sublevel as intermediate state for the transition.

dark time in order to let all excited atoms decay back to the ground state before the new excitation. We set $t_{\text{dark}} = 3 \times \tau_p$, which leads to a full period of 120 μs .

We use $|1, s\rangle = |18S_{1/2}, F = 2, m_F = -2\rangle$ and $|2, s\rangle = |18S_{1/2}, F = 1, m_F = 1\rangle$. We set $\Omega_{\text{pump}} = 2\pi \times 20$ kHz and $\Omega_{\text{probe}} = 2\pi \times 15$ kHz, with an intermediate detuning $\Delta = 2\pi \times 240$ MHz. Contrary to the steady-state experiment (see Sec.4.2.2), the two-photon scheme is blue-detuned (see Fig.51). We chop the excitation light (see Fig.52 insets) of the pump and the probe with two independent AOM. Only the red light is chopped, the blue laser is kept on during the full duration of the experiment. As usual, the measured widths are extracted from a Lorentzian fit.

We observe a clear evolution of the probe width (see Fig.52), which goes from $\Gamma = 2\pi \times 760$ kHz (pump and probe in phase) to $\Gamma = 2\pi \times 500$ kHz (pump and probe out of phase).

We apply the model of cross-broadening to this data: our model leads to a correct estimate of the amplitude of broadening. There is however a consistent 10 μs delay between experiment and simulation. We attribute this delay to the mean-field assumptions in the model which fail to capture the early time dynamics.

This measurement gives an estimate of the typical times necessary to build and wipe out the population of contaminant in the system. Building the population is a relatively quick process (saturation after 10 μs), while

the complete disparition of the pollutant states can take up to $40 \mu\text{s}$.

To our knowledge, this is the first observation of the $|p\rangle$ population in this context. This measurement not only confirms the mechanism but also indicates the typical timescales at stake. However, compared to other techniques (*e.g.* fluorescence), this method has a relatively low temporal resolution. We believe that specific methods such as state-selective field ionization[69] might have allowed a more accurate measurement. This technique has not been considered in our work because of the deep modifications in the experimental apparatus it would have involved.

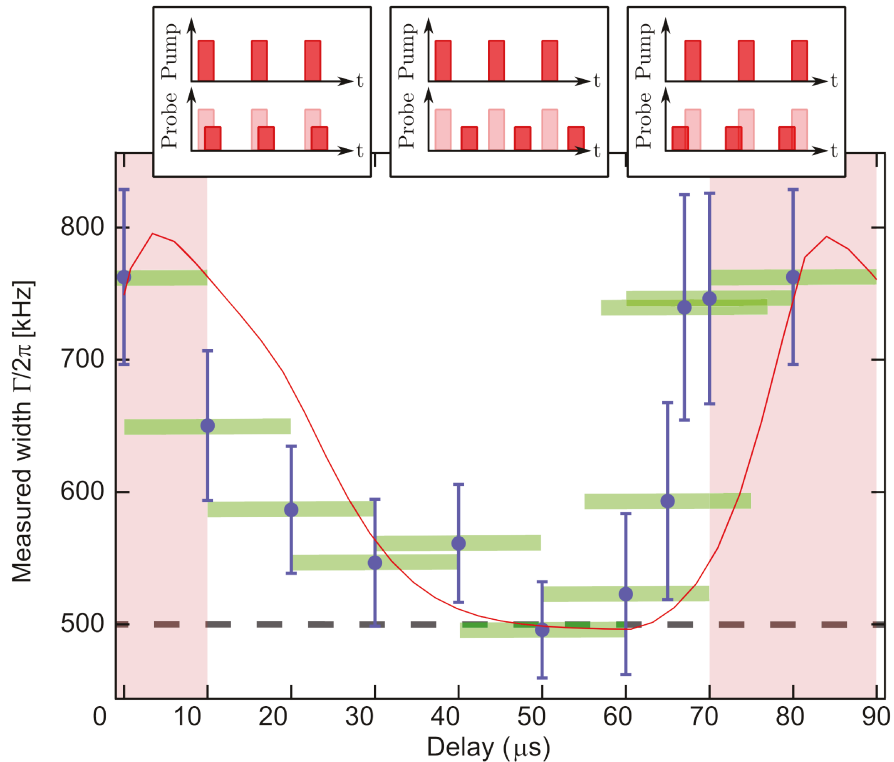


Figure 52 – **Dynamical pump-probe experiment**

We measure the time evolution of the pollutant population by measuring the width of the probe transition at arbitrary delays (blue data points). The pump pulses are represented as red squares, the solid red line is the mean-field model.

4.4 POSSIBLE WORKAROUNDS

In this section, we present investigations concerning possible workarounds to limit the decoherence. As far as large Rydberg ensembles are concerned, no ultimate solution has been identified so far. Nonetheless, our study can help few-body experiments to increase the number of particles in their system with the safest approach.

4.4.1 STROBOSCOPIC APPROACH

We have seen in Sec.4.1.3 that a stroboscopic approach can help to limit the decoherence. Short excitations times t_p followed by long dark times $t_{\text{dark}} \gg \tau_0$ allow to limit the broadening.

The time available before the apparition of the first contaminant τ_c provides an estimate of the actual coherence time available. τ_c^{-1} typically corresponds to the number of atoms in the $|s\rangle$ state multiplied by their probability to transfer to a nearby $|p\rangle$ state, $\tau_c^{-1} = N (\Omega/2\delta)^2 \Gamma_0$, which can be written

$$\frac{\tau_c}{\tau_0} = \frac{4\delta^2}{\Omega^2} \frac{1}{bN} = \frac{N_c}{N} \quad (98)$$

where N_c is a critical number of atoms above which the coherent time available drastically reduces.

We note that using larger samples (large N) should provide more coherence time. Besides, using larger principal quantum numbers leads to high values of τ_0 ($\tau_0 \propto n^3$ [53]), that also postpone the apparition of the first pollutant state. However, high n also lead to larger interactions ranges: once the first pollutant state appears, the avalanche dephasing is much more dramatic.

The stroboscopic approach can reduce the broadening down to the Fourier limit (see Sec.4.1.3). Avoiding the Fourier broadening requires $\tau_c \gg \delta^{-1}$, which imposes $N \ll N_c \delta / \Gamma_0$. The dark times between the pulses do not preserve quantum correlations: this reduces the experimental possibilities of this technique, especially for Hamiltonian engineering. This technique has been used in other experiments involving Rydberg dressing, notably by the Munich group[150].

4.4.2 MICROWAVE CAVITIES

We have seen in the previous sections that the decoherence is triggered by the apparition of blackbody induced pollutant states. Thermal photons are present at room temperature and can seem unavoidable at first glance. However, atomic absorption and radiative properties are strongly influenced by the environment of the sample[112]: for example, inserting atoms in a cavity or a waveguide drastically modifies their radiative properties due to the Purcell effect[91]. In the particular case of Rydberg atoms, it has been shown that their absorption of blackbody radiation[142] and their spontaneous emission[80] can be dramatically reduced by placing the sample in a microwave cavity. This can be used to increase their lifetime.

For a given transition, the rate of radiative absorption is given by $A\bar{n}$, where A is the spontaneous transition rate and \bar{n} the photon occupation number, $\bar{n}(T, \nu) = [\exp(h\nu/kT) - 1]^{-1}$. A is proportional to the mode density for photons at frequency ν , $\rho(\nu)$, which defines as $\rho(\nu) = 4\pi\nu^2/c^3$ in free space.

Optical cavities, such as Fabry-Pérot cavities, strongly modify the propagation of the electric field. In the particular case of Rydberg atoms, such cavities can be used as “cut-off” cavities, which filter all transitions below a critical frequency defined as $\nu_c = c/2d$, where d is the distance between the two plates.

Atoms in cavities are deceptively simple: taking in account the finite size of the plates, their imperfect electrical conductivity, the inhomogeneities of the cloud and the occupation of the energy levels deeply complicates the problem. Taking in account all these corrections is beyond the scope of this section, we only evaluate here the experimental possibilities of such systems.

Under the simplistic assumptions of two parallel plates with infinite size and perfect conductivity, the cavity allows two families of electrical modes: one type parallel to the normal of the plate, the other one orthogonal. In the frequency region $0 \leq \nu \leq 2\nu_c$, the two types of density of modes evolve as^[142]

$$\rho_{\parallel} = 4\pi \frac{\nu_c \nu}{c^3} \quad (99a)$$

$$\rho_{\perp} = \begin{cases} 4\pi\nu_c\nu/c^3 & \text{for } \nu > \nu_c \\ 0 & \text{for } \nu < \nu_c \end{cases} \quad (99b)$$

The selection rules for blackbody absorption also show that ρ_{\parallel} couples transitions with $\Delta|m| = 0$ and ρ_{\perp} transitions with $\Delta|m| = 1$ when the quantization axis is orthogonal to the plates. Cut-off cavities are only filtering one family of modes, and therefore only a fraction of all possible transitions.

Circular Rydberg states^[81], *i.e.* states satisfying $|m| = n - 1$ constitute a remarkable exception. These atoms radiate only by a single dipole transition, which happens to correspond to a ρ_{\perp} mode. A cavity combined with these states can effectively block the only possible blackbody transfer. Circular Rydberg states in cavities have been used in the past, and notably in the famous Haroche experiments^[59].

In the case of non-circular Rydberg states, it is worth evaluating the reduction of blackbody transfers provided by a cavity. We use the ARC Library to calculate the energy of each transition coupling the $18S$ level with a nP state, $n \in [5, 100]$. Setting a cavity length allows to extract a

cutting frequency ν_c , and transitions with energy $\hbar\nu < \hbar\nu_c$ are expected to be blocked. We estimate to 75% the reduction of the radiative absorption in the ρ_\perp mode for $18S$ atoms in a cavity of length $l = 130\ \mu\text{m}$. Using such a cavity, however, is challenging due to laser clipping.

Because of their dense spectrum, higher Rydberg atoms are compatible with larger cavity sizes. The same 75% filtering can be achieved with $l = 4\ \text{mm}$ and $50S$ atoms or $l = 12.5\ \text{mm}$ and $70S$ atoms. Such high-Rydberg states, however, are not compatible with optical lattices due to Rydberg blockade (see Ch.2). Besides, their relatively long lifetimes ($\sim 100\ \mu\text{s}$) are sufficient for tweezer-based experiments (see Ch.5).

Non-circular Rydberg states have also been tested experimentally. Using the $29D \rightarrow 30P$ transition, D. Kleppner reported a decrease of 59% of the absorption rate below the cutoff frequency. The experiment was performed with copper plates 40 mm in diameter and separated by a distance $r = 2\ \text{mm}$ [142]. Addressing and detection techniques used at the time, however, need to be adapted to current experimental schemes. In this type of experiments, high Rydberg levels are favorable, in the sense that they lead to larger cavity size, hence better optical access.

4.4.3 CRYOGENIC TEMPERATURES

Another approach consists in reducing the number of thermal photons by working in a cryogenic environment. In fact, most experiments using Rydberg atoms in a cavity work at cryogenic temperatures (*e.g.* $T = 0.8\ \text{K}$ in the Haroche team, $T = 6.5\ \text{K}$ in the Kleppner group, *etc.*). However, cooling the entire system can be technically difficult, notably because of the current atom and trapping techniques: usual cryocoolers have relatively low cooling power, that can easily be overwhelmed by laser-induced heating. Experimental challenges concerning cryogenic experiments are discussed in more detail in Ch.5.

4.4.3.1 PARALLEL COLD PLATES

We first consider the simplistic case of an atomic sample placed between two cold plates of an insulating material separated by a distance d . Assuming that each plate has a radius r , the solid angle of the shield is given by

$$\Omega_{\text{shield}} = 4\pi [1 - \cos(\varphi)] \quad (100)$$

with $\tan(\varphi) = 2r/d$.

We evaluate the number of photons reaching the center of the system as

$$N_{\text{ph}} = \sum_{\nu} [1 - \cos(\varphi)] \bar{n}(T, \nu) + \cos(\varphi) \bar{n}(300 \text{ K}, \nu) \quad (101)$$

Where T is the temperature of the plates. We sum all the photons with energy $h\nu$, so that ν corresponds to a transition from the nS state of interest to a $n'P$ state.

We simulate this system in several configurations (see Fig.53 and Fig.54).

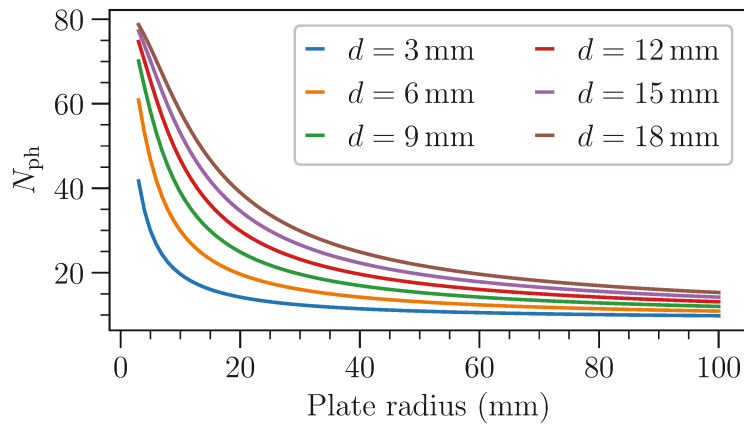


Figure 53 – **Evolution of N_{ph} with the distance between the plates**

We simulate N_{ph} for two disks at $T = 77 \text{ K}$ separated by a distance $d \in [3 - 18] \text{ mm}$ for the $n = 18$ Rydberg level.

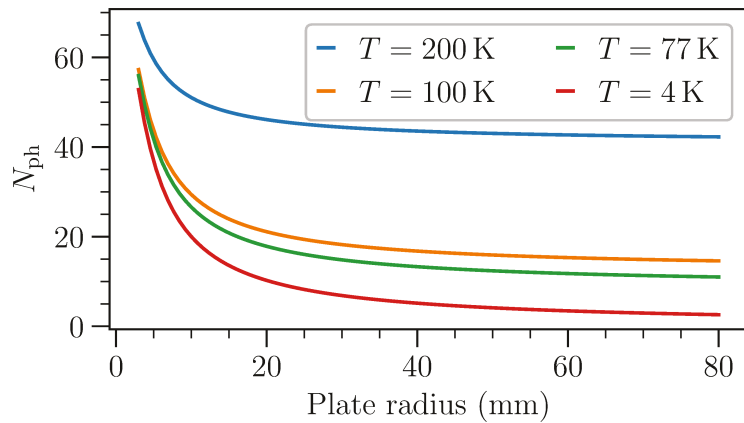


Figure 54 – **Influence of the temperature on N_{ph}**

We simulate N_{ph} for two disks at $T = 5 \text{ mm}$ for $T = 4 - 200 \text{ K}$ and $n = 18$.

Under realistic conditions ($T = 77 \text{ K}$, $d = 6 \text{ mm}$, $r = 40 \text{ mm}$), this shield could reduce N_{ph} by a factor 4. Such an experimental system could

be produced with liquid N₂-cooled alumina, which is an insulator with reasonable thermal conductivity. Using cold glass plates with a conductive coating (*e.g.* Indium Tin oxide) could combine a cold shield with a cavity effect, though limitations due to the poor conductivity of ITO and thermal properties of glass must be addressed.

4.4.3.2 COHERENCE TIME IN A CRYOGENIC ENVIRONMENT

Going back to the avalanche dephasing in large Rydberg ensembles, we now consider the case of a fully cryogenic experiment. This implies a cold shielding, which (optical access neglected) would block thermal radiation on the full 4π solid angle. Such platform would involve a cryocooler[123], whose design would be adapted to the range of temperatures required. As this is the solution we have identified, technical considerations and designs are detailed in the next chapter (See Ch.5).

We have shown that the available coherent time is typically given by τ_c (see Eq.(98)). This time depends both on the branching ratio to nearby $n'P$ states and the lifetime of the nS state, two parameters that are temperature dependent.

Lowering the temperature of the environment diminishes the stimulated emission of thermal photons, and therefore the decay rate of nS states. However, the difference in lifetime between room and cryogenic temperatures is relatively negligible for low-lying Rydberg states, $\tau_0(300\text{ K}) = 3.27\ \mu\text{s}$ vs. $\tau_0(0\text{ K}) = 4.12\ \mu\text{s}$ for $18S$ [15] (see Fig.55, *right*).

The absence of radiative transfers also means the disparition of $n'P$ atoms in the system: a consequence much more dramatic for Rydberg dressing. Indeed, limiting (ultimately suppressing) these states cancels the resonant dipole-dipole interaction and therefore halts the dephasing mechanism. Limiting the apparition of $n'P$ states can be done by reducing b (see Fig.55, *left*).

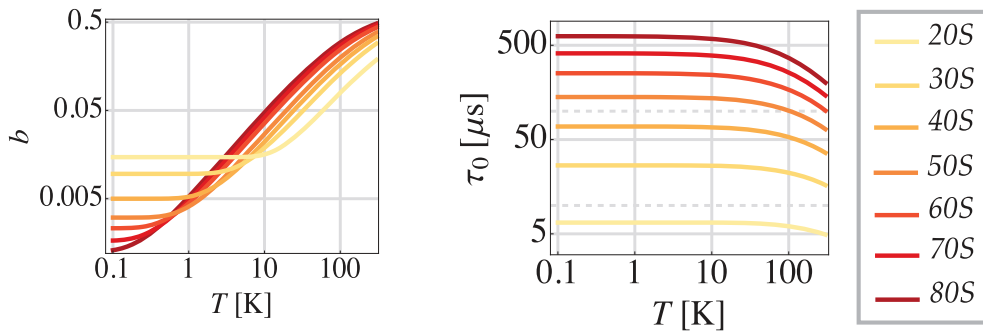


Figure 55 – **Evolution of τ_0 and b with the temperature**

For $18S$, cryogenic temperatures have a much larger impact on the branching ratio to states of opposite parity than to the lifetime.

In Rydberg-dressing proposals, the spontaneous decay rate is expected to evolve as (see Ch.3).

$$\gamma = \beta^2 \Gamma_0 = \left(\frac{\Omega}{2\delta} \right)^2 \Gamma_0 \quad (102)$$

where β is the Rydberg fraction in the mixture.

At room temperature, the actual coherence time is limited by the apparition of the first pollutant state. We have estimated this time (see Sec.4.1.3)

$$\tau_c = \left(\frac{2\delta}{\Omega} \right)^2 \frac{1}{bN\Gamma_0} \quad (103)$$

The diminution of both b and τ_0 with T suggest the existence of a temperature below which the limiting factor becomes the spontaneous decay rate. We define a critical temperature T_N^* such that the time of apparition of the first pollutant state is equal to the coherence time at $T = 300$ K.

$$\tau_c(T_N^*) = \left(\frac{2\delta}{\Omega} \right)^2 \tau_0(300 \text{ K}) \quad (104)$$

We plot the evolution of T_N^* as a function of the sample size (N) and the Rydberg level (n) (see Fig.56). The number of atoms in the system is involved in the estimation of τ_c , while the Rydberg level directly impacts the branching ratio b and the natural lifetime τ_0 .

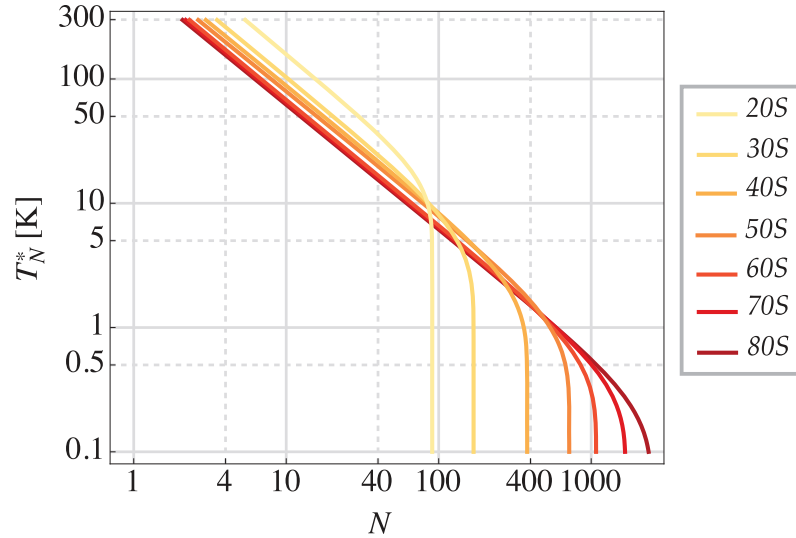


Figure 56 – Evolution of T_N^* with the temperature

Our simulations show that low atom number and low Rydberg levels are favorable to Rydberg dressing. Experiments in the range $N \sim 30 - 100$

could perform Rydberg dressing in a cryogenic environment at $T = 10$ K. Higher temperatures (*e.g.* $T = 77$ K) could be compensated by lower atom number ($N \sim 10$).

However, this approach is limited by the finite value of spontaneous decay rate: even at 0 K, spontaneous decay leads to the apparition of states of opposite parity that trigger the dephasing. This could be compensated by combining a cryogenic environment with a cut-off cavity.

4.5 PERSPECTIVES FOR RYDBERG DRESSING

In the last two chapters, we have investigated the proposal of Rydberg dressing. This technique has been proposed as a method to engineer long-range interactions between atoms in the ground state, but among with other groups (Houston[1], Munich[150]), we have observed disagreements with the proposal. We have proposed a mechanism of spontaneous dephasing due to resonant dipole-dipole interactions in the sample[60]. We have identified two types of Rydberg populations and systematically studied their dynamic evolution[24]. Despite the complex nature of this highly-correlated problem, we have captured its physics in simple mean-field equations. We have formulated possible workarounds aiming to reduce the decoherence and provide larger experimental times.

Our observations show that Rydberg dressing might be difficult to combine with Hamiltonian engineering. Probing new phases of matter typically requires 1 – 100 ms, timescales which are far beyond the range accessible today. However, Rydberg dressing can be performed at short times, as it has been proved by the Munich group[150]: by using a post-selection technique (spin-echo), the group has successfully filtered all cases exhibiting the decoherence and observed Rydberg dressing in the remaining cases. Their experiment was performed with $N = 200$ in a 2D optical lattice at room temperature.

Despite difficulties with Rydberg dressing, there is still room for Rydberg atoms in many-body quantum systems. Experiments such as the “atom-by-atom assembler” at the Institut d’Optique have demonstrated the versatility of these states in diverse experiments[9, 12, 29, 117, 124]. Low-lying Rydberg states do not exhibit decoherence at short times, which is the regime of this experiment.

In the last part of this thesis, we discuss the combination of Rydberg atoms and cryogenic environment. In particular, we focus on an improved design of the “atom-by-atom assembler” involving a cryocooler at 4 K. Such system would allow for larger experimental times and therefore larger matrices of atoms.

Part III

RYDBERG ATOMS IN A CRYOSTAT

The previous part was dedicated to the study of large ensembles of ultracold atoms trapped in optical lattices and excited to relatively low Rydberg states (see Part.ii). A different approach consists in using optical tweezers to trap the atoms. With this approach, it is possible to engineer atomic structures of several tens of atoms with arbitrary geometries. While the intersite distance in an optical lattice is typically $0.5\ \mu\text{m}$, the usual distance between two optical tweezers reaches $\geq 3\ \mu\text{m}$. This implies using much higher Rydberg states ($n > 50$) to obtain sizeable interactions. This type of quantum simulator can be used to investigate phenomena with energy scale in the MHz range, thus requiring experimental timescales much shorter than the Rydberg lifetime. Contrary to Rydberg atoms in optical lattices, Rydberg dressing is not relevant here.

The tweezer-based experiment at LCFIO has had a remarkable evolution in the last few years: Initially able to produce pair of atoms individually trapped in optical tweezers[52, 113, 148], the experiment has quickly evolved into a versatile machine generating tridimensional arbitrary atomic structures with $N = 72$ atoms[9, 10, 117]. The experiment combines a spatial light modulator (SLM) and a pair of high-NA lenses under vacuum to produce arbitrary arrays of microtraps. From stochastically filled matrices, an independent moving tweezer assembles the atoms into deterministic structures (see Sec.5.1).

However, the size of the structures is currently limited by collisions with the background gas. To increase the size of the structures, we suggest using a 4 K cryostat: at the contact of cold walls, residual gaseous particles immediately freeze and stick, effectively reducing the residual pressure. We first briefly remind the reader of the current apparatus (see Sec.5.1) before discussing the requirements of the new setup (see Sec.5.2). We detail the first steps of its construction (see Sec.5.3) with a specific focus on the optomechanical mount to be placed under vacuum at 4 K (see Sec.5.4).

5.1 ARBITRARY STRUCTURES UP TO 72 ATOMS

Started in 2010, the “atom-by-atom assembler” constituted the logical evolution of a previous experimental platform developed in the Quantum Optics group at LCFIO, the “Large Aperture Microscope” (MICROSCOPE Grande OUverture). This experiment started the investigation of pairs of Rydberg atoms individually trapped in optical tweezers, and notably the direct observation of Rydberg blockade[52, 113, 129, 148]. Adding a spatial light modulator (SLM) led to the realization of three independent tweezers[8], quickly followed by arbitrary two-dimensional arbitrary arrays of atoms[117]. Two years later, the addition of a “moving-tweezer” allowed to produce deterministic atomic structures up to 70 particles. In 2018, the acquisition of tunable lenses made possible the fabrication of artificial three-dimensional atomic structures[10].

5.1.1 PAIRS OF INTERACTING RYDBERG ATOMS

Since its beginning, the setup is based on a pair of high numerical aperture (high-NA) lenses placed under vacuum (see Fig.57). A collimated red-detuned laser beam is tightly focused at the focal plane of the first lens and serves as dipole trap (see Ch.1). We detect the the fluorescence of the D_2 line using the same aspheric lens to focus the dipole beam and collect the signal. The second aspheric lens, placed in a symmetric configuration, allows to perform diagnostics on the recollimated light.

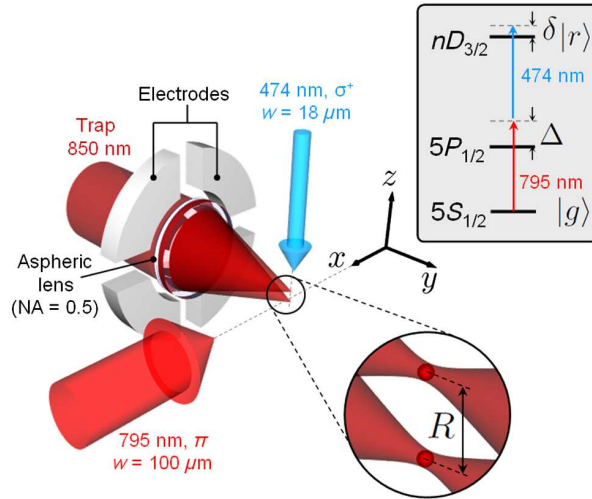


Figure 57 – **The apparatus able to trap pairs of Rydberg atoms**
The experiment as it was in 2013 (picture from [12])

The lenses are plano-convex aspheres from LightPath, with focal length $f_{\text{asp}} = 10$ mm and working distance $d_{\text{asp}} = 7$ mm. These lenses are made of D-ZLaF52LA glass and have a numerical aperture of $\text{NA} = 0.45$. They are diffraction-limited at $\lambda = 780$ nm but similar performances can be

reached at $\lambda = 850$ nm for lower apertures ($\text{NA} = 0.44$). They have been coated on their flat surface with a transparent conducting material (ITO) in order to avoid electrostatic perturbations of Rydberg levels.

The tweezer is a tightly focused red detuned dipole trap at wavelength $\lambda = 850$ nm. It is possible to replicate as many tweezers as needed by simply using several collimated dipole beams. On the earlier setup by the group (MIGOU), the distance R between a pair of tweezers was tuned by changing the incidence angle between the two collimated beam, R typically ranging from $3 - 5$ μm [52, 148]. Each tweezer has a typical $1/e^2$ radius $w_0 = 1$ μm , the typical trapping depth is $U_0/k_B \approx 1$ mK, with trapping frequencies of order of 100 kHz (radially) and 20 kHz (longitudinally). Such a microtrap can capture one atom at maximum.

Atoms are excited into the Rydberg state via the transition $|5S_{1/2}, F = 2, m_F = 2\rangle \rightarrow |nD_{3/2}, F = 3, m_F = 3\rangle$, where n typically ranges from 50 to 100. The setup uses a typical off-resonant two-photon scheme (see Ch.2) with intermediate detuning $\Delta/2\pi = 740$ MHz and two-photon Rabi frequency $\Omega/2\pi = 1$ MHz. The two lasers are locked on a ultra-stable cavity via PDH[16, 45] limiting frequency fluctuation to less than 100 kHz. These Rydberg levels lead to energy shifts $\Delta E \geq 10$ MHz at $R = 5$ μm , frequencies that require experimental timescales ($0.1 - 1$ μs) much shorter than Rydberg lifetimes (100 μs). These highly excited states being extremely sensitive to parasitical electric fields, the apparatus is equipped with an ensemble of 8 independent electrodes, placed around the lenses, and allowing to zero out the magnetic field.

We drive the Rydberg transition selectively[96]: a tightly focused beam at 850 nm can be superimposed with each trap by means of two AOM. The resulting lightshift ($\Delta E \approx h \times 10$ MHz) prevents Rydberg excitation of the addressed atoms. The addressing beam has a $1/e^2$ radius of 1.3 μm , which is slightly larger than the microtrap size.

In this initial configuration, this apparatus enabled the direct measurement of the Van der Waals interaction between two Rydberg atoms[12].

5.1.2 BUILDING ARBITRARY ARRAYS OF MICROTRAPS

A first evolution of the apparatus consisted in adding a spatial light modulator (SLM) to the setup (See Fig.58)[79]. We use this SLM to imprint a phase pattern on the dipole beam, thus replicating the original tweezer as many times as needed. The resulting array of microtraps is completely modulable and can be used to generate arbitrary trapping potentials. Some of them, such as kagome or honeycomb structures have direct counterparts in condensed matter (see Fig.59). Overall, this apparatus allows to form arbitrary structures up to 100 single-atom sites with

a minimum intersite distance of $\sim 3 \mu\text{m}$ and global dimensions $30 \times 30 \mu\text{m}$.

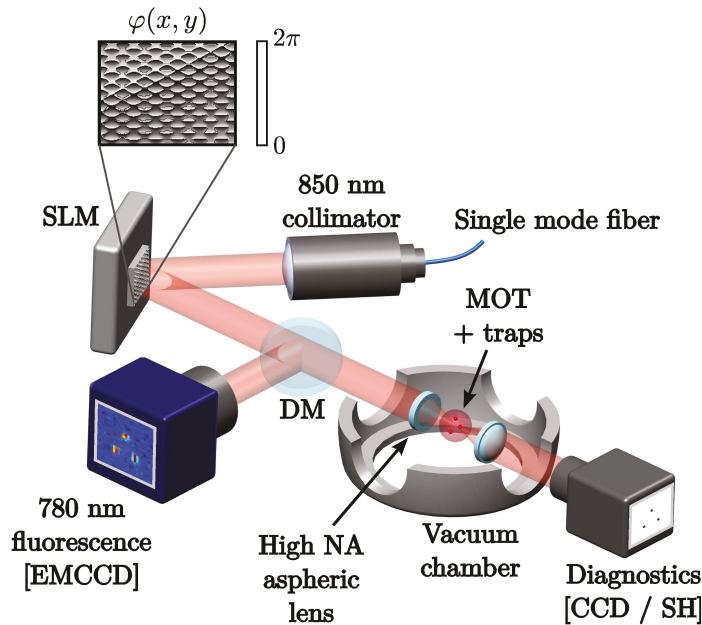


Figure 58 – **Apparatus generating arbitrary 2D atomic structures**

We use a SLM to imprint a phase pattern on the dipole beam. The beam is collimated at the center of a pair of aspheric lenses. Transmitted light is used for diagnostics. The fluorescence of trapped atoms is analyzed via an EMCCD camera (*picture from [117]*).

The spatial light modulator has an active area of $12 \times 18 \text{ mm}^2$, corresponding to 600×800 pixels. We illuminate its surface with a Gaussian beam of $1/e^2$ diameter 6.7 mm. The phase patterns are calculated with the Gerchberg-Saxton algorithm[56]. Image processing is mostly based on direct and inverse FFT. Besides, a closed-loop optimization system using a diagnostics camera ensures that the trapping depth is equivalent for all sites, notably compensating for inherent imperfection in the optical system such as astigmatism.

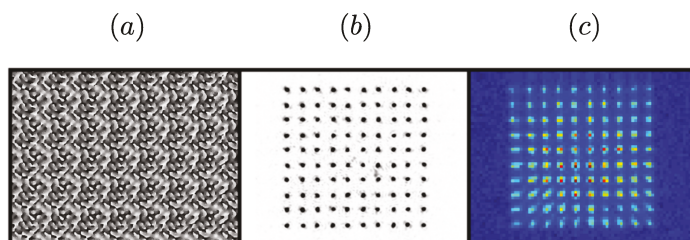


Figure 59 – **An example of array of microtraps with optical tweezers**

This SLM phase (a) leads to a cubic array of 10×10 traps of equal intensity (b). Fluorescence patterns averaged over ~ 1000 shots (c).

5.1.3 AN ATOM-BY-ATOM ASSEMBLER

Microtrap loading is a stochastic process. Assuming an array with N traps, with average occupation probability p , the probability to load n atoms in the pattern is given by the binomial distribution

$$P_n = \frac{N!}{n!(N-n)!} p^n (1-p)^{N-n} \quad (105)$$

Assuming that $p = 1/2$ (which is reasonable given[117]), the probability of a complete filling of the array reduces to

$$P_N = \frac{1}{2^N} \quad (106)$$

In the case of small structures, unit filling can spontaneously appear with a reasonable probability. However, as the number of sites increases, the loading time required to obtain a spontaneous unit filling grows exponentially. To tackle this issue, several propositions have been envisaged, notably using the Rydberg blockade[47] or tailored light-assisted collisions[68]. Yet, these methods reach 90% filling at best, still leading to exponential loading times for large arrays.

The technique implemented on the LCF experiment consists in a “moving tweezer” — an independent trapping potential able to move atoms from one site to another[114, 146]. Starting from stochastically-filled arrays of $2N$ with half-filling, this tool organizes the atoms into a defect-free arbitrary pattern of N atoms[9] (see Fig.60).

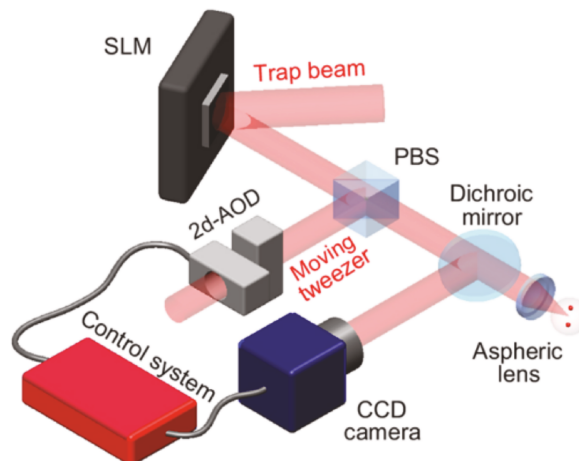


Figure 60 – **Atom-by-atom assembler**

The setup combines the array of microtraps with an independent moving tweezer (*picture from [9]*).

The moving tweezer is the same than the previously presented addressing beam. To transfer an atom from one trap to another, the moving

tweezer is superimposed to the microtrap, its optical power is then linearly ramped up during a time $\tau = 300 \mu\text{s}$ so that the trapping depth becomes $U \sim 10 U_0 = 10 \text{ mK}$, the tweezer is then moved at speed $v \sim 10 \text{ nm } \mu\text{s}^{-1}$ by sweeping the vertical and horizontal frequencies of the 2D AOM.

Deterministic atomic motion can be generalized to N atoms, and this is how organized structures are produced. We use arrays of $2N$ microtraps containing the target array of N traps as a subset. A typical sequence begins when N atoms are (randomly) trapped in the $2 \times N$ array. A fluorescence image identifies the location of each atoms. Next, an algorithm computes a serie of individual atom motions that are then transmitted to the AOM by means of microcontrollers. After all transfers are performed, a control fluorescence image verifies that the structure is defect-free. A structure of $N = 50$ atoms typically takes 50 ms to assemble, each move having a probability of success of 99.3%.

The code used to compute the trajectory is a heuristic path-finding algorithm that starts by computing all the possible individual moves and sorts them according to their length. It then moves the atoms starting from the shortest paths. When all target traps are filled, the program discards all unused atoms by pushing them away from the trapping array. This solution typically leads to $\sim N/2$ moves but does not minimize the total travel distance. While an optimal solution could be calculated, this problem is NP-complete and therefore hard to solve. In fact, the computation time required for such task might be larger than the lifetime of the atomic pattern. Heuristic algorithms find a solution which is not optimal but very close to.

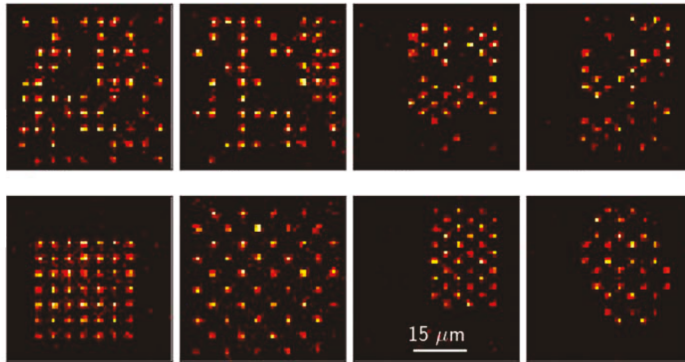


Figure 61 – **Fluorescence images of experimental random and arbitrary arrays of atoms**

From $2N$ stochastically-filled arrays (*top arrays*), we rearrange the atoms into a subset array of N atoms (*bottom arrays*) (*picture from [9]*).

5.1.4 BUILDING SYNTHETIC 3D STRUCTURES

The most recent evolution of the setup consisted in adding three electrically tunable lenses (ETL) onto the experiment [10]. While three dimensional structures can be built without these lenses (it only requires an SLM), they are essential for addressing and diagnostics. The first ETL is placed on the moving tweezer and allows to arrange the atoms in each planes. The ETL on the path of the EMCCD camera allows to selectively analyze the fluorescence, and therefore the atomic arrangement. The last ETL is placed on the control CCD (after the second asphere) allows to analyze the trapping sites in each planes.

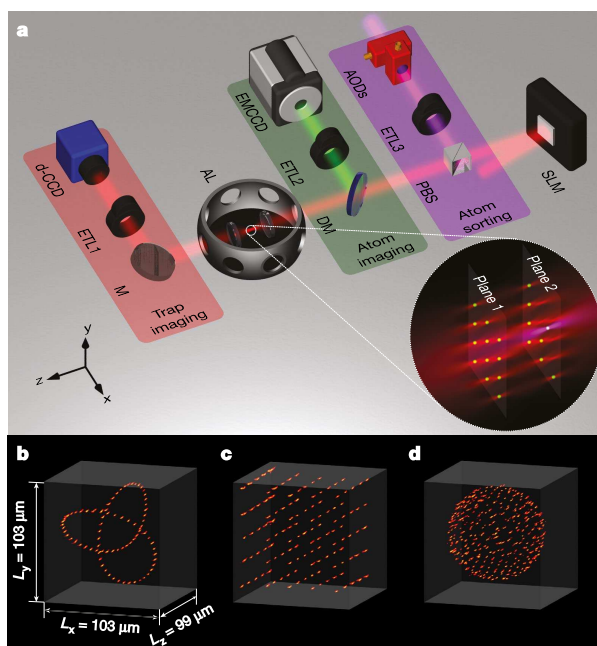


Figure 62 – **Atom-by-atom assembler of tridimensional structures**
 (a) Sketch of the apparatus (b,c,d) Examples of structures (*picture from [10]*).

This new evolution allows to assemble arbitrary tridimensional structures such as cubic lattices, Möbius strips, fullerene-like structures... or even Eiffel towers! The typical distance between two layers is about $17 \mu\text{m}$ but could be reduced to in principle $14 \mu\text{m}$.

5.2 TOWARDS STRUCTURES OF ≥ 300 ATOMS

5.2.1 MOTIVATIONS

Quantum simulation consists in building controllable many-body quantum systems that imitate the behavior of less accessible real-world systems. Quantities of interest, such as correlation functions, can be measured instead of calculated. Such “toy systems” have been engineered

with ions[36] and photons[70], the experiments at JQI and LCFIO being representative of their atomic counterpart. The experiment at JQI has successfully simulated magnetic fields[102] and two-dimensional superexchange[30], while the apparatus at LCFIO has recently investigated Ising models[101] and topological phases.

In spite of their complexity, few-body quantum systems can be calculated classically. The limit corresponding to the largest quantum system computable by exact diagonalization with classical tools is usually estimated around $N = 40$ [103]. The experiment at LCFIO has followed a bottom-up approach: in a first time, experiments performed with few-body systems could be compared to classical computations of the model. As several experiments have successfully matched theoretical predictions, we can now safely simulate larger systems that cannot be classically computed.

The new version of the experiment aims to simulate many-body systems up to $N \sim 300$, a regime which is far beyond classical computers. This regime, which has only been probed in a very limited number of geometries, promises exciting prospects.

5.2.2 LIMITATIONS OF THE CURRENT SETUP

In the current experimental setup at LCF, diagnostics and atom-by-atom assembling are time consuming. For each plane, building the atomic structure requires an initial fluorescence image, a serie of moves and a control image. Each fluorescence image takes about $\tau_{\text{fluo}} = 60$ ms and the assembling approximately scales with the number of atoms in the plane, $\tau_{\text{mt}} = 1$ ms per atom. Other steps, such as computation for the trajectories (~ 1 ms) can be neglected in first approximation (at least for low N).

Overall, a structure containing N atoms allocated in N_p planes takes at time τ_{build} to assemble, with

$$\tau_{\text{build}} = 2 N_p \tau_{\text{fluo}} + N \tau_{\text{mt}} \quad (107)$$

While this time can be relatively short for 2D structures, it increases rapidly with the number of planes. As an example, building a cubic $N = 300$ structure containing 10×10 atoms per plane would require half of a second, a $N = 324$ honeycomb structure made of 6 identical parallel planes would take more than a second.

At the same time, the lifetime of an atom in a single tweezer is not infinite. Atoms tend to escape the traps due to collisions with the residual background gas[94]. *Ab initio* estimations of this process can be delicate, notably because a precise estimation of the collision cross-section requires an excellent knowledge of the composition of the background gas.

More simply, direct measurements of the lifetime of an atom in an optical tweezer performed on our experiment provide the average $\tau_{\text{vac}} = 20$ s. This corresponds to a standard ultra-high vacuum pressure at room temperature¹.

The lifetime of a structure of N atoms trapped in individual tweezers simply corresponds to τ_{vac}/N . This sets an upper limit in the size of the arrays (see Fig.63): the time necessary to assemble the structure must be shorter than its lifetime, $\tau_{\text{vac}}/N > \tau_{\text{build}}$. Both N and N_p are limited, but structures with a lower number of planes require less time for fluorescence imaging and can therefore contain more atoms.

Assuming Eq.(107), we can estimate the maximum particles than can be assembled. This number depends on the number of planes N_p involved in the structure.

$$\begin{aligned}
 N(N_p = 1) &= 93 \\
 N(N_p = 2) &= 64 \\
 N(N_p = 3) &= 48 \\
 N(N_p = 4) &= 38 \\
 N(N_p = 5) &= 31 \\
 &\dots
 \end{aligned}
 \tag{108}$$

To date, $N = 72$ is the maximum we have achieved experimentally.

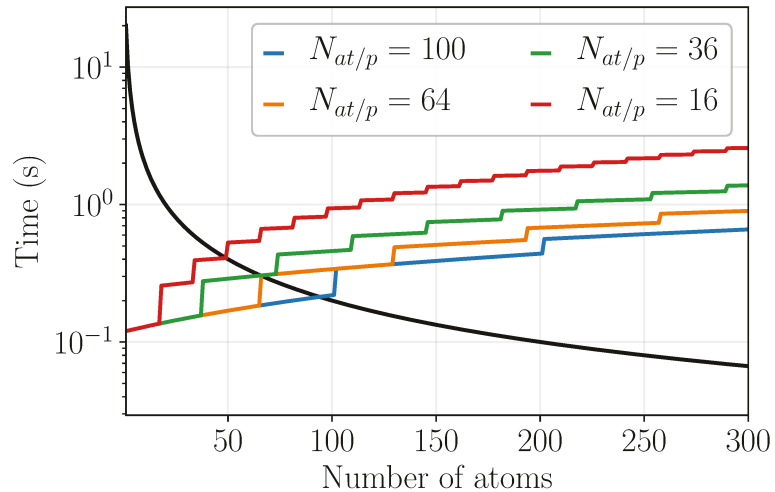


Figure 63 – **Assembling time vs. lifetime of an atomic structure**

We compare the lifetime of the structure (solid black line) to the time necessary to build tridimensional arrays. This time crucially depends on the maximum number of atoms per plan, $N_{\text{at}/p}$.

1. All the more that the system bake-out has to be done at moderate temperatures around $\sim 150^\circ\text{C}$ due to the presence of lenses under vacuum.

5.2.3 FROM UHV TO XHV

Increasing the lifetime of the atomic structure implies to reduce the vacuum background pressure. To reach the goal of $N = 300$ atoms, we infer that the lifetime must be improved by at least a factor 10 (see Fig.64).

Conventional pumping systems such as ion pumps or getter sputtering pumps[50, 75] can be added to the chamber, but there is little hope to achieve our goal by these means. Technically, our goal requires to move from ultra-high vacuum (UHV) to extremely high vacuum (XHV), corresponding to pressures below 10^{-12} mbar.

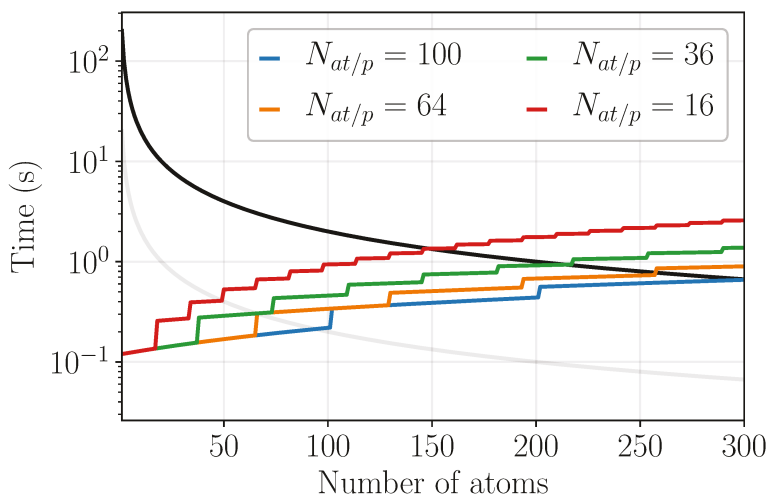


Figure 64 – **Structure lifetime vs. assembling time**

Improving the lifetime by a factor 10 ($\tau_{\text{vac}} = 200$ s on the black line) is sufficient to produce structures up to $n = 300$ atoms.

Reaching XHV can be done by using UHV technologies (*eg.* conflat gaskets) at cryogenic temperatures[95]. This technique, referred as cryopumping, consists in drastically lowering the temperature of the inner walls of the chamber so that the residual atoms in the gaseous phase stick to the walls.

5.2.3.1 CRYOPUMPING

Cryopumping involves two major phenomena[44]. First, cryocondensation corresponds to the condensation of a gas at the contact of a cold surface. At thermodynamic equilibrium, the vapor pressure can theoretically reach the saturation pressure corresponding to the temperature of the walls. This pressure can be estimated with the Clausius-Clapeyron formula, or more accurately, with the Antoine's equation[3],

$$\ln(P_0(T)) = a + \frac{b}{T + c} \quad (109)$$

with $a = 3.54$, $b = 99.40$ K and $c = 7.72$ K for H_2 , providing a pressure in bar with temperatures in K[143]. This estimate should be taken with precaution as it assumes a system at thermodynamical equilibrium, which is not the case in a UHV chamber maintained at low pressure by ion pumps.

The operating temperature of a cryopump is usually below the triple point of most species in the background pressure, so that the particles undergo a direct phase transition from gas to solid. With this simple principle, a temperature of 100 K is sufficient to eliminate water and hydrocarbons, 20 K all air components and 4 K H_2 molecules[44].

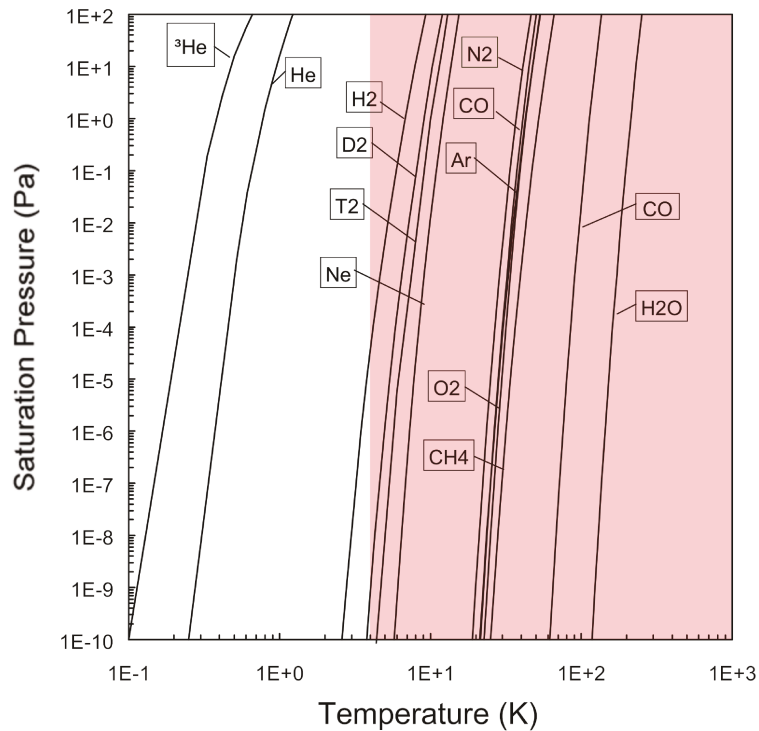


Figure 65 – **Saturation pressure evolution with the temperature**

At 4 K, only H_2 and He isotopes are not cryocondensed. The red zone corresponds to temperatures higher than 4 K (*Adapted from [44]*)

The second pumping mechanism is referred as cryosorption: gas particles near a cold surface lose the majority of their kinetic energy and are trapped near the surface by weak intermolecular forces. This physisorption results in a high concentration of particles close to the walls of the chamber and an improved vacuum at the center of the chamber.

Contrary to cryocondensation, this phenomenon is deeply influenced by the properties of the substrate. The adsorption efficiency is usually characterized by adsorption isotherms connecting the pressure with the number of molecules adsorbed per unit of surface (S). In the case of a

monolayer adsorption, the phenomenon is well captured by the Dubinin Raduschkevich Kaganer (DRK) equation, which writes[135]

$$\ln(S/S_m) = -D[k_b T \ln(P_0/P)]^2 \quad (110)$$

where S_m is the maximum monolayer capacity and D an experimental parameter notably depending on the species adsorbed.

5.2.3.2 NON EVAPORATIVE GETTER PUMPS

Cryosorbers, such as carbon glass fiber[2] or coconut charcoal[132], can be added to the chamber in order to increase the sorbing capacity and pumping speed of the system. These highly porous materials have remarkably large surface areas — up to $3000 \text{ m}^2 \text{ g}^{-1}$ for activated charcoal — and cavities that can capture gaseous particles inside them[119]. These materials are often used in high-energy experiments, notably at the LHC and ITER[2, 132]. The AMO community tend to prefer Non-Evaporative Getter pumps[108] (NEG pumps), which are another type of passive pumps. Adding a NEG pump to a cryopump can reduce the pressure by one order of magnitude[57].

5.2.3.3 SURFACE TREATMENTS

Surface treatments can also help lowering the vacuum pressure. To start, the materials used inside vacuum must have an extremely low outgassing rate. This is the case of stainless steel (notably the 300 serie of austenitic steel such as 304L or 316L), but also titanium, Cu/Be alloys, OHFC copper and aluminium. UHV pressures are usually reached by means of a thermal treatment (“bake-out” or annealing), during which the walls of the chamber are heated for hundreds of hours. The process accelerates the desorption of H_2 , thus reducing the rate of the virtual leak when back at room temperature. Each time the chamber is opened, a bake-out must be done again in order to remove H_2O .

Several treatments aiming to reduce the initial adsorption of H_2 can be done, including polishing the inner walls (ion bombardement) or using chemical treatments. Thin film deposition of Ti (also known as “Titanium sublimation”[111]), ZrO_2 or Al_2O_3 have successfully been used in high-energy experiments in the past. Some of these coatings increase the diffusion barrier of H_2 (the H_2 adsorbed in the walls cannot escape) while others transform the walls into effective getter pumps.

Overall, a cryostat at 4 K combined with NEG pumps seems to be a reasonable starting point. Given our needs, it is not yet entirely clear whether additional surface treatments will be required.

5.3 FIRST STEPS OF A CRYOGENIC ASSEMBLER

The adaptation of a cryopump requires deep modifications in the current setup. Adjusting the optomechanical parts will involve several months (or even years) of development. Besides, the radical change in dimension of the chamber necessitates to rearrange most of the optics in the setup.

At the same time, the current setup still has a lot of potential for many experiments. We would regret to stop research for the sake of new technical improvements. Rather than restrain our research capabilities, we chose to build from scratch a second apparatus dedicated to cryogenic investigations.

The first step of our development consists in assembling a single-atom experiment at room temperature. This apparatus involves the usual cooling and trapping techniques as well as a single optical tweezer focused by a high-NA lens. This setup will allow to adjust laser parameters and coils currents in a well-known regime. Eventually, the science chamber (containing the doublet of lenses) will be replaced by the cryocooler.

Meanwhile, we design optomechanical components compatible with cryogenic temperatures. Several fundamental questions, such as the behavior of the high-NA lens at low temperatures and the deformation of all mechanical components must be investigated. For this, we use a high-vacuum (HV) cryostat at 77 K to test our prototypes.

5.3.1 A NEW COLD ATOMS APPARATUS

We are currently building the new apparatus. This setup is based on the original Rydberg assembler (see Fig.66), except for the main chamber which will eventually be replaced by the 4 K cryostat. Most of the parts have been directly inspired from the original design.

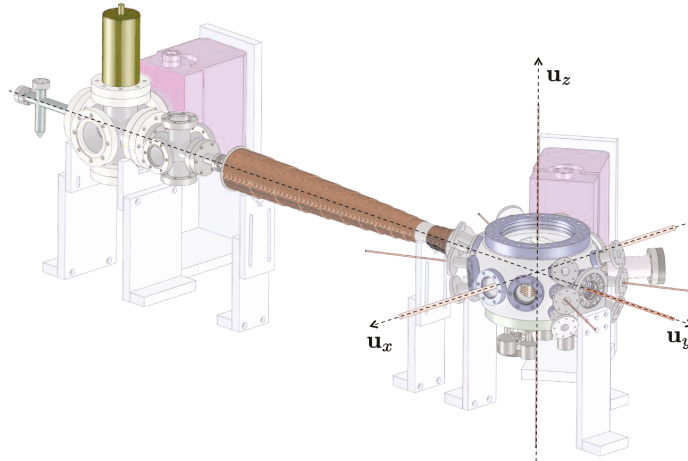


Figure 66 – **The original Rydberg assembler**

The new apparatus is largely inspired from the original Rydberg assembler.

5.3.1.1 EFFUSIVE OVEN

The oven consists in a CF-16 tube connected to the chamber by a CF-63 flange (see Fig.67). The two parts are linked by a low diameter ($\varnothing_{\text{int}} = 5 \text{ mm}$) 70 mm long pipe that acts as a spatial collimator for the Rb atoms. A 1 g ampule of Rb is placed in the CF-16 tube. We use a heating resistor to reach the boiling point of Rubidium.

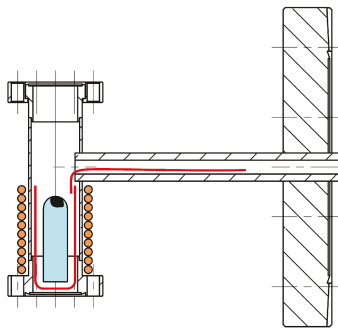


Figure 67 – **Sketch of the effusive oven**

We place a Rb ampule in the oven (in blue). A metallic mesh (in red) helps for regeneration of Rb by capillarity, the heating resistor is represented in orange.

5.3.1.2 ZEEMAN SLOWER

The Zeeman slower is a standard spin-flip design. The coils are wound on a $l = 650 \text{ mm}$ long and $\varphi = 44 \text{ mm}$ in diameter stainless steel (314L) tube, in which we slide the DN16CF flange that links the chamber and the oven (see Fig.68).

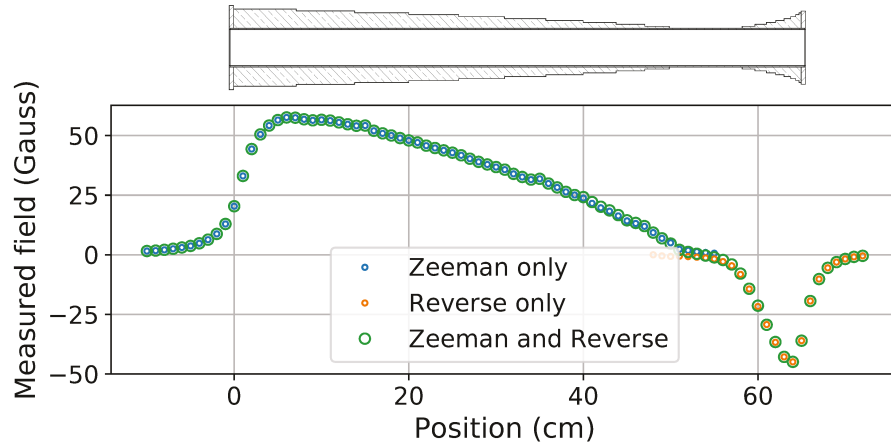


Figure 68 – **Typical magnetic field of the Zeeman slower**
Measurement of the longitudinal magnetic field at $I = 1$ A.

The main coil contains about 272 m of $\varnothing = 2$ mm copper cable, which represents a about 7.7 kg of copper. The reverse slower contains 44 m of $\varnothing = 1$ mm copper cable and weights around 320 g. We measured $R = 1.4 \Omega$ and $R_r = 0.7 \Omega$ for the electrical resistance of the main and reverse coils respectively. Driven at 1 A in both the forward and reverse coils, we obtain a maximum magnetic field of 60 G. In its standard operating regime ($I = 2$ A), the dissipated power is around $P = 8.4$ W.

5.3.1.3 MAIN CHAMBER

The main chamber comes from an earlier experiment from the group, initially set up by Charles Tuchendler[140]. This experiment was our very first apparatus using aspheric lenses to produce optical tweezers for atom trapping[134].

The chamber contains a pair of pre-aligned aspheric lenses able to produce an optical tweezer with resolution $1 \mu\text{m}$ and field-of-view $25 \mu\text{m}$. The lenses have a numerical aperture $NA = 0.5$, a focal distance of 8 mm and a working distance of 5.7 mm. Both lenses are diffraction limited between 700 nm and 880 nm and perform reasonably well up to 950 nm.

The short distance between the positions of the lenses (11.4 mm) requires small MOT beams at a shallow angle (40°). The viewports of this chamber are adapted to this original geometry (see Fig.69). The chamber is equipped with three pairs of Helmholtz coils, each of them containing 50 turns of $\varnothing = 1$ mm enamel coated copper wire, to compensate for stray magnetic field. Two additional anti-Helmholtz coils with 50 turns of the same cable generate a quadrupole magnetic field.

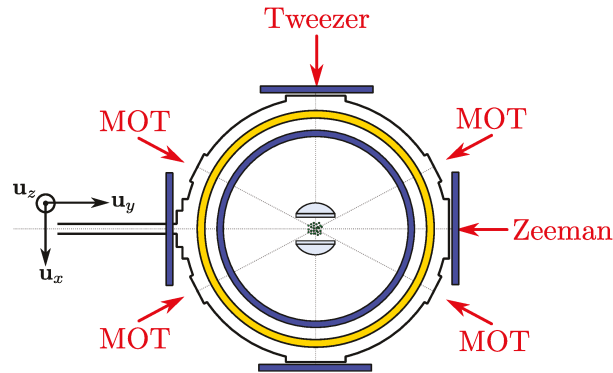


Figure 69 – **Sketch of the science chamber**

The main chamber is equipped with a doublet of aspheric lenses and the usual anti-Helmholtz coils (yellow) and three pairs of Helmholtz coils (blue).

5.3.1.4 LASER SYSTEM

The experiment is currently equipped with three lasers: a 780 nm cooling laser, a 795 nm repump laser and a 810 nm laser for the dipole trap, all Toptica DL series (see Fig.70). We protect them from feedback with optical isolators, the cooling and repump lasers are independently locked via saturated absorption spectroscopy in heated cells (“RbC” in the figure). These lasers are adjusted in frequency to match the requirements of the Zeeman slower and the MOT by means of AOM. The lights are directly combined in optical fibers and sent to the optical table.

5.3.2 CHOICE OF A CRYOCOOLER

The several types of cryocoolers are divided among two categories: recuperative and regenerative cycles[123]. Recuperative cycles, *e.g.* Joules-Thomson and Brayton cryostats, use a steady flow of gas at high-pressure which circulates in one direction. Cooling occurs in the zones of low pressure, the heat is then removed by compression of the gas. These systems are appreciated for their intrinsic low vibrational noise, but they also have a relatively low efficiency.

Regenerative cycles are mostly represented by Stirling, Gifford-McMahon (GM) and pulse-tube cycles. These schemes use oscillating flows and oscillating pressures of a cooling material, usually high-pressure liquid helium. The typical oscillating frequencies range from 1 Hz (GM cycles) to 60 Hz (Stirling cycles). They have intrinsically more vibrations than recuperative cycles, but pulse tubes are the least impacted because of the absence of moving parts.

Recent AMO experiments at 4 K use pulse tubes or GM cycles[27]. At this temperature, typical efficiencies reach 1% or less of the Carnot cycle, and the cooling power are typically in the range 0.1 – 5 W. The oscillation

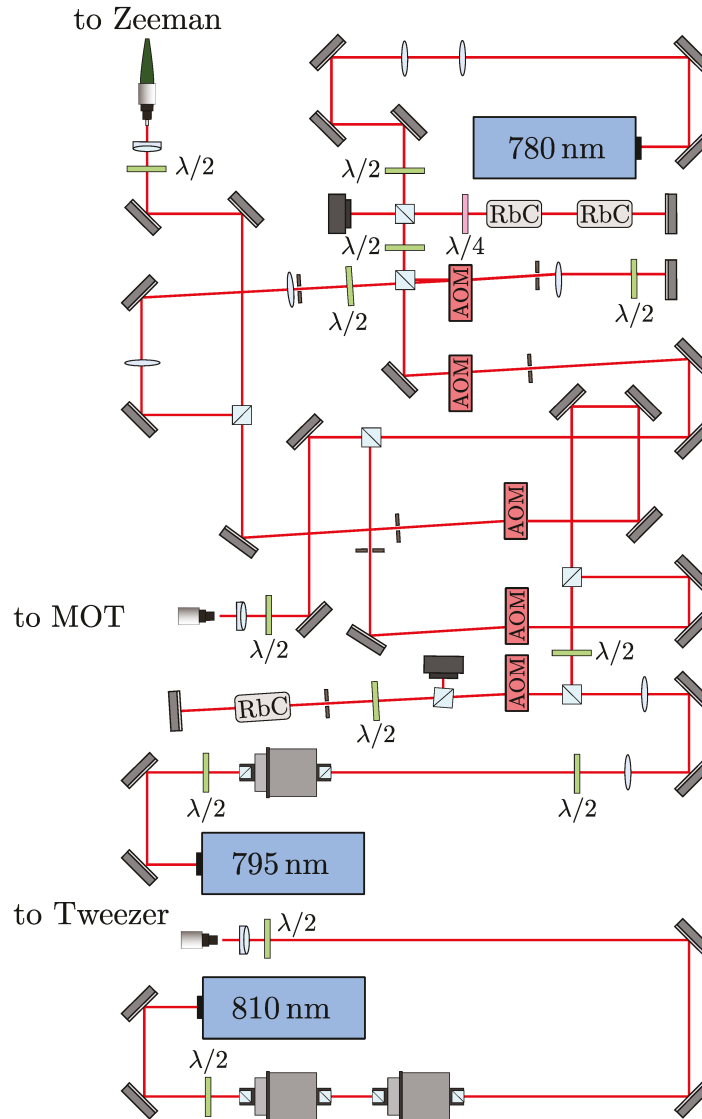


Figure 70 – **Sketch of the optical setup at the time of writing**

We use three wavelength to perform cooling, trapping and individual atom trapping. Beam separation and combination are based on polarization.

of cooling fluid typically leads to vibrations of amplitude $\sim 10 \mu\text{m}$, but solutions have been developed to tackle this issue[82]. In particular, the use of rubber bellows as only connection between the cold head compression and the science chamber allows to reduce the acoustic vibrations down to 40 nm peak-to-peak[120].

Typical systems combine two cooling stages, both using liquid helium in closed cycle. The science chamber is protected with two layers of thermal shields, typically at 50 – 70 K and 4 K. These shields are made of copper and gold plated.

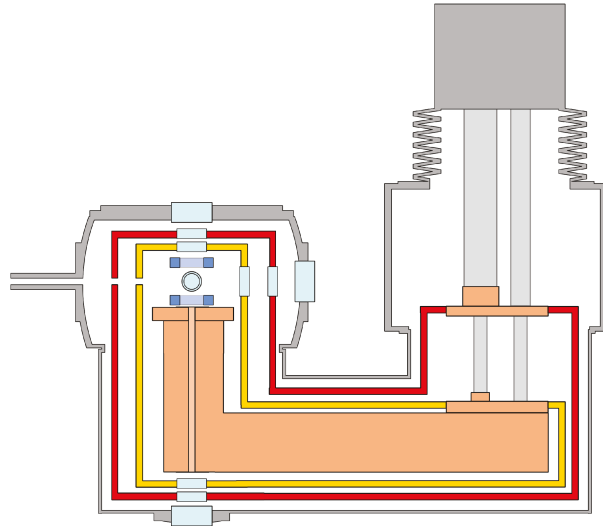


Figure 71 – **Sketch of the future cryogenic platform**

The main chamber is aside from the pulsed tube, thermal contact is ensured by a large copper cantilever (orange). Two layers of thermal shield (red and yellow) are protecting the experiment from blackbody radiation. Multiple windows provide the necessary optical access. On this view, atoms enter the chamber from the left (along \mathbf{u}_y), the Zeeman laser propagating along $-\mathbf{u}_y$.

While the technical details of our future cryostat are currently being discussed with the manufacturer, [MyCryoFirm](#), we already have a rough idea of the future design (See Fig.71). The apparatus will be separated in two chambers, one for the pulse tube, the other one for the science platform. This architecture allows for differential pumping and selective baking of the system. The main chamber will contain two layers of thermal shields with the windows necessary for optical access. Inside, we will place the pairs of aspheric lenses and set of superconductive anti-Helmholtz coils.

Many technical choices, such as the thermalization of the successive windows, the optomechanical mount for the windows, the behavior of the AR-coatings, the cables used for the coils, *etc.* still need to be discussed.

5.4 ASPHERIC LENSES IN A CRYOSTAT

5.4.1 CHALLENGES

The original design used in the current Rydberg assembler includes a pair of aspheric lenses, coils and electrodes under vacuum (See Fig.72). While the electrodes should not be deeply modified, we expect major changes in the design of the lens holders and the coils.

Using a superconducting material such as Nb-Ti allows to run higher levels of currents or smaller gauges of wire. Compared to the current setup

which uses a high diameter with a relatively small number of turns, we could instead use a much smaller gauge and several tens of turns. This would improve the compactness of the coils and the homogeneity of the field.

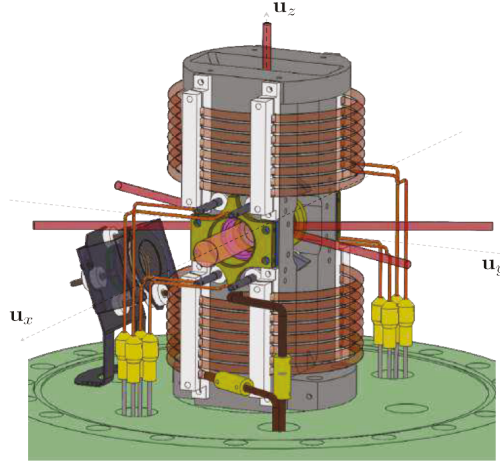


Figure 72 – **Equipment under vacuum: original design**

The original design includes a pair of aspheric lenses and coils placed under vacuum (*picture from [13]*).

Another crucial point lies in the optomechanical mount for the doublet of aspheres. The current mount consists in a stainless steel structure supporting two lens holders. The lenses are mounted inside these supports, held via a washer made of soft material (PEEK) and tightened by a stainless steel ring. The distance between the lenses is tuned by A4 stainless steel spacers inserted between the mount and the lens holders.

We expect several difficulties to arise at cryogenic temperatures. Lowering the temperature results in a global contraction of all pieces, the evolution depending on the material of each piece. The deformation of the lenses has no reason to be homothetic, so that the radius of curvature of each dioptre could change with the temperature. The thermal expansion coefficient of stainless steel is much larger than the one of glass, which should result in a high level of stress in the lenses. This could at worst break the lenses and at best induce some noticeable birefringence that would lead to polarization issues on the trapping light. More generally, little is known on the behavior of the D-ZLaF52LA glass at 4 K (the one the lenses are made of), nor is it for ITO coatings.

5.4.2 A COST-EFFECTIVE TESTING SYSTEM

The great majority of materials get their most of their thermal expansion at temperatures higher than 50 K. The evolution of their dimensions between 4 K and 50 K is usually negligible compared to the one in the range 50 – 300 K. To develop a cryogenic mount adapted to 4 K, we thus

perform our first investigations in a cryostat at 77 K.

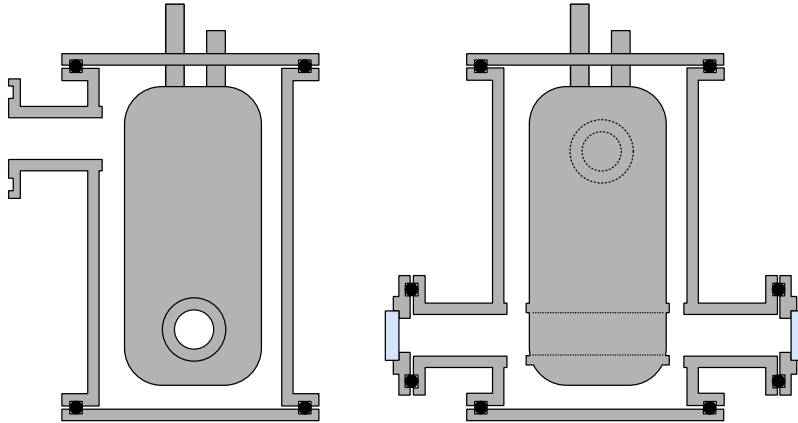


Figure 73 – **Sketch of the testbench at 77 K**

We use a cost-effective cryostat based on LN₂.

The experimental platform consists in a LN₂ reservoir of approximately 2 L capacity (see Fig.73) and placed under high vacuum ($\sim 10^{-7}$ mbar). A tube within the reservoir and aligned with optical accesses allows to test optomechanical components. The seals of the chamber are rubber-based (ISO-KF) and allow quick vacuum breaking. Overall, this modest system is cost effective and adapted to our needs for testing various lens-holder designs.

We initially design a very simple mount for the aspheric doublet. The ensemble consists in two stainless steel tubes one inside the other. The two aspheric lenses are facing each other, each of them attached to one tube. The external tube is tighten to a “cradle” which matches the shape of the reservoir. This allows to maximize thermal conduction. The internal tube is well adjusted to the external tube: to adjust the distance between the two lenses, we slide the two tubes. The position can be locked by a screw. Both lenses are held by grub screws. This rudimentary system has no control on the relative tilt or shift between the two lenses. Technical details and precise dimensions are available in App.B.

This system is meant to perform elementary checks, such as verifying that the glass is still transparent at low temperature, that the ITO coating does not crack, that the lenses do not break due to differential shrinkage, *etc.*

5.4.3 THERMAL DEFORMATION OF THE MOUNT

Initial tests performed with a thermocouple under vacuum show that the minimum temperature on the lenses is 120 K. This limit is probably due to poor thermal contact between the reservoir and the cradle, and

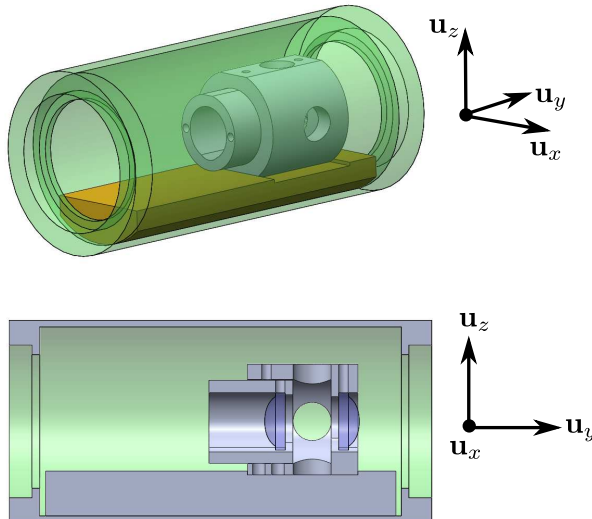


Figure 74 – **Elementary doublet mount**

(*top*) The lens mount (gray) is attached to a cradle (yellow). The ensemble is fitted onto the reservoir (green). (*bottom*) Sliding the two tubes allows to set the distance between the two lenses.

blackbody radiation coming from the viewports. Such temperature typically takes 15 h to reach. Our first observations indicate that the lenses can operate at these temperatures without major troubles.

Given the difference in linear thermal expansion coefficients between stainless steel and glass, we can assume in first approximation that most of the deformation will be happening in the stainless steel parts. We therefore neglect the variation of focal length of the lenses due to their deformation. Between 4 K and 300 K, the thermal expansion for stainless steel is typically $\Delta L/L = 3 \text{ mm m}^{-1}$.

To measure the thermal expansion of the mount, we prepare the doublet in an afocal configuration at room temperature and measure the evolution of its focal length when lowering the temperature. The diminution of the distance between the two lenses results in an equivalent lens with focal length f' that directly relates to the distance between the two lenses, e and the focal length of the two lenses $f_{\text{asph}} = 10 \text{ mm}$

$$\frac{1}{f'} = \frac{2}{f_{\text{asph}}} - \frac{e}{f_{\text{asph}}^2} \quad (111)$$

We place a beam profiler at a known distance from the optical doublet and measure the $1/e^2$ diameter of the beam as a function of the temperature. We deduce the effective focal length $f'(T)$ and the distance between the two lenses, $e = 2f_{\text{asph}} - \Delta e(T)$. Between 300 K and 120 K, we measure a displacement of $\Delta e \approx 15 \mu\text{m}$. Given **NIST data**, we estimate the thermal expansion for stainless steel between 120 K and 300 K to $\Delta L/L = 2.3 \text{ mm m}^{-1}$. Given a spacing $L = 14 \text{ mm}$ between the two

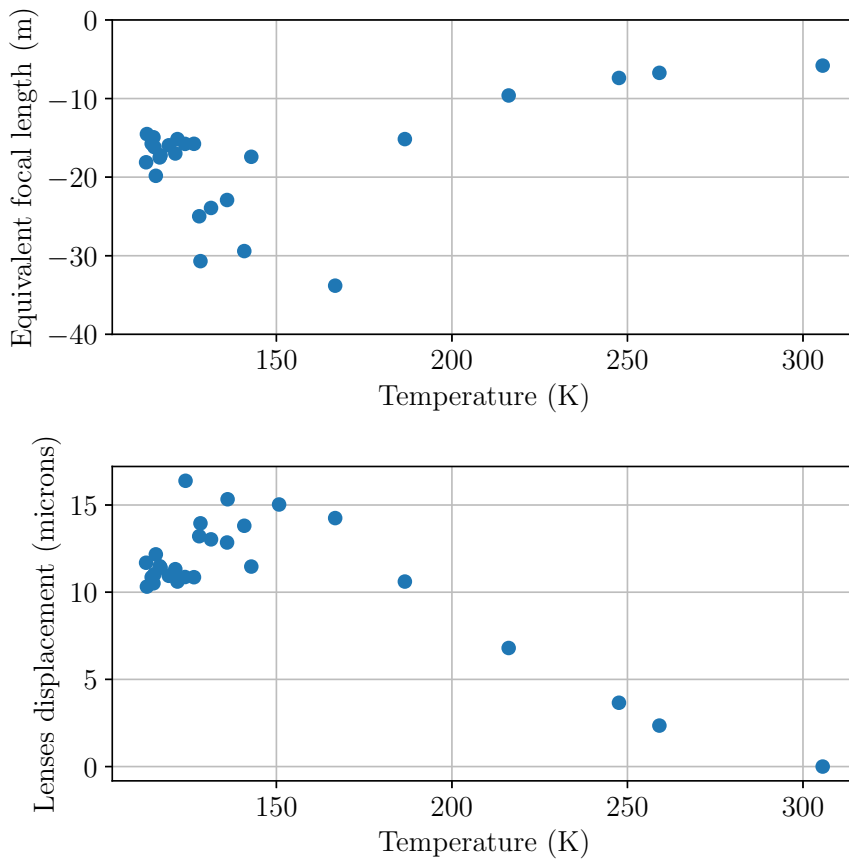


Figure 75 – **Precompensation of the thermal expansion of the mount**

We have successfully pre-compensated the diminution of the distance between the two lenses. From a converging optical system at room temperature, we obtain a nearly afocal system at cryogenic temperatures.

lenses, this provides the expected value $\Delta L = 32 \mu\text{m}$, which in the same order of magnitude than our observations.

We use this information to precompensate the setup: at room temperature we set $e = 2f_{\text{asph}} + \Delta e(120 \text{ K})$. With this setting, we obtain a nearly afocal configuration ($|f'| \approx 20 \text{ m}$) at 120 K (see Fig.75).

5.4.4 STRESS IN THE LENSES

Photoelasticimetry is an optical method based on the polarization of light and allowing to measure the stress in transparent objects[43]. This technique takes advantage of the birefringence induced by the stress in a material: imaging local alterations of the polarization allows to map the stress in the sample.

Depending on the complexity of the setup, the method can lead to qualitative or quantitative results. We use it in its simplest form, *i.e.* as a dark field plane polariscope: we place the afocal doublet between two crossed polarizers and illuminate the system with collimated white light.

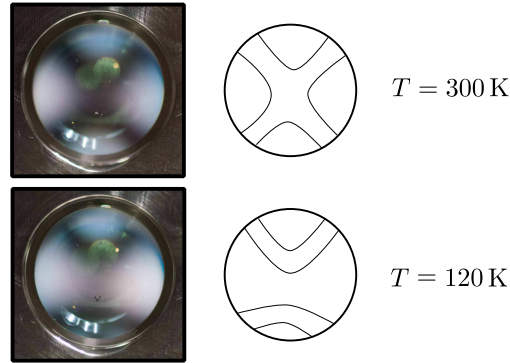


Figure 76 – **Observation of birefringence in the doublet of aspheres**

We image a beam of white light passing through the aspheric lenses between crossed polarizers. At room temperature (*upper images*), the presence of a dark cross aligned with the polarizers axes corresponds to low or no modification of the polarization. The partial disparition of the cross at lower temperatures (*lower image*) indicates the presence of birefringence.

At room temperature, we observe a black cross aligned on the principal axes of the polarizers (see Fig.76). This *isogyre* is due the setup itself[115] and appears in the absence of stress. In our case, a slight asymmetry in the cross exhibits some residual stress, probably due to the grub screw holding the lens. At 120 K, we observe a disparition of the center of the cross (the *melatope*), which is an indication of polarization rotation in the lenses, and therefore stress in the lens.

These results indicate the presence of stress, but further analysis should be done to get a quantitative information. In particular, using a circular polariscope with a monochromatic source would be an interesting complementary experiment.

5.4.5 FURTHER DEVELOPMENT OF THE CRYOGENIC EXPERIMENT

In this part, we have detailed the first developments of a new atom-by-atom assembler. The size of the structures achievable with the current setup is limited to $N \leq 72$ because of the background pressure: combining UHV components with a 4 K cryostat, we expect to reach structure sizes of order of $N \geq 300$. Working at 4 K also allows to eliminate black-body radiation and protect the system against the avalanche dephasing

observed in large Rydberg ensembles (see Part.ii).

This work is still very preliminary, but we have verified that no major obstacle prevents us from using the aspheric lenses at low temperatures. The full development of the experimental platform is still in progress and will require a significant amount of additional work in the coming months.

CONCLUSION AND PERSPECTIVES

During my doctoral studies, I had the opportunity to investigate two radically different types of Rydberg-based many-body quantum simulators. At JQI, we use $N = 40000$ Rydberg atoms trapped in optical lattices to produce many-body quantum systems in a cubic geometry. At LCF, we combine a SLM with optical tweezers to assemble smaller many-body quantum systems ($N \leq 72$) in arbitrary geometries.

One of the fundamental difference between these structures lies in the distance between two neighboring atoms, which is of order of $0.5 \mu\text{m}$ in the first case and larger than $3 \mu\text{m}$ in the second one. This imposes the use of very different Rydberg states ($n = 20$ in lattices, $n \geq 50$ in tweezers) with different lifetimes ($\tau_{20} = 5 \mu\text{s}$ and $\tau_{50} = 100 \mu\text{s}$). The tweezer-based experiment investigates phenomenon in the MHz range, therefore experimental timescales are much shorter than the Rydberg lifetime. On the contrary, the phenomena at stake in the lattice experiment are in the kHz range and necessitate a dramatic increase of the Rydberg lifetime. Rydberg dressing has been proposed as a potential solution, but its experimental implementation in large many-body quantum systems has been difficult so far.

We propose an explanation to this deviation based on observations performed on the JQI apparatus during my time there. We show that Rydberg states of opposite parity spontaneously appear in the system due to blackbody radiation at room temperature. An onset of decoherence emerges from the resonant dipole-dipole interaction between the Rydberg states of opposite parity. The physics of this phenomena is beyond mean-field and therefore extremely difficult to simulate: we circumvent this difficulty by using simple scalings that match relatively well the data. We take the opportunity to investigate the dynamics of the Rydberg populations and measure their typical timescales. A complete elimination of the decoherence seems to be unrealistic, but we show that it is possible to limit its effects notably by working at low temperatures, where blackbody radiation is minimized.

In the case of the JQI experiment, it remains possible to engineer exotic Hamiltonians without Rydberg states. Ultracold atoms in periodically driven optical lattices allow to engineer exotic phases and band structures in a process called “Floquet engineering”[5]. Combining two-dimensional motion with the double-well lattice[131] promises exciting prospects. In particular, I present in App.A a technical solution I developed to adapt the super-lattice of the JQI experiment to Floquet engineering. At the time of writing, this equipment is used to study the parametric instabili-

ties in 2-D periodically driven systems[25].

At LCF, we show that the size of the atomic structures is limited by the lifetime of the atoms in their individual microtraps. We attribute this limitation to losses induced by the residual gas in the vacuum chamber and conclude that a lower vacuum pressure is a necessary condition to assemble larger structures. Besides, larger ensembles of Rydberg atoms may be impacted by decoherence in a similar fashion than the JQI experiment. To address both issues, we suggest using a cryopump at 4 K. We take the opportunity to design a new experiment, with a particular focus on the optomechanical components to be placed under vacuum.

While remarkable results have been obtained with a linear chain containing a hundred ions[120], the cryogenic assembler will open the door to quantum simulation in arbitrary tridimensional geometries with several hundreds of interacting particles. This experiment will enable to probe many-body quantum phenomena far beyond the capabilities of classical computers, thus reaching the goal of quantum simulation.

Part IV

APPENDIX

APPENDIX A: PUBLICATION

A low-steering piezo-driven mirror

E. Magnan,^{a)} J. Maslek, C. Bracamontes, A. Restelli, T. Boulier,^{a)} and J. V. Porto
*Joint Quantum Institute, National Institute of Standards and Technology and The University of Maryland,
College Park, Maryland 20742, USA*

(Received 14 April 2018; accepted 22 June 2018; published online 18 July 2018)

We present a piezo-driven translatable mirror with excellent pointing stability, capable of driving at frequencies up to tens of kilohertz. Our system uses a tripod of piezo actuators with independently controllable drive voltages, where the ratios of the individual drive voltages are tuned to minimize residual tilting. Attached to a standard $\varnothing = 12.7$ mm mirror, the system has a resonance-free mechanical bandwidth up to 51 kHz, with displacements up to $2 \mu\text{m}$ at 8 kHz. The maximum static steering error is $5.5 \mu\text{rad}/\mu\text{m}$ displaced, and the dynamic steering error is lower than $0.6 \mu\text{rad} \mu\text{m}^{-1}$. This simple design should be useful for a large set of optical applications where tilt-free displacements are required, and we demonstrate its application in an ensemble of cold atoms trapped in periodically driven optical lattices. *Published by AIP Publishing.* <https://doi.org/10.1063/1.5035326>

I. INTRODUCTION

Piezo-based opto-mechanical devices, such as tip-tilt stages, are routinely used for applications as diverse as image stabilization,^{1,2} adaptive optics,^{3–5} microscopy,^{6,7} optical communication systems,⁸ and laser stabilization.⁹ The typical figures of merit for such devices are the modulation bandwidth of the mechanical displacement and the maximum possible displacement. For some applications, minimal angular rotation of the optical element while it is translated is essential, but typical designs¹⁰ fail to compensate for undesired tilts when driving the piezo. This is particularly true if the optical path lengths in the system are long such that angular rotation leads to large beam displacements. One approach to minimize beam steering is to stabilize rotations using kinematic restrictions that allow for translation but not rotation. The kinematic approach has the drawback that it can be complicated to implement, and the increased mass and friction of such a design can limit the bandwidth of the modulation response. We present here a mechanically simple design that provides low rotation during translation, while maintaining large mechanical bandwidths.

Ultra-cold neutral atoms can be optically trapped in the interference patterns of light to form the so-called “optical lattices,”^{11,12} which allows for cold atom simulation of crystalline many-body physics. The most common way to create such an optical lattice is to retro-reflect a laser beam from a mirror, where the position of the optical lattice is determined by the position of the retro-reflecting mirror. Electronic control of the optical lattice position, e.g., for position stabilization or to modify the quantum properties of the system by applying a time-periodic force,^{13–15} can be accomplished by moving the retro-reflected mirror. In the simplest approach using a mirror glued to a piezoelectric material, deformation of the piezo is not uniform and the mirror experiences a position dependent tilt. Typical path

lengths in optical lattice experiments are fractions of a meter, and even a small amount of steering leads to a significant misalignment of the retro-reflected beam. This misalignment results in an unwanted modulation of the optical lattice depth, which motivated the present low-steering piezo mirror design.

The system is based on a triplet of individually controlled piezo actuators, which allows for independent adjustment of the expansion of each transducer in order to correct for imbalances between the three actuators. The design substantially reduces steering errors while maintaining a multi-micron displacement up to high frequencies. The system can vibrate $\varnothing = 12.7$ mm mirrors and is compatible with standard optical mounts. The easy to assemble design has been tested on an ensemble of atoms trapped in optical lattices. This approach could be useful in a large set of applications, including high-finesse tunable optical cavities and live focus-stacking.

II. OPTOMECHANICAL DESIGN

The present design is based on a triplet of piezo actuators (Noliac NAC2012¹⁶). These piezo plates ($3 \times 3 \text{ mm}^2$) combine a low capacitance (65 nF) with a relatively high maximum free stroke (nominally $3.3 \mu\text{m}$). The piezos are epoxied onto the edges of a thin ceramic disk in an equilateral triangle (see Fig. 1). The ceramic plate (alumina, 1 mm thickness, $\varnothing = 12.7$ mm) facilitates electrical insulation between the piezos and the metal support. The plate is attached to a heavy steel support of mass $m = 310$ g which acts as a mechanical insulator, preventing resonances in the region of interest.¹⁷ While other materials (e.g., tungsten or marble) could be used, steel remains a good compromise between the density, cost, and machining time. The steel piece can be machined to fit within standard 1-in. optomechanical mirror mounts. All surface bonds are performed with a slow-curing epoxy resin.

The design is compatible with $\varnothing = 12.7$ mm mirrors. Two types of mirrors have been tested: a $(R, e, \varnothing) = (-500 \text{ mm},$

^{a)}Also at Laboratoire Charles Fabry, Institut d’Optique Graduate School, CNRS, Université Paris-Saclay, 91127 Palaiseau Cedex, France.

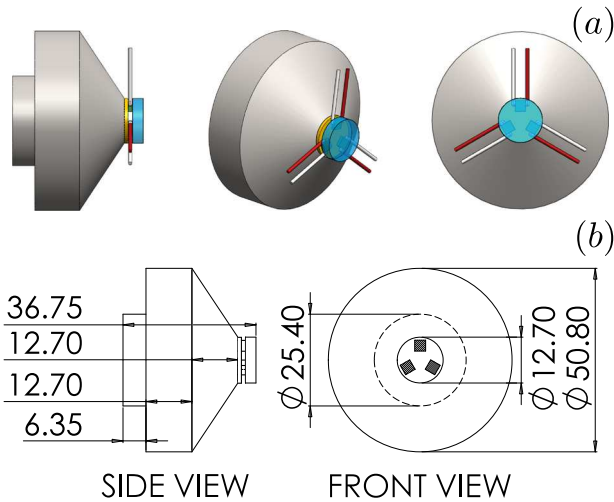


FIG. 1. **Optomechanical design:** (a) The system includes a heavy steel support (metallic gray) compatible with standard $\varnothing = 25.4$ mm optical mounts, a ceramic electrical insulator (yellow), three piezo transducers (green with white and red cables), and a mirror (in blue). (b) Technical plan of the system, all units in millimeter.

2 mm, 12.7 mm) dielectric concave mirror (Lattice Electro-Optics, Inc. RX-810-UF-MPC-0512-519) and a (e , \varnothing) = (3.1 mm, 12.7 mm) flat silver mirror (Newport ValuMax). R is the radius of curvature, e is the thickness, and \varnothing is the diameter of the mirror. In the following, we refer to these two mirrors as \mathcal{M}_1 (concave mirror) and \mathcal{M}_2 (flat mirror). Section IV presents the performance of \mathcal{M}_2 , while Sec. V demonstrates the compatibility of \mathcal{M}_1 with an ensemble of cold atoms in optical lattices.

III. ELECTRONIC SYSTEM

The three piezo actuators are controlled by a tailor-made electronic device schematically shown in Fig. 2. An external, commercial, ground-referenced high voltage driver (Piezo-Drive PX200) provides most of the amplitude necessary to drive the piezo actuators. The driver has a gain of 20 V/V over the control signal V_{Input} . The rest of the diagram shows the electronics used to vary the voltage across each piezo actuator. While PZ1 is referenced to ground, the other two piezos are referenced to nodes A and B. Through the 20 k Ω trim-pots, the adjustment voltages V_A and V_B of the two nodes can be set to $V_A = k_A \cdot V_{\text{Input}}$ and $V_B = k_B \cdot V_{\text{Input}}$, where k_A and k_B can vary from -2 to $+2$. This allows for an overall gain of those two nodes to be adjusted over 18 V/V and 22 V/V.

The design of the second amplification stage of the driver is determined by the requirements of low dynamic output impedance and high output current capabilities that are needed when a highly capacitive load is driven at high voltage and high frequency. With driving frequencies of the order of 10 kHz and peak amplitudes of the order of 100 V, the peak current flowing in each piezo can be on the order of $(100 \text{ V}) \cdot 2\pi \cdot (10 \text{ kHz}) \cdot (65 \text{ nF}) = 0.4 \text{ A}$.

To obtain this current capability, four non-inverting gain stages based on a Texas Instruments LM7171¹⁸ are connected in parallel. The choice of this simple architecture is driven by

the goals of limiting the component count, ensuring a flat frequency response over all the spectrum of operation and eliminating the additional design complexity that a push-pull or totem-pole high-current output stage with discrete transistors usually introduces. The LM7171 has a current driving capability of 100 mA. Combining four of them in parallel allows to deliver to a load up to 400 mA of peak current. In addition to the high current capability, the wide open-loop bandwidth of the operational amplifier (120 MHz) ensures a low dynamic output impedance over the entire frequency spectrum of operation of few tens of kHz.

When connecting in parallel multiple amplifiers, one issue is that small differences between their feedback networks cause them to compete with each other by forcing a slightly different voltage at the common output node. To prevent this undesirable behavior, a solution is to decouple the outputs by inserting small resistors in series. This potentially degrades the performance by increasing the overall output impedance, but in this particular circuit the value of just 1 Ω shown in Fig. 2 is sufficient to decouple the four amplifiers. The additional increase in the output impedance is only 0.25 Ω . All LM7171 are configured as non-inverting buffers with a gain of 2.

When holding a DC output voltage, or for AC drives during the typical cold atoms experimental time scales ($\tau \leq 100$ ms), the LM7171 do not require heat sinking. Full schematics, printed circuit board artwork, and bill of material for the fabrication of the circuit in Fig. 2 are available on the JQI git repository.¹⁹

IV. PERFORMANCE

In this section, we characterize the mechanical response, the maximum stroke, the static steering-error, and the amplitude of the dynamic tilt. These measurements have been performed with \mathcal{M}_2 .

A. Frequency response

We measure the frequency response of the piezo-tripod by interferometry. The setup is based on a Michelson interferometer set to measure the optical path length of a vibrating arm. The interferometer has an arm length about $l \approx 100$ mm and uses a collimated beam from a $\lambda = 780$ nm laser diode.

In order to compensate slow drifts, we phase-lock the test interferometer. The reference arm is equipped with a separate piezo-actuated mirror controlled by a feedback loop. This corrects low frequency drifts due to thermal and mechanical imperfections. The locking frequency of the proportional integral differential loop is $f_{\text{lock}} \approx 100$ Hz, which is an order of magnitude lower than the smallest frequency tested on the piezo-tripod.

A periodic path length difference Δx results in a modulation of the intensity ΔI . Around half-maximum, the \sin^2 dependence of the intensity in Δx can be linearized. In this region and assuming small path length differences ($\Delta x \ll \lambda/2$), the variation of intensity becomes proportional to the mirror displacement, $\Delta I \propto \Delta x$.

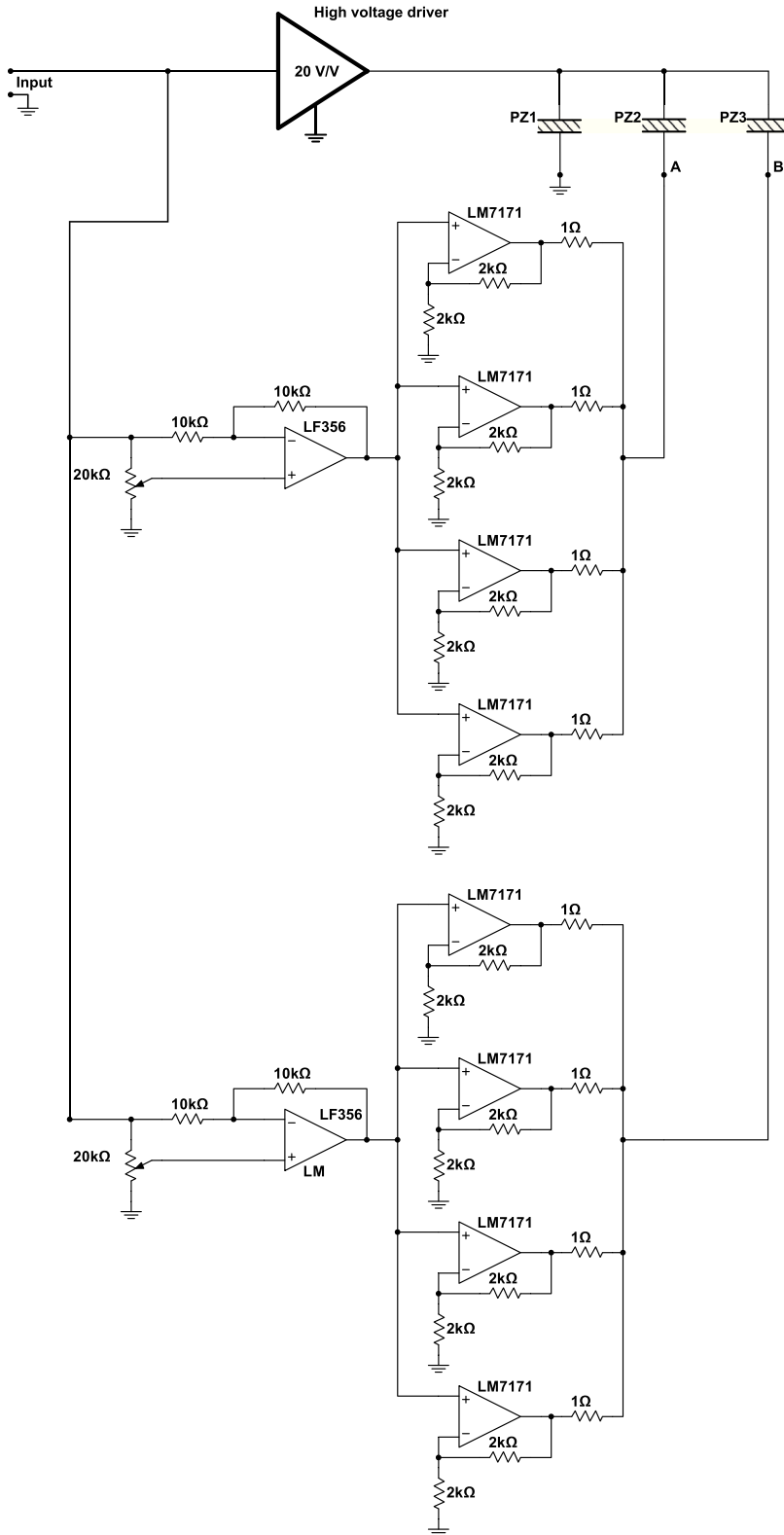


FIG. 2. **Schematic of the piezo controller:** To improve readability, the circuit diagram omits the power supply distribution and bypass network for the operational amplifiers described here briefly. All the operational amplifiers are powered from a dual-power supply between ± 15 V. Each operational amplifier has an individual bypass capacitor ($4.7 \mu\text{F}$, 0805 multilayer ceramic) very close to the positive and negative supply pins. In addition, a common $220 \mu\text{F}$ capacitor is placed between each voltage rail and ground. An effective bypassing of the power supply is critical to prevent instability especially when connecting several operational amplifiers in parallel.

We use a Bode 100 network analyzer to generate a frequency sweep from 1 kHz to 55 kHz which is then amplified and sent to the piezo-tripod. The modulation of intensity is measured by a photodiode and separated between the proportional integral differential feedback loop and the network analyzer input. We observe a flat response up to 40 kHz [see Fig. 3(a)]. The phase is decreasing linearly with a remarkable

absence of resonances up to 40 kHz. We attribute the linear decrease to a large mechanical resonance at higher frequencies.

B. Maximum displacement

The maximum displacement characterization involves the same interferometer, with the phase-locking piezo of the

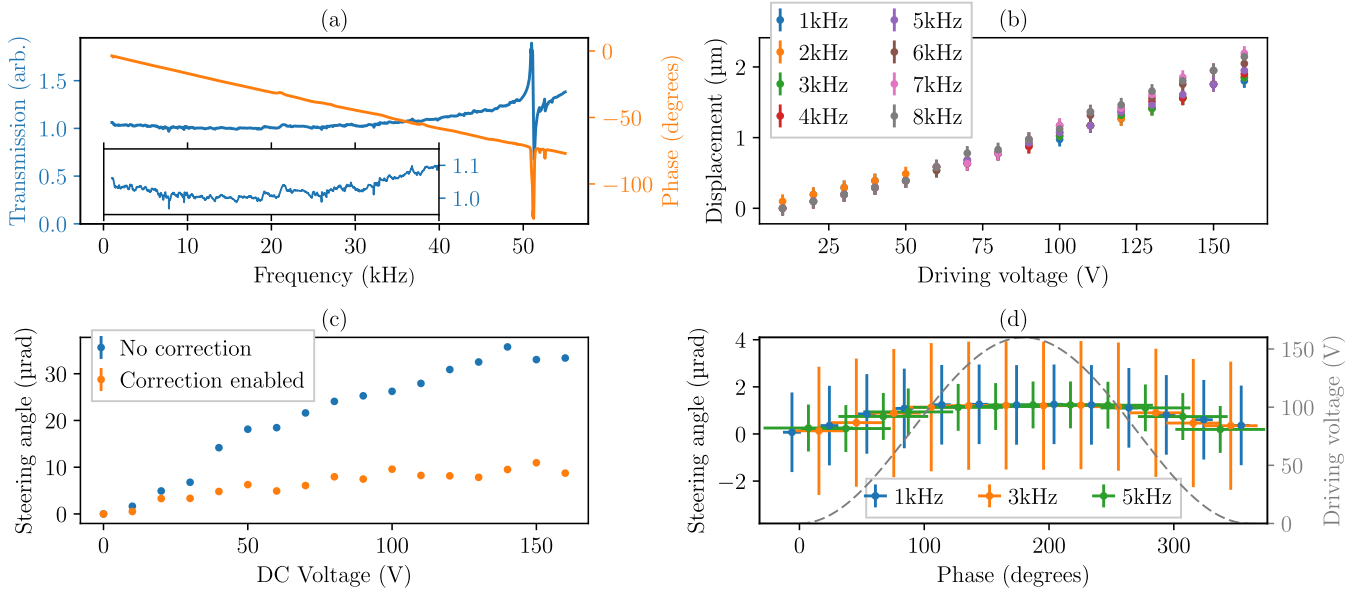


FIG. 3. **Characterization of the system:** (a) The frequency response (gain in blue, phase in orange) is flat up to 40 kHz. In the inset, we plot a zoom of the transmission in the region of interest (1 kHz–40 kHz, $\times 10$ magnification on the y-axis). (b) We achieve a $2 \mu\text{m}$ displacement up to 8 kHz. (c) The feed-forward systems enable gaining a factor of 3.5 on the static steering error. (d) We observe a maximum dynamic steering error lower than $0.6 \mu\text{rad} \mu\text{m}^{-1}$. The uncertainty of the phase is due to the exposure time of the beam profiler. The dashed gray line indicates the instantaneous voltage. On both (c) and (d), the vertical error bars correspond to the standard deviation of the fit to a Gaussian.

reference arm disabled. The piezo-tripod is driven with a periodic symmetric triangular signal, leading to a time-dependent path length difference $2\delta(t)$ with the same characteristics. Over one period, we observe n minima of intensity from which we can recover the mirror displacement δ . With the given drive circuit operating at the maximum amplitude, we achieve displacements up to $2 \mu\text{m}$ for frequencies between 1 kHz and 8 kHz [see Fig. 3(b)].

C. Static steering error

We characterize the amplitude of the static steering error by measuring the lateral displacement of a retro-reflected beam at a large distance. We place a beam profiler Thorlabs BC106N-VIS at $D = 12.38(3)$ m from the vibrating mirror. We take a reference position $\mathbf{r}_0 = \mathbf{r}(V = 0)$. We then apply a DC voltage V , measure the position of the reflected beam $\mathbf{r}(V)$ and determine the tilt angle $\theta(V) = \arctan[(r(V) - r_0)/D]$.

For each position, we average a set of 10 images and extract the position of the center with a two-dimensional Gaussian fit. The exposure time is 1 s, which helps to filter the vibrational noise. The images are taken after thermalization of the optomechanics.

We first measure the maximum static tilt without using the adjustment trim-pots of the electronic board, $k_A = k_B = 0$. We observe a $17.9(3) \mu\text{rad} \mu\text{m}^{-1}$ tilt. With the trim-pots adjusted, this reduces to $5.5(3) \mu\text{rad} \mu\text{m}^{-1}$ [see Fig. 3(c)]. We attribute the residual tilt to low-frequency thermal drifts. The intrinsic hysteresis of each piezo may also be detrimental to pointing stability. The same experiment performed with a single, center-mounted $10 \times 10 \text{ mm}^2$ piezo plate (Noliac NAC2015) leads to a static tilt larger than $250 \mu\text{rad} \mu\text{m}^{-1}$. We note that even the uncompensated design improves the steering over a single-piezo design. With drive

compensation, the steering of the tripod design is 50 times smaller.

D. Time-dependent residual tilt

The time-dependency of the tilt with a periodic shaking is measured via a similar technique. We drive the piezo-tripod with a sinusoidal signal at frequency f . The beam profiler is now placed at $D = 7.76(3)$ m from the mirror and is triggered with a pulse signal at the same frequency f than the drive. The drive phase ϕ sets the instantaneous voltage at which the picture is taken.

In order to limit effects due to heating, we gate the two signals with a 10 Hz square signal so that we only shake ten periods every 100 ms. For each trigger phase, we extract the position of the retro-reflected beam from an average over 20 fitted images. Each image has an exposure time of $20 \mu\text{s}$, which is short enough to resolve frequency-dependent tilts up to 5 kHz. The uncertainty of the measured position is given by the fit residuals.

We measure a maximum dynamic tilt of $1.25 \mu\text{rad}$ for three different frequencies (1, 3, and 5 kHz) shaken at maximum amplitude (160 V); see Fig. 3(d). This largely reduced steering error, by a factor of 10 compared to the static case, suggests that most of the DC steering is due to low frequency thermal effects. The dynamic tilt of the compensated tripod design of $0.6 \mu\text{rad} \mu\text{m}^{-1}$ is 17 times smaller than the single piezo design.

V. APPLICATION: SHAKING COLD ATOMS IN OPTICAL LATTICES

Atoms in optical lattices are extremely sensitive to the depth of the trapping potential.¹² In the case of a bowtie-shaped

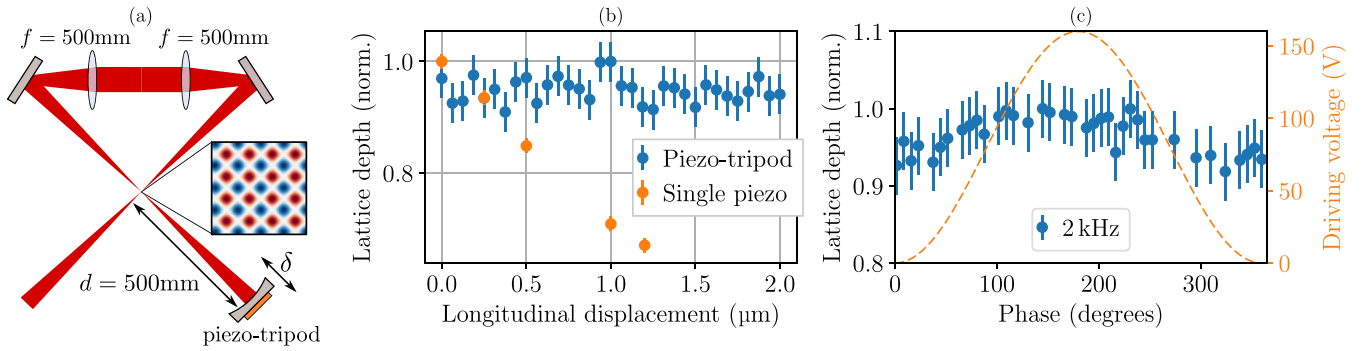


FIG. 4. **Shaking an optical lattice:** (a) The bowtie-shaped optical path leads to a two-dimensional optical lattice at the crossing of the beams. (b) We compare the performances of a single piezo actuator (Noliac NAC2015) with the piezo-tripod for DC voltages. While the first becomes rapidly unusable, the latter performs well up to its maximum displacement. The errorbars of the piezo-tripod measurement are given by F ; the ones of the single-piezo data correspond to $F/\sqrt{10}$. (c) We measure a lattice depth modulation lower than 8% for $f = 2$ kHz, with errorbars equal to F . Identical measurements done at 1, 3, and 4 kHz lead to similar results.

lattice,²⁰ misalignments in the retro-propagation as small as a few tens of microradians lead to a visible degradation of the trapping depth.

Our experimental setup consists of a ^{87}Rb Bose-Einstein condensate of $N \approx 4 \times 10^4$ atoms and typical dimension $a = 10 \mu\text{m}$ loaded into a bowtie-shaped lattice made of $\lambda = 813 \text{ nm}$ light. \mathcal{M}_1 is closing the bowtie and is placed at $d = 500 \text{ mm}$ from the atomic cloud [see Fig. 4(a)]. This leads to a $1/e^2$ beam radius of $\sigma \approx 170 \mu\text{m}$ on the atoms.

The optical lattice depth can be measured with the atoms by Kapitza-Dirac diffraction,²¹ in which the lattice light is switched on and off and the lattice depth is determined from the resulting atom diffraction.

To test the alignment for constant voltages, we step the position of the piezo and observe the evolution of the lattice depth. Over a $\delta = 2 \mu\text{m}$ displacement, the deterioration of the lattice depth is lower than the noise floor ($F = \pm 4\%$). The same experiment made with a single 100 mm^2 piezo plate (Noliac NAC2015) leads to a reduction of the lattice depth larger than 30% over less than a $1.2 \mu\text{m}$ [see Fig. 4(b)]. For this latter experiment, each datapoint corresponds to an average of 10 measurements.

To measure the instantaneous steering error, we set the mirror in a sinusoidal motion at the maximum driving amplitude. We then send the pulse of lattice light ($2 \mu\text{s}$ duration) at different phases of the drive and extract the lattice depth from the diffraction pattern. Up to 4 kHz, the measured variation in the lattice depth is lower than 8% [see Fig. 4(c)].

VI. CONCLUSION

We present the design of a retro-reflecting vibrating mirror combining high frequencies, high amplitude, and low steering error. Along with its relatively low cost, the system combines efficiency and compactness. It allows vibrating relatively large mirrors ($\varnothing = 12.7 \mu\text{m}$) with a flat frequency response, in principle, up to tens of kHz and fits into standard optomechanical mounts.

While this design was originally optimized for optical lattices, its versatility could be applicable for a wide range of applications, such as high-finesse tunable optical cavities, interferometric microscopy, and laser stabilization. We believe

that further modifications could possibly reduce the steering error, e.g., increasing the number of piezo actuators or driving each piezo with an independent waveform.

ACKNOWLEDGMENTS

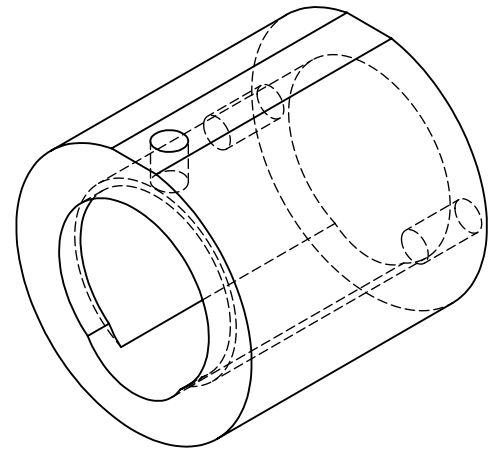
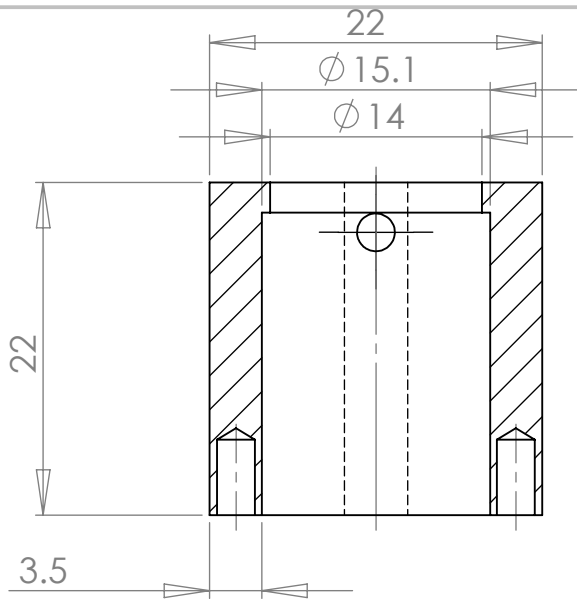
This work was partially supported by ARL-CDQI and NSF PFC at JQI. E.M. acknowledges the support of the Fulbright program and NSF PFC.

- ¹M. Eromaki, U.S. patent 0,103,555 (10 May 2007).
- ²A. P. Doel, C. N. Dunlop, J. V. Major, R. M. Myers, and A. Purvis, "Stellar image stabilization using piezo-driven active mirrors," *Proc. SPIE* **1236**, 179–192 (1990).
- ³F. Roddier, *Adaptive Optics in Astronomy* (Cambridge University Press, 1999).
- ⁴H. Wang, "Research on a bimorph piezoelectric deformable mirror for adaptive optics in optical telescope," *Opt. Express* **25**(7), 8115–8122 (2017).
- ⁵R. Davies and M. Kasper, "Adaptive optics for astronomy," *Annu. Rev. Astron. Astrophys.* **50**, 305–351 (2012).
- ⁶R. Wolleschensky, R. Grub, U. Simon, M. Gluch, A. Faulstich, and M. Voelcker, U.S. patent 6,771,417 (3 August 2004).
- ⁷S. Salapaka, A. Sebastian, J. P. Cleveland, and M. V. Salapaka, "High bandwidth nano-positioner: A robust control approach," *Rev. Sci. Instrum.* **73**(9), 3232–3241 (2002).
- ⁸J. J. Gorman, N. G. Dagalakis, and B. G. Boone, "Multi-loop control of a nanopositioning mechanism for ultra-precision beam steering," *Proc. SPIE* **5160**, 170–181 (2003).
- ⁹J. L. Hall, M. S. Taubman, and J. Ye, "Laser stabilization," in *Handbook of Optics* (McGraw-Hill Professional, 2010), Vol. II.
- ¹⁰A. Chadi, G. Méjean, R. Grilli, and D. Romanini, "Note: Simple and compact piezoelectric mirror actuator with 100 kHz bandwidth, using standard components," *Rev. Sci. Instrum.* **84**(5), 056112 (2013).
- ¹¹R. Grimm, M. Weidemüller, and Y. B. Ovchinnikov, "Optical dipole traps for neutral atoms," in *Advances in Atomic, Molecular, and Optical Physics*, edited by B. Bederson and H. Walther (Academic Press, 2000), Vol. 42.
- ¹²I. Bloch, "Ultracold quantum gases in optical lattices," *Nat. Phys.* **1**, 23–30 (2005).
- ¹³E. Arimondo, D. Ciampini, A. Eckardt, M. Holthaus, and O. Morsch, "Kilohertz-driven Bose-Einstein condensates in optical lattices," in *Advances in Atomic, Molecular, and Optical Physics* (Elsevier, 2012), Chap. 10, pp. 515–547.
- ¹⁴H. Lignier, C. Sias, D. Ciampini, Y. Singh, A. Zenesini, O. Morsch, and E. Arimondo, "Dynamical control of matter-wave tunneling in periodic potentials," in European Conference on Lasers and Electro-Optics and the International Quantum Electronics Conference, 2007.
- ¹⁵A. Zenesini, H. Lignier, D. Ciampini, O. Morsch, and E. Arimondo, "Coherent control of dressed matter waves," *Phys. Rev. Lett.* **102**, 100403 (2008).

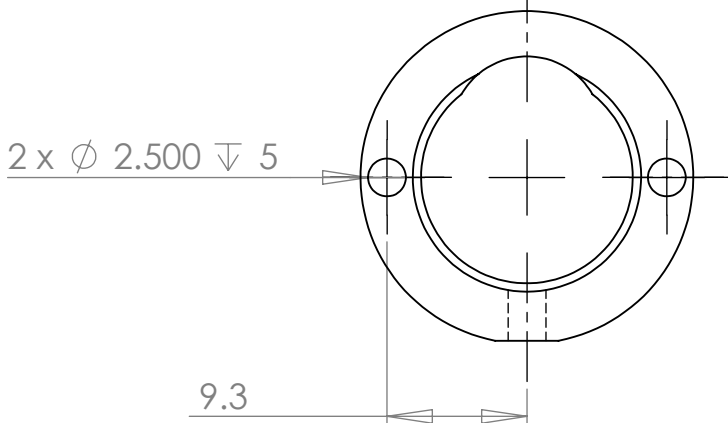
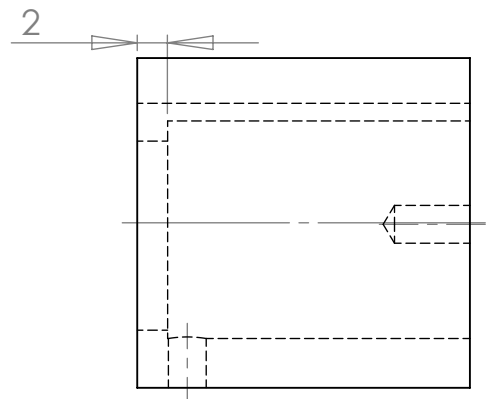
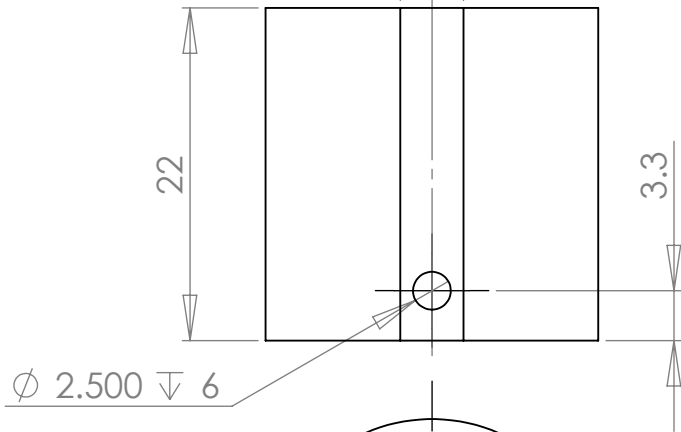
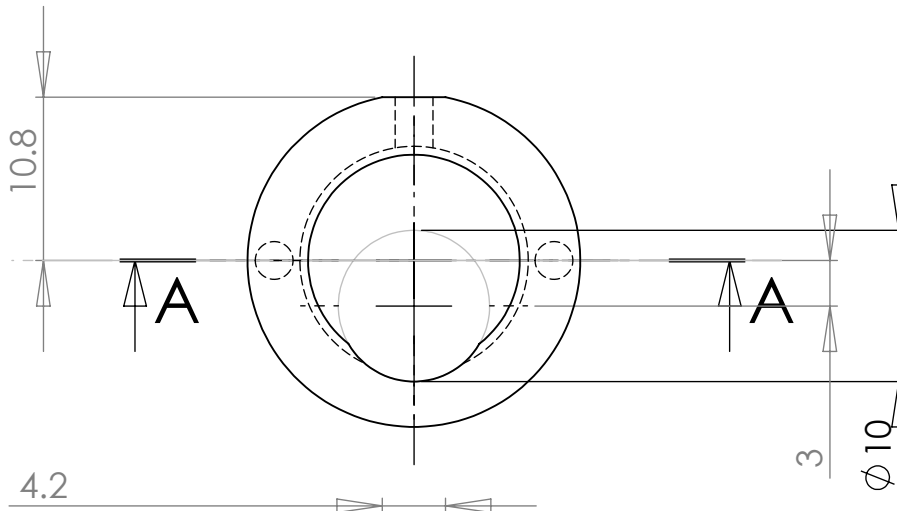
- ¹⁶Note 1. The identification of any commercial product or trade name does not imply endorsement or recommendation by the National Institute of Standards and Technology.
- ¹⁷T. C. Briles, D. C. Yost, A. Cingöz, J. Ye, and T. R. Schibli, “Simple piezoelectric-actuated mirror with 180 kHz servo bandwidth,” *Opt. Express* **18**(10), 9739–9746 (2010).
- ¹⁸LM7171 Very High Speed, High Output Current, Voltage Feedback Amplifier, Texas Instruments, 2014, Rev. C.
- ¹⁹A. Restelli, Github repository, 2018, URL: <https://github.com/JQIamo/tripod-piezo-driver>.
- ²⁰J. Sebby-Strabley, M. Anderlini, P. S. Jessen, and J. V. Porto, “Lattice of double wells for manipulating pairs of cold atoms,” *Phys. Rev. A* **73**, 033605 (2006).
- ²¹P. L. Gould, G. A. Ruff, and D. E. Pritchard, “Diffraction of atoms by light: The near-resonant Kapitza-Dirac effect,” *Phys. Rev. Lett.* **56**, 827 (1986).

B

APPENDIX B: TECHNICAL DRAWINGS FOR A FIRST OPTOMECHANICAL MOUNT

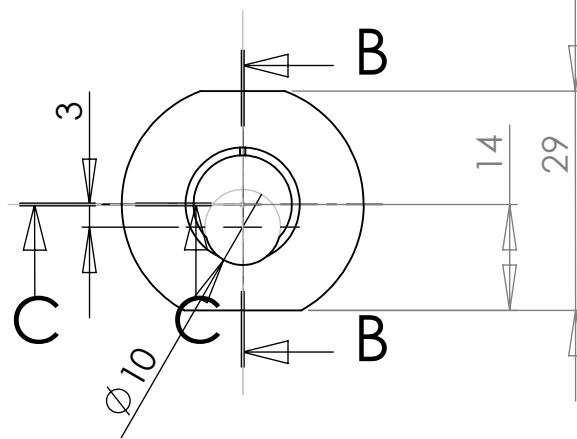
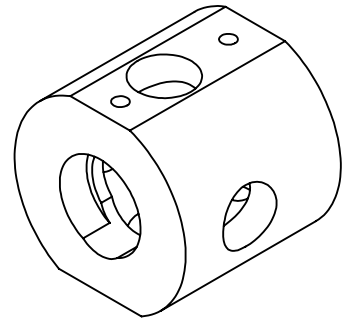
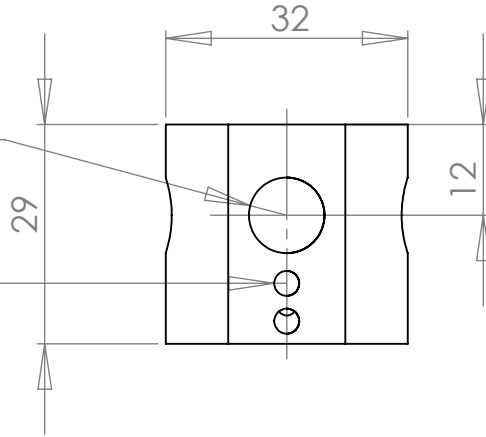
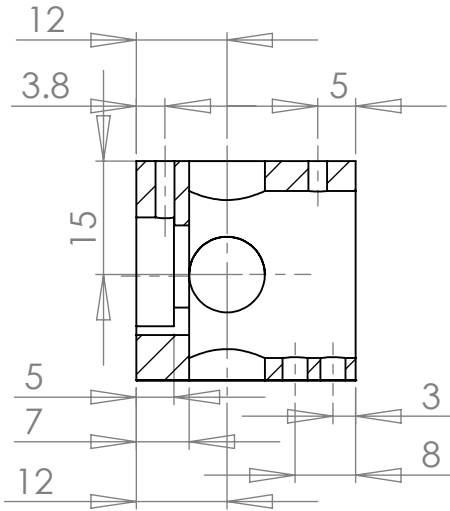


COUPE A-A



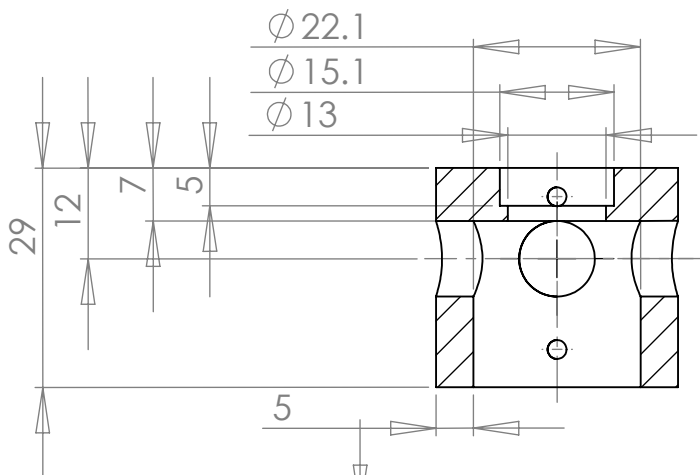
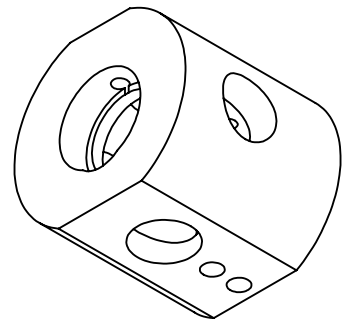
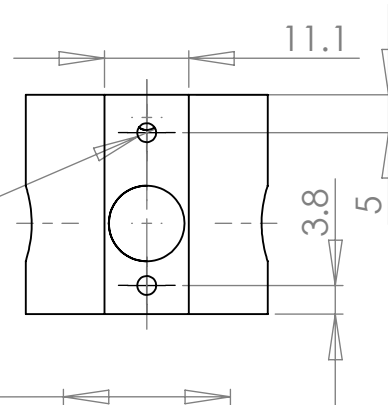
R5 A TRAVERS TOUT

2 x \varnothing 3.300 ∇ 8

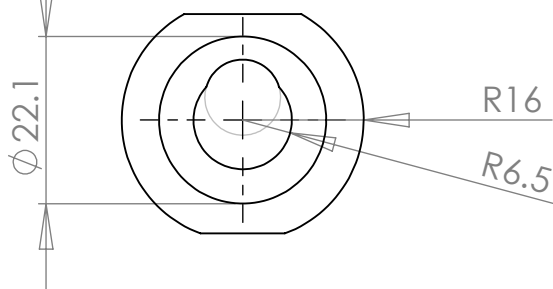


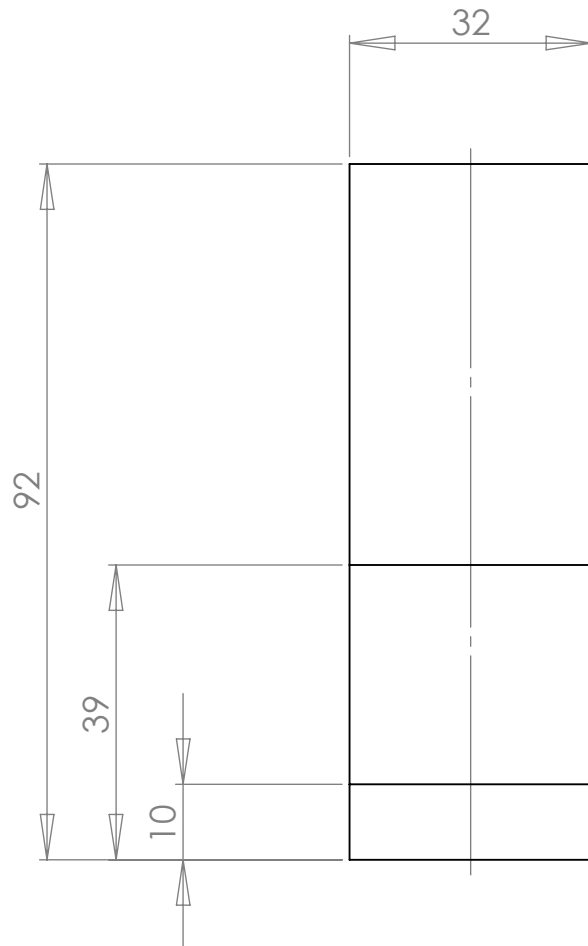
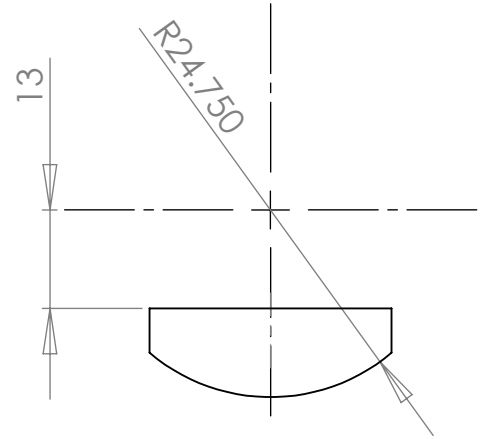
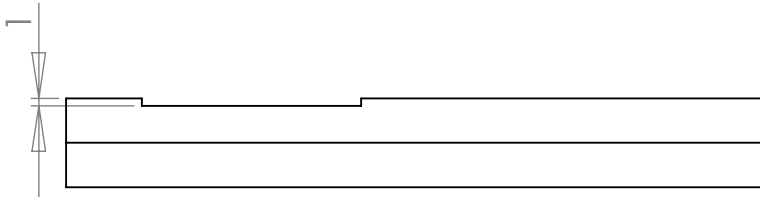
COUPE B-B

2 x \varnothing 2.500 ∇ 10



COUPE C-C





Eric Magnan
eric.magnan@institutoptique.fr

BERCEAU
MATERIAU: ALU, TOLERANCES: 0.1 mm A4

ECHELLE:1:1

FEUILLE 1 SUR 1

BIBLIOGRAPHY

- [1] J A Aman et al. « Trap losses induced by near-resonant Rydberg dressing of cold atomic gases. » In: *Phys. Rev. A* 93.043425 (2016).
- [2] V. V. Anashin et al. « Vacuum performance of a carbon fibre cryosorber for the LHC LSS beam screen. » In: *Vacuum* 75.4 (2004), pp. 293–299.
- [3] C. Antoine. « Tensions des vapeurs: nouvelle relation entre les tensions et les températures. » In: *Comptes Rendus des Seances l'Academie des Sci.* 107 (1888), pp. 681–684, 778–780, 836–837.
- [4] A Arias et al. « Realization of a Rydberg-dressed atomic clock. » In: (2018), pp. 1–6.
- [5] Ennio Arimondo et al. « Kilohertz-driven Bose-Einstein condensates in optical lattices. » In: *Adv. At. Mol. Opt. Phys.* Elsevier. Elsevier, 2012. Chap. Chapter 10, pp. 515–547. arXiv: [arXiv:1203.1259v2](https://arxiv.org/abs/1203.1259v2).
- [6] C. Ates et al. « Many-body theory of excitation dynamics in an ultracold Rydberg gas. » In: *Phys. Rev. A* 76.1 (2007), pp. 1–10.
- [7] J Balewski et al. « Rydberg dressing: understanding of collective many-body effects and implications for experiments. » In: *New J. Phys* 16.063012 (2014).
- [8] D. Barredo et al. « Demonstration of a strong rydberg blockade in three-atom systems with anisotropic interactions. » In: *Phys. Rev. Lett.* 112.18 (2014), pp. 1–5.
- [9] Daniel Barredo et al. « An atom-by-atom assembler of defect-free arbitrary two-dimensional atomic arrays. » In: *Science (80-.)*. 354.6315 (2016), pp. 1021–1023.
- [10] Daniel Barredo et al. « Synthetic three-dimensional atomic structures assembled atom by atom. » In: *Nature* 561 (2018).
- [11] D. R. Bates and A. Damgaard. « The Calculation of the Absolute Strengths of Spectral Lines. » In: *Philos. Trans. R. Soc. A Math. Phys. Eng. Sci.* 242.842 (1949), pp. 101–122.
- [12] L Béguin et al. « Direct measurement of the van der waals interaction between two rydberg atoms. » In: *Phys. Rev. Lett.* 110.26 (2013).
- [13] Lucas Béguin. « Measurement of the van der Waals interaction between two Rydberg atoms. » PhD thesis. Institut d’Optique Graduate School, 2014.
- [14] I I Beterov et al. « Ionization of Rydberg atoms by blackbody radiation. » In: *New J. Phys.* 11.11 (2009), pp. 13052–13052.

- [15] I I Beterov et al. « Quasiclassical calculations of blackbody-radiation-induced depopulation rates and effective lifetimes of Rydberg nS, nP, and nD alkali-metal atoms with $n < 80$. » In: *Phys. Rev. A* 79.052504 (2009).
- [16] Eric D Black. « An introduction to Pound–Drever–Hall laser frequency stabilization. » In: *Am. J. Phys.* 69.101 (2001), pp. 63107–680.
- [17] Immanuel Bloch. « Exploring quantum matter with ultracold atoms in optical lattices. » In: *J. Phys. B At. Mol. Opt. Phys.* 38.38 (2005), pp. 629–643.
- [18] Immanuel Bloch. « Ultracold quantum gases in optical lattices. » In: *Nat. Phys.* 1 (2005).
- [19] Immanuel Bloch, Jean Dalibard, and Sylvain Nascimbène. « Quantum simulations with ultracold quantum gases. » In: *Nat. Phys.* 8 (2012).
- [20] Immanuel Bloch, Jean Dalibard, and Wilhelm Zwerger. « Many-body physics with ultracold gases. » In: (2008).
- [21] Massimo Boninsegni and Nikolay V Prokof'ev. « Supersolids: What and Where are they ? » In: *Rev. Mod. Phys.* 84.759 (2012).
- [22] Satyendranath Bose. « Planck's law and the light quantum hypothesis. » In: *Z. Phys.* 26.178 (1924).
- [23] Isabelle Bouchoule and Klaus Mølmer. « Spin squeezing of atoms by the dipole interaction in virtually excited Rydberg states. » In: *Phys. Rev. A* 65.041803 (2002), p. 041803.
- [24] T Boulier et al. « Spontaneous avalanche dephasing in large Rydberg ensembles. » In: *Phys. Rev. A* 96.053409 (2017).
- [25] T Boulier et al. « Parametric instabilities in a 2D periodically-driven bosonic system: Beyond the weakly-interacting regime. » In: (2018), pp. 1–11.
- [26] D B Branden et al. « Radiative lifetime measurements of rubidium Rydberg states. » In: *J. Phys. B At. Mol. Opt. Phys.* 43.015002 (2010), pp. 15002–15002.
- [27] M F Brandl et al. « Cryogenic setup for trapped ion quantum computing. » In: *Rev. Sci. Inst.* 87.113103 (2016).
- [28] D. M. Brink and C. V. Sukumar. « Majorana spin-flip transitions in a magnetic trap. » In: *Phys. Rev. A* 74.3 (2006), p. 035401.
- [29] Antoine Browaeys and Thierry Lahaye. « Interacting Cold Rydberg Atoms: a Toy Many-Body System. » In: *Séminaire Poincaré XVII* (2013), pp. 125–144.
- [30] R. C. Brown et al. « Two-dimensional superexchange-mediated magnetization dynamics in an optical lattice. » In: *Science* (80-). 348.6234 (2015).

- [31] Roger C Brown et al. « Note: Pneumatically actuated and kinematically positioned optical mounts compatible with laser-cooling experiments. » In: *Cit. Rev. Sci. Instrum* 84.096101 (2013).
- [32] Roger Brown. « Nonequilibrium manybody dynamics with ultracold atoms in optical lattices and selected problems in atomic physics. » PhD thesis. University of Maryland, 2014.
- [33] H. P. Büchler et al. « Strongly correlated 2D quantum phases with cold polar molecules: Controlling the shape of the interaction potential. » In: *Phys. Rev. Lett.* 98.6 (2007), pp. 1–4.
- [34] G K Campbell et al. « Imaging the Mott Insulator Shells by Using Atomic Clock Shifts. » In: *Science (80-.)*. 313 (2006).
- [35] L. D. Carr et al. « Cold and ultracold molecules: science, technology and applications. » In: *New J. Phys.* 055049 (2009).
- [36] J. I. Cirac and P. Zoller. « Quantum Computations with cold trapped ions. » In: *Phys. Rev. Lett.* 74.20 (1995).
- [37] Connerade Jean-Patrick. *Highly Excited Atoms*. Cambridge. London, 1998.
- [38] W E Cooke and T F Gallagher. « Effects of blackbody radiation on highly excited atoms. » In: *Phys. Rev. A* 21.2 (1980).
- [39] G D 'yachkov and P M Pankratov. « On the use of the semiclassical approximation for the calculation of oscillator strengths and photoionization cross sections. » In: *J. Phys. B At. Mol. Opt. Phys.* 27 (1994), pp. 461–472.
- [40] Franco Dalfovo et al. « Theory of Bose-Einstein condensation in trapped gases. » In: ()
- [41] J. Dalibard and C. Cohen-Tannoudji. « Dressed-atom approach to atomic motion in laser light: the dipole force revisited. » In: *J. Opt. Soc. Am. B* 2.11 (1985), p. 1707.
- [42] J Dalibard and C Cohen-Tannoudji. « Laser cooling below the Doppler limit by polarization gradients: simple theoretical models. » In: *J. Opt. Soc. Am. B* 6.11 (1989).
- [43] J. W. Dally and W. F. Riley. *Experimental Stress Analysis*. McGraw-Hil.
- [44] C Day. « Basics and Applications of Cryopumps. » In: *Cern Accel. Sch. Proc. Vac. Accel.* 2006, pp. 241–274.
- [45] Sylvain De Léséleuc et al. « Analysis of imperfections in the coherent optical excitation of single atoms to Rydberg states. » In: *Phys. Rev. A* 97.5 (2018), pp. 1–9.
- [46] B. J. DeSalvo et al. « Rydberg-blockade effects in Autler-Townes spectra of ultracold strontium. » In: *Phys. Rev. A* 93.2 (2016), pp. 1–10.

- [47] Matthew Ebert et al. « Atomic fock state preparation using Rydberg blockade. » In: *Phys. Rev. Lett.* 112.4 (2014), pp. 1–5.
- [48] André Eckhard. « Atomic quantum gases in periodically driven optical lattices. » In: *Rev. Mod. Phys.* 89 (2017).
- [49] A Einstein. « Quantum Theory of a Monoatomic Ideal Gas. » In: *Sitzungsber. Kgl. Preuss. Akad. Wiss.* (1924), p. 261.
- [50] G. Firpo and A. Pozzo. « New getter pump for ultrahigh vacuum systems and transportable enclosure. » In: *Rev. Sci. Instrum.* 75.11 (2004), pp. 4828–4832.
- [51] CJ Foot. *Atomic Physics*. Oxford Uni. Oxford: Oxford University Press, 2005.
- [52] Alpha Gaëtan et al. « Observation of collective excitation of two individual atoms in the Rydberg blockade regime. » In: *Nat. Phys.* 5.2 (2009), pp. 115–118.
- [53] T F Gallagher. *Rydberg atoms*. Cambridge. Vol. 51. 143. London: Cambridge University Press, 1994, pp. 143–188.
- [54] C Gaul et al. « Resonant Rydberg Dressing of Alkaline-Earth Atoms via Electromagnetically Induced Transparency. » In: *Phys. Rev. Lett.* 116.243001 (2016).
- [55] I M Georgescu, S Ashhab, and Franco Nori. « Quantum simulation. » In: *Rev. Mod. Phys.* 86.1 (2014).
- [56] R W Gerchberg and W O Saxton. « A practical algorithm for the determination of phase from image and diffraction plane pictures. » In: *Optik (Stuttg)*. 35.2 (1972), pp. 237–246.
- [57] R Giannantonio, M Succi, and C Solcia. « Combination of a cryopump and a non-evaporable getter pump in applications. » In: *JVST A* 15 (1997), p. 187.
- [58] Stefano Giovanazzi, Axel Gorlitz, and Tilman Pfau. « Tuning the Dipolar Interaction in Quantum Gases. » In: *Phys. Rev. Lett.* 89.130401 (2002), pp. 1–4.
- [59] Sébastien Gleyzes et al. « Quantum jumps of light recording the birth and death of a photon in a cavity. » In: *Nature* 446 (2007).
- [60] E A Goldschmidt et al. « Anomalous Broadening in Driven Dissipative Rydberg Systems. » In: *Phys. Rev. Lett.* 116.113001 (2016).
- [61] K. Góral, L. Santos, and M. Lewenstein. « Quantum Phases of Dipolar Bosons in Optical Lattices. » In: *Phys. Rev. Lett.* 88.17 (2002), p. 4.
- [62] Phillip L Gould, George A Ruff, and David E Pritchard. « Diffraction of Atoms by Light: The Near-Resonant Kapitza-Dirac Effect. » In: *Phys. Rev. Lett.* 56.8 (1986).

- [63] F Gounand, M Hugon, and P R Fournier. « Radiative lifetimes of highly excited states in rubidium. » In: *J. Phys.* 41.2 (1980), pp. 119–121.
- [64] Markus Greiner et al. « Magnetic transport of trapped cold atoms over a large distance. » In: *Phys. Rev. A* 63.3 (2001), p. 031401.
- [65] Markus Greiner et al. « Quantum phase transition from a superfluid to a Mott insulator in a gas of ultracold atoms. » In: *Nature* 415.3 (2002).
- [66] David J. Griffiths. *Introduction to Quantum Mechanics*. 1995. arXiv: [0804.3728](https://arxiv.org/abs/0804.3728).
- [67] Rudolf Grimm, Matthias Weidemüller, and Yurii B Ovchinnikov. « Optical dipole traps for neutral atoms. » In: *Adv. At. Mol. Opt. Phys.* 42 (2000).
- [68] T. Grünzweig et al. « Near-deterministic preparation of a single atom in an optical microtrap. » In: *Nat. Phys.* 6.12 (2010), pp. 951–954.
- [69] A. Gurtler and W. J. Van Der Zande. « l-state selective field ionization of rubidium Rydberg states. » In: *Phys. Rev. A* 324.4 (2004), pp. 315–320.
- [70] Michael J Hartmann. « Quantum simulation with interacting photons. » In: *J. Opt.* 18.104005 (2016).
- [71] Xinghong He et al. « Model-potential calculation of lifetimes of Rydberg states of alkali atoms. » In: *J. Phys. B At. Mol. Opt. Phys.* 23 (1990).
- [72] S. Helmrich et al. « Two-body interactions and decay of three-level Rydberg-dressed atoms. » In: *J. Phys. B At. Mol. Opt. Phys.* 49.3 (2016), 03LT02.
- [73] N Henkel, R Nath, and T Pohl. « Three-Dimensional Roton Excitations and Supersolid Formation in Rydberg-Excited Bose-Einstein Condensates. » In: *Phys. Rev. Lett.* 104.195302 (2010).
- [74] N Henkel and T Pohl. « Supersolid Vortex Crystals in Rydberg-Dressed Bose-Einstein Condensates. » In: *Phys. Rev. Lett.* 108.265301 (2012).
- [75] Edwards High and Vacuum International. « Getter sputtering a review. » In: *Vacuum* 24.3 (1973), pp. 107–116.
- [76] W Hofstetter and T Qin. « Quantum simulation of strongly correlated condensed matter systems. » In: *J. Phys. B At. Mol. Opt. Phys.* 51.061001 (2018).
- [77] Jens Honer et al. « Collective Many-Body Interaction in Rydberg Dressed Atoms. » In: *Phys. Rev. Lett.* 105.160404 (2010).

- [78] Michael Höning et al. « Steady-state crystallization of Rydberg excitations in an optically driven lattice gas. » In: *Phys. Rev. A* 87.2 (2013), pp. 1–5.
- [79] J. P. Huignard. « Spatial Light Modulators and Applications. » In: *J. Opt.* 18.4 (1987).
- [80] Randall G. Hulet, Eric S. Hilfer, and Daniel Kleppner. « Inhibited spontaneous emission by a Rydberg atom. » In: *Phys. Rev. Lett.* 55.20 (1985), pp. 2137–2140.
- [81] Randall G Hulet and Daniel Kleppner. « Rydberg Atoms in "Circular" States. » In: *Phys. Rev. Lett.* 51.16 (1983).
- [82] Yuki Ikushima et al. « Ultra-low-vibration pulse-tube cryocooler system - cooling capacity and vibration. » In: *Cryogenics (Guildf)*. 48.9-10 (2008), pp. 406–412.
- [83] D Jaksch and P Zoller. « The cold atom Hubbard toolbox. » In: *Ann. Phys. (N. Y)*. 315 (2004), pp. 52–79.
- [84] D Jaksch et al. « Cold Bosonic Atoms in Optical Lattices. » In: *Phys. Rev. Lett.* 81.15 (1998).
- [85] D. Jaksch et al. « Fast Quantum Gates for Neutral Atoms. » In: *Phys. Rev. Lett.* 85.10 (2000), pp. 2208–2211.
- [86] Y.-Y Jau et al. « Entangling atomic spins with a Rydberg-dressed spin-flip blockade. » In: *Nat. Phys.* 12 (2016).
- [87] J E Johnson and S L Rolston. « Interactions between Rydberg-dressed atoms. » In: *Phys. Rev. A* 82.033412 (2010).
- [88] Tomi H Johnson, Stephen R Clark, and Dieter Jaksch. « What is a quantum simulator? » In: *EPJ Quantum Technol.* 1.1 (2014), p. 10.
- [89] P.L. Kapitza. « Viscosity of Liquid Helium below the λ -Point. » In: *Nature* 141.3558 (1938), pp. 74–74.
- [90] P.L. Kapitza and P.A.M Dirac. « The reflection of electrons from standing light waves. » In: *Math. Proc. Cambridge Philos. Soc.* 29.2 (1933).
- [91] Daniel Kleppner. « Inhibited spontaneous emission. » In: *Phys. Rev. Lett.* 47.4 (1981), pp. 233–236.
- [92] C. Kollath, Julia S. Meyer, and T. Giamarchi. « Dipolar bosons in a planar array of one-dimensional tubes. » In: *Phys. Rev. Lett.* 100.13 (2008), pp. 1–4.
- [93] S B Koller et al. « Nonlinear looped band structure of Bose-Einstein condensates in an optical lattice. » In: (2016).
- [94] S. J. M. Kuppens et al. « Loading an optical dipole trap. » In: *Phys. Rev. A* 62.1 (2000), p. 013406.
- [95] Kwang Hwa Chung Jhung et al. « Achievement of extremely high vacuum using a cryopump and conflat aluminium gaskets. » In: *Vacuum* 43.4 (1992), pp. 309–311.

- [96] Henning Labuhn et al. « Single-atom addressing in microtraps for quantum-state engineering using Rydberg atoms. » In: *Phys. Rev. A - At. Mol. Opt. Phys.* 90.2 (2014), pp. 1–4.
- [97] Tony E. Lee, Sarang Gopalakrishnan, and Mikhail D. Lukin. « Unconventional magnetism via optical pumping of interacting spin systems. » In: *Phys. Rev. Lett.* 110.25 (2013), pp. 1–5.
- [98] Tony E. Lee, H. Häffner, and M. C. Cross. « Antiferromagnetic phase transition in a nonequilibrium lattice of Rydberg atoms. » In: *Phys. Rev. A* 84.3 (2011), pp. 1–4.
- [99] Maciej Lewenstein et al. « Ultracold atomic gases in optical lattices: Mimicking condensed matter physics and beyond. » In: *Adv. Phys.* 56.02 (2007).
- [100] Wenhui H Li et al. « Millimeter-Wave Spectroscopy of Cold Rb Rydberg Atoms in a Magneto-Optical Trap: Quantum Defects of the ns, np, and nd Series. » In: *Phys. Rev. A* 67.52502 (2003).
- [101] Vincent Lienhard et al. « Observing the Space- and Time-Dependent Growth of Correlations in Dynamically Tuned Synthetic Ising Models with Antiferromagnetic Interactions. » In: *Phys. Rev. X* 8.2 (2018), pp. 1–17.
- [102] Y.-J Lin et al. « Synthetic magnetic fields for ultracold neutral atoms. » In: *Nature* 462 (2009).
- [103] Seth Lloyd. « Universal Quantum Simulators. » In: *Science (80-.)*. 273.5278 (1996), pp. 1073–1078.
- [104] Robert Low. « An experimental and theoretical guide to strongly interacting Rydberg gases. » In: *J. Phys. B* 45.113001 (2012).
- [105] Robert Löw et al. « An experimental and theoretical guide to strongly interacting Rydberg gases. » In: *J. Phys. B At. Mol. Opt. Phys. J. Phys. B At. Mol. Opt. Phys* 45.45 (2012), pp. 113001–113001.
- [106] Robert Löw et al. « Rydberg dressing: understanding of collective many-body effects and implications for experiments An experimental and theoretical guide to strongly interacting Rydberg gases Experimental investigations of dipole–dipole interactions between a few Rydberg at. » In: *New J. Phys* 16 (2014).
- [107] T Mac and T Pohl. « Rydberg dressing of atoms in optical lattices. » In: *Phys. Rev. A* 89.011402 (2014).
- [108] Enrico Maccallini et al. « Non evaporable getter (NEG) technology : A powerful tool for UHV-XHV systems. » In: *AIP Conf. Proc.* Vol. 1451. 2012, pp. 24–27.
- [109] V S Malinovsky and J L Krause. « General theory of population transfer by adiabatic rapid passage with intense, chirped laser pulses. » In: *Eur. Phys. J. D* 14.2 (2001), pp. 147–155.

- [110] F Maucher et al. « Rydberg-Induced Solitons: Three-Dimensional Self-Trapping of Matter Waves. » In: *Phys. Rev. Lett.* 106.170401 (2011).
- [111] G. M. McCracken and N. A. Pashley. « Titanium Filaments for Sublimation Pumps. » In: *J. Vac. Sci. Technol.* 3.3 (2000), pp. 96–98.
- [112] Peter W. Milonni. « Spontaneous emission between mirrors. » In: *J. Mod. Opt.* 54.13-15 (2007), pp. 2115–2120.
- [113] Y. Miroshnychenko et al. « Coherent excitation of a single atom to a Rydberg state. » In: *Phys. Rev. A - At. Mol. Opt. Phys.* 82.1 (2010), pp. 1–8.
- [114] Yevhen Miroshnychenko et al. « An atom-sorting machine. » In: *Nature* 442.7099 (2006), p. 151.
- [115] Luigi Montalto et al. « Inspection of birefringent media by photoelasticity: from diffuse light polariscope to laser conoscopic technique. » In: *Opt. Eng.* 54.8 (2015), p. 081210.
- [116] N F Mott. « The Basis of the Electron Theory of Metals, with Special Reference to the Transition Metals. » In: *Proc. Phys. Soc. Sect. A* 62.7 (1949), pp. 416–422.
- [117] F Nogrette et al. « Single-atom trapping in holographic 2D arrays of microtraps with arbitrary geometries. » In: *Phys. Rev. X* 4.021034 (2014).
- [118] T. Okoshi, K. Kikuchi, and A. Nakayama. « Novel method for high resolution measurement of laser output spectrum. » In: *Electron. Lett.* 16.16 (1980), p. 630.
- [119] Toshiro Otowa, Ritsuo Tanibata, and Masao Itoh. « Production and adsorption characteristics of MAXSORB: High-surface-area active carbon. » In: *Gas Sep. Purif.* 7.4 (1993), pp. 241–245.
- [120] G Pagano et al. « Cryogenic Trapped-Ion System for Large Scale Quantum Simulation. » In: *Quantum Sci. Technol.* (2018).
- [121] G. S. Paraoanu. « Recent Progress in Quantum Simulation Using Superconducting Circuits. » In: *J. Low Temp. Phys.* 175.5-6 (2014), pp. 633–654.
- [122] G. Pupillo et al. « Strongly Correlated Gases of Rydberg-Dressed Atoms: Quantum and Classical Dynamics. » In: *Phys. Rev. Lett.* 104.223002 (2010).
- [123] Ray Radebaugh. « Cryocoolers: the state of the art and recent developments. » In: *J. Phys. Condens. Matter* 21.164219 (2009).
- [124] Sylvain Ravets et al. « Coherent dipole–dipole coupling between two single Rydberg atoms at an electrically-tuned Förster resonance. » In: *Nat. Phys.* 10 (2014).

- [125] J. R. Rydberg. « On the structure of the line-spectra of the chemical elements. » In: *Phil. Mag. Ser.* 29.179 (1890).
- [126] M Saffman. « Quantum computing with atomic qubits and Rydberg interactions: progress and challenges. » In: *J. Phys. B At. Mol. Opt. Phys.* 49.20 (2016), p. 202001.
- [127] M Saffman, T G Walker, and K Mølmer. « Quantum information with Rydberg atoms. » In: *Rev. Mod. Phys.* 82 (2010).
- [128] H. Schempp et al. « Coherent population trapping with controlled interparticle interactions. » In: *Phys. Rev. Lett.* 104.17 (2010), pp. 1–4.
- [129] N Schlosser et al. « Subpoissonian loading of a microscopic dipole trap. » In: *Nature* 411.June (2001), p. 1024.
- [130] M J Seaton. « Quantum defect theory. » In: *Rep. Prog. Phys* 46 (1983).
- [131] J Sebby-Strabley et al. « Lattice of double wells for manipulating pairs of cold atoms. » In: *Phys. Rev. A* 73.033605 (2006).
- [132] Douglas W Sedgley, Charles R Walthers, and Everett M Jenkins. « Fusion reactor high vacuum pumping: charcoal cryosorber tritium exposure results. » In: *14th IEEE/NPSS Symp. Fusion Eng.* 1992, pp. 1233–1236.
- [133] S. Sevinçli et al. « Nonlocal nonlinear optics in cold Rydberg gases. » In: *Phys. Rev. Lett.* 107.15 (2011), pp. 1–5.
- [134] Y R P Sortais et al. « Diffraction-limited optics for single-atom manipulation. » In: *Phys. Rev. A* 75.013406 (2007).
- [135] M. J. Sparnaay. « Physisorption on heterogeneous surfaces. » In: *Surf. Sci.* 9.1 (1968), pp. 100–118.
- [136] P J St Russell et al. « Hollow-core photonic crystal fibres for gas-based nonlinear optics. » In: *Nat. Photonics* 8 (2014).
- [137] R C Stoneman, G Janik, and T F Gallagher. « Anticrossing spectroscopy of K Rydberg atoms using 300-K blackbody radiation. » In: *Phys. Rev. A* 34.4 (1986).
- [138] Leticia Tarruell et al. « Creating, moving and merging Dirac points with a Fermi gas in a tunable honeycomb lattice. » In: *Nature* 483.7389 (2012), pp. 302–305.
- [139] Constantine E Theodosiou. « Lifetimes of alkali-metal — atom Rydberg states. » In: *Phys. Rev. A* 30.6 (1984).
- [140] Charles Tuchendler. « Nouvelle generation de dispositif a microscope de grande ouverture pour le piegeage d’atomes individuels. » PhD thesis. 2015.
- [141] E Urban et al. « Observation of Rydberg blockade between two atoms. » In: *Nat. Phys.* 5 (2009).

- [142] A. Ganesh Vaidyanathan, William P. Spencer, and Daniel Kleppner. « Inhibited absorption of blackbody radiation. » In: *Phys. Rev. Lett.* 47.22 (1981), pp. 1592–1595.
- [143] A. Van Itterbeek et al. « The difference in vapour pressure between normal and equilibrium hydrogen. Vapour pressure of normal hydrogen between 20K and 32K. » In: *Physica* 30.6 (1964), pp. 1238–1244.
- [144] T Wang et al. « Superradiance in ultracold Rydberg gases. » In: *Phys. Rev. A* 75.033802 (2007).
- [145] Hendrik Weimer et al. « A Rydberg quantum simulator. » In: *Nat. Phys.* 6 (2010).
- [146] Shimon Weiss. « Fluorescence Spectroscopy of Single Biomolecules. » In: *Science (80-.)*. 283 (1999).
- [147] S Whitlock, A W Glaetzle, and P Hannaford. « Simulating quantum spin models using Rydberg- excited atomic ensembles in magnetic microtrap arrays. » In: *J . Phys. B* 50.074001 (2017).
- [148] T. Wilk et al. « Entanglement of two individual neutral atoms using rydberg blockade. » In: *Phys. Rev. Lett.* 104.1 (2010), pp. 2–5.
- [149] Jeremy T. Young et al. « Dissipation induced dipole blockade and anti-blockade in driven Rydberg systems. » In: *Phys. Rev. A* 97.023424 (2018).
- [150] Johannes Zeiher et al. « Many-body interferometry of a Rydberg-dressed spin lattice. » In: *Nat. Phys.* 12 (2016).
- [151] Alessandro Zenesini et al. « Coherent Control of Dressed Matter Waves. » In: *Phys. Rev. Lett.* 102.100403 (2008).
- [152] J Zhang et al. « Observation of a Many-Body Dynamical Phase Transition with a 53-Qubit Quantum Simulator. » In: *Nature* 551 (2017), pp. 601–604.
- [153] Myron L. Zimmerman et al. « Stark structure of the Rydberg states of alkali-metal atoms. » In: *Phys. Rev. A* 20.6 (1979), pp. 2251–2275.

Titre : Décohérence spontanée dans les grands ensembles d'atomes de Rydberg

Mots clés : Rydberg, systèmes en interaction, simulation quantique, décohérence, habillage Rydberg, atomes

Résumé : La simulation quantique consiste à réaliser expérimentalement des systèmes artificiels équivalents à des modèles proposés par les théoriciens. Pour réaliser ces systèmes, il est possible d'utiliser des atomes dont les états individuels et les interactions sont contrôlés par la lumière. En particulier, une fois excités dans un état de haute énergie (appelé état de Rydberg), les atomes peuvent être contrôlés individuellement et leurs interactions façonnées arbitrairement par des faisceaux laser. Cette thèse s'intéresse à deux types de simulateurs quantiques à base d'atomes de Rydberg, et en particulier à leurs potentielles limitations. Dans l'expérience du Joint Quantum Institute (USA), nous observons la décohérence dans une structure cubique contenant jusqu'à 40000 atomes. À partir d'atomes préparés dans un état de Rydberg bien défini, nous constatons l'apparition spontanée d'états de Rydberg voisins et le déclenchement d'un phénomène d'avalanche. Nous montrons que ce mécanisme émane de l'émission stimulée produite par le rayonnement du corps noir. Ce phénomène s'accompagne d'une diffusion induite par des interactions de type dipole-dipole résonant. Nous

complétons ces observations avec un modèle de champ moyen en état stationnaire. Dans un second temps, l'étude de la dynamique du problème nous permet de mesurer les échelles de temps caractéristiques. La décohérence étant globalement néfaste pour la simulation quantique, nous proposons plusieurs solutions pour en atténuer les effets. Nous évaluons notamment la possibilité de travailler dans un environnement cryogénique, lequel permettrait de réduire le rayonnement du corps noir. Dans l'expérience du Laboratoire Charles Fabry à l'Institut d'Optique (France), nous analysons les limites d'un simulateur quantique générant des structures bi- et tridimensionnelles allant jusqu'à 70 atomes de Rydberg piégés individuellement dans des pinces optiques. Le système actuel étant limité par le temps de vie des structures, nous montrons que l'utilisation d'un cryostat permettrait d'atteindre des tailles de structures jusqu'à 300 atomes. Nous présentons les premiers pas d'une nouvelle expérience utilisant un cryostat à 4K, et en particulier les études amont pour le développement de composants optomécaniques placés sous vide et à froid.

Title : Spontaneous decoherence in large Rydberg ensembles

Keywords : Rydberg, many-body, quantum simulation, decoherence, Rydberg dressing, atoms

Abstract : Quantum simulation consists in engineering well-controlled artificial systems that are ruled by the idealized models proposed by the theorists. Such "toy models" can be produced with individual atoms, where laser beams control individual atomic states and interatomic interactions. In particular, exciting atoms into a highly excited state (called a "Rydberg state") allows to control individual atoms and tailor interatomic interactions with light. In this thesis, we investigate experimentally two different types of Rydberg-based quantum simulators and identify some possible limitations. At the Joint Quantum Institute, we observe the decoherence of an ensemble of up to 40000 Rydberg atoms arranged in a cubic geometry. Starting from the atoms prepared in a well-defined Rydberg state, we show that the spontaneous apparition of population in nearby Rydberg states leads to an avalanche process. We identify the origin of the mechanism as stimulated emission induced by black-body radiation followed by a diffusion induced by the resonant dipole-dipole in-

teraction. We describe our observations with a steady-state mean-field analysis. We then study the dynamics of the phenomenon and measure its typical timescales. Since decoherence is overall negative for quantum simulation, we propose several solutions to mitigate the effect. Among them, we discuss the possibility to work at cryogenic temperatures, thus suppressing the black-body induced avalanche. In the experiment at Laboratoire Charles Fabry (Institut d'Optique), we analyze the limitation of a quantum simulator based on 2 and 3 dimensional arrays of up to 70 atoms trapped in optical tweezers and excited to Rydberg states. The current system is limited by the lifetime of the atomic structure. We show that working at cryogenic temperatures could allow to increase the size of the system up to $N=300$ atoms. In this context, we start a new experiment based on a 4K cryostat. We present the early stage of the new apparatus and some study concerning the optomechanical components to be placed inside the cryostat.

